INTERFACE-CONTROLLED ELECTRODEPOSITION OF SINGLE METAL & BINARY ALLOYS: SUBSTRATE-DIRECTED EPITAXY TO SOLVENT DRIVEN CO-DEPOSITION

A Thesis

Presented to the Faculty of the Graduate School

of Cornell University

In Fulfillment of the Requirements for the Degree of

Master of Science in Chemical Engineering

by

Animesh Chaturvedi

August 2025

© 2025 Animesh Chaturvedi

ABSTRACT

This thesis presents a mechanistic study of interface-controlled electrodeposition of both single-metal and binary alloy systems, with emphasis on substrate & electrolyte engineering. A scalable strain-induced compaction–annealing process was developed to fabricate Cu(111)-textured pellets with up to 96% texture ratio. These substrates are reported to be highly effective in regulating the growth of basal Zn(002) films, enabling planar deposition with high reversibility & long-term stability. Compared to commercially available Cu foils, textured Cu(111) substrates significantly reduced the nucleation overpotential, enhancing the Zn plating/stripping efficiency (~99% over 2000 cycles) and lower voltage hysteresis. These results are noteworthy because they are achieved under high current density. X-ray diffraction revealed a predictable correlation of Zn(002) texture ratio on the prepared Cu(111) substrates, with analysis of degradation of the electrodeposit texture as a function of Zn deposition amount, yielding correlation lengths of the order of 100 μm. Electrochemical analysis coupled with XPS, SEM-EDS studies confirmed well-aligned homogeneous Zn deposits on Cu(111) compared to the disordered growth on polycrystalline Cu foil.

To investigate the superior nucleation behavior of Zn on noble substrates like Cu, the role of underpotential deposition (UPD)—a phenomenon wherein Zn atoms adsorb and nucleate on the Cu surface at potentials more positive than the Zn^{2+}/Zn equilibrium potential—was examined. In this system, UPD enables the formation of a compact and stable Zn layer, energetically favored by crystallographic registry and strong interfacial bonding. Motivated by these observations, the Zn–Cu binary system was investigated to understand the role of UPD in CuZn alloy formation, given the large disparity in their standard redox potentials. At low applied potentials, UPD facilitates the formation of a Zn–Cu α-brass solid solution. In the Zn-Cu binary aqueous electrolytes, at intermediate deposition potentials (–1.0 to –1.6 V), 3D Cu–Zn clusters form via sustained UPD, acting as nucleation scaffolds that promote dense, planar Zn growth. Having established the influence of redox asymmetry and substrate interactions in the Zn–Cu system, the study transitions to the Ni–Co binary alloy system—a compositionally symmetric pair with near-identical redox potentials and atomic radii. This transition enabled the exploration of co-deposition dynamics in the

absence of UPD effects, focusing instead on phenomena such as anomalous codeposition, interfacial adsorption, and crystallographic compatibility. Together, these investigations offer a comparative framework to understand how electrochemical symmetry, nucleation energetics and substrate engineering collectively dictate alloy formation and film quality. The analysis is initially conducted in an aqueous electrolyte, where redox-inverted co-deposition is observed. However, due to pronounced hydrogen evolution reaction (HER) at higher overpotentials, it becomes difficult to establish a wider optimal deposition window. To address this, the study transitions to a polar aprotic solvent—Dimethyl sulfoxide (DMSO)—which mitigates HER exhibits passivation at high overpotentials, thereby suppressing interfacial instabilities and enabling compact Ni–Co alloy deposition. Furthermore, DMSO offers a wider and practically feasible voltage window for forming uniform Ni–Co solid solutions that closely replicate the bulk electrolyte composition.

BIOGRAPHICAL SKETCH

Animesh Chaturvedi is a graduate student at the Robert Frederick Smith School of Chemical and Biomolecular Engineering at Cornell University. Dedicated to interdisciplinary research, his current work focuses on interface-controlled electrodeposition in both aqueous and non-aqueous media, with the goal of developing next-generation anodes and coatings that exhibit enhanced reversibility, morphological stability, and long-term performance. His approach combines principles of electrochemical epitaxy, fluid–structure interactions, and metal–liquid interfacial dynamics to engineer surfaces at the microscale. Animesh earned his Bachelor of Engineering in Chemical Engineering from the Institute of Chemical Technology (ICT) Mumbai, where he also took on active leadership roles in student-led organizations and national competitions.

Driven by a broader vision to address global challenges through electrochemical science and sustainable energy technologies, Animesh is passionate about integrating deep scientific rigor with creative innovation. He is equally committed to knowledge dissemination, aesthetic expression, and purposeful impact—seeking to bridge research, design and transformative change in both academia and industry.

ACKNOWLEDGEMENTS

I gratefully acknowledge the U.S. Department of Energy for funding this research and I am deeply thankful to my special committee members – Prof. Lynden Archer and Prof. Donald Koch for their invaluable mentorship, vision and guidance throughout this work. I am especially appreciative of the freedom and intellectual space they offered me to explore bold questions and cultivate an independent research perspective.

I would like to express my sincere gratitude to the faculty and staff of the Smith School of Chemical and Biomolecular Engineering (CBE) for their continued support through access to resources and a curriculum that challenged and enriched me. This work would not have been possible without the unconditional and steadfast support of my family, whose belief in my potential has been a constant source of strength. I extend heartfelt thanks to my well-wishers, and to the Cornell Health, and Graduate Student Support Services for upholding a healthy and fair academic environment for students. I am especially thankful to my peers from several labs across CBE. Their shared pursuit of knowledge, helpful discussions, and unwavering camaraderie have added depth, warmth, and resilience to my academic journey.

TABLE OF CONTENTS

Chapters	Page No.
INTRODUCTION	6
SECTION I: Substrate-induced Epitaxial Electrodeposition	11
I.1: The Stable Crystal Facet of Copper for Planar Zinc Deposition	
I.2: Fabrication of Textured (Single-Crystal) Copper Substrate for Planar Zinc Deposition	
SECTION II: Evaluating Zn(002) Texture Evolution on Cu(111) & its Electrochemical Performance	27
II.1: Comparison of Zinc Electrodeposition on Textured Cu(111) & Polycrystalline Copper	
II.2: Evolution of Electrodeposited Zn(002) on Cu(111) with Deposition Capacity	
II.3: Investigation of Surface-controlled Zn Growth via Underpotential Deposition (UPD) on Cu	
II.4: Evaluating Zn Plating/Stripping & Cycling Performance on Cu (111) Substrate	
SECTION III: Interfacial Control in Binary Alloy Electrodeposition in Aqueous Medium	43
III.1: Crystallographic Analysis of Electrodeposited Copper in Different I-V Regimes	
III.2: Harnessing UPD of Zn on Cu for Sustained Zn-Cu Alloying & Planar Zn Growth	
III.3: Anomalous Co-deposition of Nickel & Cobalt: Evidence of Redox Inversion	
III.4: Stable Ni-Co Solid Solution Alloy Formation Window in Aqueous Medium	
SECTION IV: Mechanistic Exploration & Optimization of Ni-Co Alloy Electrodeposition in Non-Aqueous Medium	72
IV.1: Challenges in Ni-Co Electrodeposition from the Aqueous Electrolytes	
IV.2: Mechanisms in Ni–Co Alloy Electrodeposition in Non-Aqueous Medium (DMSO)	
IV.3: Optimal Electrochemical Window & Bath Composition for Ni-Co Solid Solution Formation	
CONCLUSION & OUTLOOK	93

PREFACE

This thesis marks the culmination of my Master of Science journey at Cornell University, during which I immersed myself in the exploration of electrochemical interfaces and the mechanistic design of electrodeposited materials. The central theme of this work—interface-controlled electrodeposition—arose is from my fascination with the idea that the crystallography of substrate and chemistry of the electrolyte can govern atomic-scale processes that shape macroscale behavior, particularly in energy storage systems & anti-corrosive science.

What began as a focused inquiry into zinc deposition on copper evolved into a broader investigation of epitaxy, underpotential deposition, alloy co-deposition, and the influence of solvent systems. This transformation reflects both the complexity of electrochemical systems and the freedom I was given to explore them in depth. Throughout this process, I gained not only scientific knowledge but also an appreciation for rigor, precision, and resilience in research. I hope this work contributes meaningfully to the field and inspires further efforts to engineer better, more sustainable electrochemical systems.

—Animesh Chaturvedi

INTRODUCTION

Electrodeposition is a widely used, cost-effective, and scalable technique for creating metallic coatings on electrically conductive substrates [1,2]. This method has been in use for over two centuries across diverse applications, including circuit board interconnects, electrochemical sensors, battery and fuel cell electrodes, and the fabrication of intricately shaped metal components. At its core, the process involves the migration of solvated metal ions in an electrolyte under the influence of applied electric fields and concentration gradients toward an electrically conductive surface, where they undergo electrochemical reduction to form solid metal deposits. Despite its conceptual simplicity, the electrodeposition process is governed by a rich interplay of thermodynamic and kinetic factors that render it fundamentally complex. From a thermodynamic perspective, factors such as phase stability, interfacial energies and lattice compatibility influence the feasibility of forming specific crystalline structures and textures. However, the actual deposition behavior is predominantly dictated by kinetic parameters including ion transport, charge transfer rates, nucleation dynamics, and surface diffusion. This divergence between thermodynamic favorability and kinetic accessibility often results in deposits with undesirable morphologies—such as rough, cracked, or inhomogeneous films.

A critical challenge stems from the fact that electrodeposition of metals is an electrocrystallization process: the reduction of metal ions from the electrolyte results in the nucleation and growth of crystalline materials, whose symmetry and orientation may conflict with the intended geometry of the coating [3-7]. Furthermore, metal ions in solution are not isolated species—they exist as complexes with other electrolyte components, leading to deposition that often occurs concurrently with competing electrochemical or chemical reactions. Compounding these issues are several instability mechanisms inherent to the process. Morphological instabilities, such as those described by the Mullins–Sekerka mechanism, arise when ions preferentially migrate toward surface protrusions due to locally amplified electric fields and concentration gradients [8]. This causes non-planar growth and uneven thicknesses across the deposited film. At higher overpotentials, especially beyond the diffusion-limited regime, ion depletion near the electrode surface gives rise to an extended space charge layer [9]. Within this layer, electro-osmotic forces induce electroconvection—hydrodynamic instabilities that further exacerbate non-uniform growth by locally enhancing ion transport toward rapidly advancing features [10-13]. Consequently, while

electrodeposition remains a powerful and highly tunable approach for materials synthesis, achieving uniform, defect-free coatings require a nuanced understanding of both the underlying physicochemical mechanisms and the instabilities that can emerge during growth.

This study builds on three key strategies for advancing control over electrodeposition: electrochemical epitaxy for crystallographic alignment and interfacial stability, and dynamic metal–liquid interphases—especially in organic solvents—that tune nucleation kinetics and suppress electroconvective instabilities. Guided by these principles, the work explores two main directions: (1) achieving reversible, epitaxial single-metal deposition, and (2) enabling controlled co-deposition of binary alloys in aqueous and non-aqueous systems. In alloy systems, techniques like underpotential deposition, anomalous co-deposition or redox inversion are exploited to overcome disparities, leading to compositionally uniform, stable films. Across both cases, steep interfacial gradients can trigger morphological and hydrodynamic instabilities, which this work seeks to mitigate through substrate and electrolyte design.

Traditionally viewed as passive support, the substrate crystallography can actively guide nucleation and growth through lattice matching and interfacial energetics. This concept of substrate-induced electrodeposition introduces a paradigm in which crystal orientation, interfacial strain, and epitaxial relationships between the deposit and the substrate dictate deposit morphology and phase formation. For instance, copper substrates with a high degree of (111) texturing provides an ideal platform for the epitaxial growth of zinc, particularly along its basal Zn(002) plane. This relationship minimizes interfacial energy and promotes planar growth, thereby suppressing morphological instabilities and enhancing plating reversibility. The Zn–Cu system is emblematic of substrate-directed electrodeposition; and this crystallographic registry facilitates coherent nucleation and lateral growth, improving both morphological stability and electrochemical performance. Systematic comparisons between textured Cu(111) and polycrystalline Cu substrates reveal that substrate orientation governs nucleation density, grain alignment, and deposit compactness.

Underpotential deposition (UPD) refers to the electrochemical phenomenon in which a metal (M) deposits onto a foreign substrate at a potential more positive than the Nernst equilibrium potential for M^{n+}/M deposition onto itself. This early-stage nucleation mechanism has garnered significant

attention due to its critical role in shaping the morphology, structure, and uniformity of metal films [14-17]. UPD is fundamentally driven by favorable interactions—such as stronger binding energies or electronic coupling—between the depositing metal and the foreign substrate, which stabilize the adsorbed metal atoms and enable fractional monolayer formation prior to bulk deposition. The scientific importance of UPD spans multiple domains: it provides insights into crystal or cluster growth and interfacial charge-transfer, while also offering practical advantages in electrocatalysis, corrosion inhibition, and surface finishing [18]. From a mechanistic perspective, UPD couples a range of interfacial processes including adsorption, charge transfer, surface diffusion, nucleation, mass transport, and modifications in the electrochemical double layer [19]. The equilibrium properties of UPD—such as monolayer coverage, electrosorption valency, and the potential of zero charge—yield valuable information about particle–substrate interactions and adsorbate structure. Notably, the underpotential shift often correlates with the work function difference between the metal and substrate, reinforcing the dominant role of particle–substrate interactions in determining UPD behavior [20]. In the context of Zn–Cu systems, UPD plays a crucial role in mediating nuclei growth and enhancing deposit quality. Zinc can form a sub-monolayer on copper substrates at potentials significantly more positive than those required for bulk Zn deposition. This initial UPD layer reduces the nucleation overpotential and provides a uniform template that promotes conformal film growth. As a result, UPD serves not only as a tool for structural templating of Zn but also to regulate early-stage deposition kinetics.

Electrodeposition of binary or ternary alloys introduces additional complexity due to disparities in redox potentials, diffusion coefficients, adsorption behaviors, and crystallographic compatibility. In systems like Ni–Co, where the standard redox potentials (–0.25 V for Ni^{2+}/Ni and –0.277 V for Co^{2+}/Co vs SHE) and atomic radii are nearly identical, co-deposition occurs under near-equilibrium conditions without requiring UPD-aided interface templating. However, even in such compositionally symmetric systems, anomalous codeposition—where the less noble metal deposits preferentially—can occur due to surface adsorption effects and intermediate species, such as MOH^+, that locally alter deposition kinetics. In contrast, alloy formation in redox-asymmetric systems such as Zn–Cu ($\Delta E \approx 1.1$ V) necessitates more deliberate interface engineering. Here, UPD enables Zn^{2+} to nucleate on freshly formed Cu surfaces at more positive potentials than its Nernst equilibrium value. This interfacial stabilization facilitates the formation of Cu-rich α-brass

solid solution and compact Zn-rich films at high voltages, bypassing the large redox mismatch. The UPD mechanism not only lowers nucleation overpotentials but also suppresses dendritic morphology, highlighting its broader utility beyond monolayer templating. Together, these contrasting systems illustrate how electrochemical symmetry, nucleation barriers, and substrate interactions dictate alloy deposition pathways. Non-aqueous electrolytes further expand the design space by offering wider electrochemical windows, suppressed hydrogen evolution, and altered solvation environments. These media permit access to metastable phases and solid solution alloys that are otherwise inaccessible in aqueous systems. The distinct ion-pairing and solvation structures in non-aqueous solvents significantly influence kinetics, growth morphology, and alloy stoichiometry, often deviating from Nernstian predictions due to mass transport and kinetic asymmetries. Understanding these electrochemical growth regimes—across both aqueous and non-aqueous media—is essential for constructing predictive models and tailoring processing windows for high-performance, compositionally controlled alloys.

This thesis presents a comprehensive investigation into the mechanisms governing interface-controlled electrodeposition, spanning single-metal deposition, UPD-assisted templating, and solvent-mediated binary alloy solid solution deposition. The work progresses from fundamental principles to increasingly complex systems, beginning with Zn deposition on textured Cu substrates and advancing toward the co-deposition of Zn–Cu in aqueous medium and Ni–Co alloys under both aqueous and non-aqueous conditions. Special emphasis is placed on characterizing how electrochemical parameters, substrate crystallography, and electrolyte composition influence microstructural evolution, phase formation, and electrochemical performance. The results presented herein not only provide mechanistic insights into interface-driven electrodeposition but also demonstrate practical strategies for tuning key parameters—such as applied voltage, current density, electrolyte composition, and substrate crystallinity—to achieve reliable metal and alloy coatings. By integrating crystallographic engineering with electrochemical design, this work advances predictive control over electrodeposited materials and contributes to the rational development of functional metallic systems.

SECTION I: Epitaxial Substrate-induced Electrodeposition

Crystalline materials are inherently anisotropic, and this structural anisotropy often governs key behaviors such as ion transport, morphological evolution, and interfacial stability. However, conventional electrode designs have largely overlooked this anisotropy, relying instead on randomly oriented polycrystalline materials that fail to leverage the directional advantages intrinsic to their crystal structures. Recent insights have revealed that intentionally engineering crystallographic texture—specifically aligning densely packed planes such as the (111) facet of face-centered cubic (FCC) metals—with the principal electrochemical axis (P_{ec}) of the cell can substantially improve performance by enhancing lateral growth, suppressing morphological instabilities, and optimizing charge transport pathways [21]. Such alignment provides a new axis of design freedom in electrode architecture, potentially enabling high-rate capability and greater reversibility without the cost and scalability limitations of single-crystal materials.

Electrodeposits can exhibit varying degrees of crystallographic order, ranging from single crystalline to completely random, or textureless microstructures (Figure I.1). A single crystalline electrode features a continuous, uninterrupted crystal lattice that extends across dimensions comparable to the electrode itself. Such materials display well-defined orientation both out-of-plane and in-plane relative to the electrochemical cell configuration—typical of thin-film electrodes fabricated via epitaxial growth on single-crystal substrates. However, this definition differs from some battery literature where "single-crystalline" refers merely to the lack of secondary agglomeration, even if individual particles are crystalline but not aligned macroscopically [21, 22]. In contrast, a textured polycrystalline electrode consists of multiple grains that may share a preferential orientation along one or more crystallographic axes, often aligning out-of-plane or in-plane with respect to the current collector or cell symmetry. Finally, random polycrystalline or textureless electrodes exhibit no preferred crystallographic orientation; the constituent grains are distributed isotropically, leading to negligible directional dependence. This microstructural category includes most conventional composite or porous battery electrodes. In such systems, the normal direction (ND) relative to the current collector plays a key role in defining any potential orientation reference.

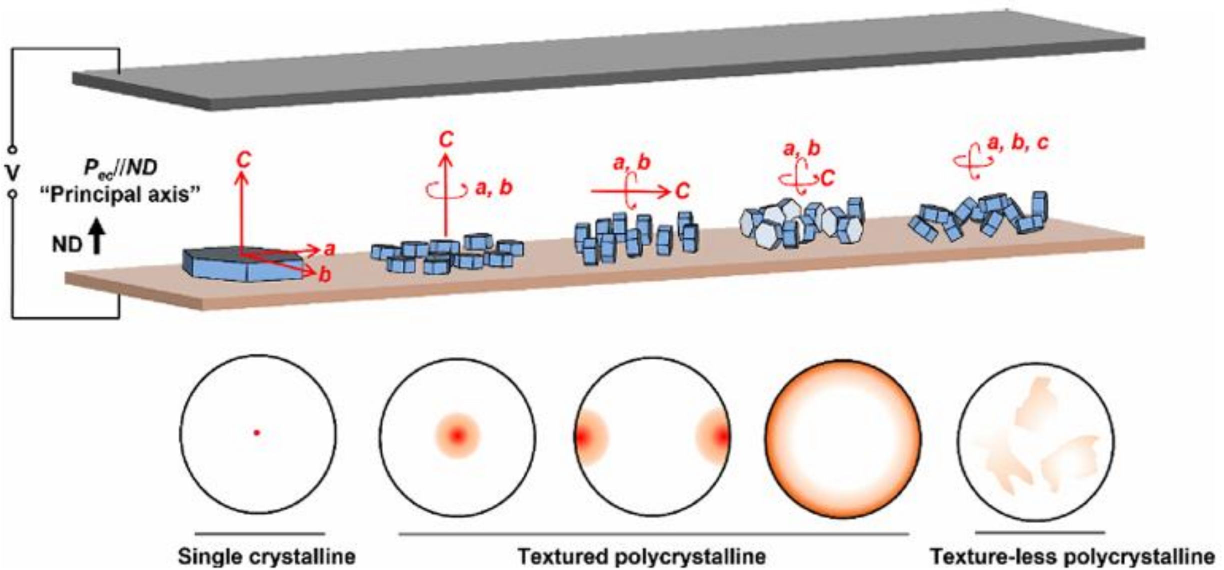

Figure I.1: Representative crystallographic textures of battery electrodes, ranging from single crystalline to textured and textureless. Single crystalline electrodes exhibit large grains with well-defined in-plane and out-of-plane orientation relative to the current collector's normal direction (ND), reflecting the uniaxial symmetry of the electrochemical cell [21].

Epitaxial electrodeposition is a crystallographically directed process in which the substrate surface not only acts as a physical support but also dictates the orientation and growth mode of the deposited layer through lattice matching and interfacial energy minimization. From a thermodynamic perspective, the driving force for such epitaxial alignment is the minimization of the total interfacial energy between the substrate and the deposit. The system tends toward a configuration where the lattice mismatch is minimized and where atomic planes in the deposit can coherently align with those of the substrate to reduce strain energy. When the substrate has a well-defined crystallographic texture, such as Cu(111), it can template the growth of a deposited metal, encouraging it to adopt a specific orientation that mirrors or complements the substrate's structure. This phenomenon is particularly relevant in systems involving metals with closely packed structures, such as FCC copper and HCP zinc. The Cu(111) surface provides a high-density atomic arrangement with minimal surface energy, enabling it to serve as a preferential template for the alignment of Zn(002) planes during electrodeposition. Based on the concept demonstrated by Zheng & Archer (21), Zn films deposited on Cu(111) are expected to develop a strong (002) texture due to the symmetry-aligned Pec//Pc configuration, in which the principal axis of electrochemical

operation coincides with the low-energy basal planes of both materials (Figure I.2). The lattice arrangement promotes coherent interfacial nucleation and directional grain growth, suppressing out-of-plane morphological instabilities and enabling compact, reversible Zn plating/stripping.

Electrochemical reactions fundamentally rely on the coupled transport of ions and electrons [23-25]. These transport phenomena are characterized by two key parameters: diffusivity (D) for ion movement and conductivity (σ) for electron flow. For intercalation-type layered materials (such as graphite or transition metal dichalcogenides), ion diffusion occurs preferentially within the basal planes rather than between layers. The highest diffusivity direction lies parallel to the layered planes, while out-of-plane diffusion is minimal unless facilitated by structural defects [26, 27]. As shown schematically in Figure I.2 (B), the orientation of the electrode relative to the electric field—whether Pec is aligned with the basal plane (Pc) or with the stacking direction (Sc)—strongly influences ion transport efficiency. When Pec is parallel to Pc (basal plane), both the electric field and the ion concentration gradient are directed along the slow-diffusing axis, which limits ion mobility. In such configurations, ions must enter through the edges of the crystals, significantly increasing the required transport path. This introduces cumulative tortuosity, especially as electrode thickness increases, thereby impeding effective ion penetration [23, 28]. Based on these considerations, aligning Pec with the stacking direction (Pec // Sc) rather than with the basal plane (Pec // Pc) is more favorable for intercalation materials. This crystallographic alignment enhances in-plane ionic diffusion while reducing transport barriers caused by tortuous pathways. For metallic anodes (such as zinc), the electrochemical process involves reversible metal deposition and dissolution. The objective shifts to promoting thin, dense metallic films with preferential lateral growth parallel to the substrate surface. This requires suppressing three-dimensional growth modes that can lead to dendrite formation. Optimal morphology control is achieved when the most densely packed crystallographic plane is oriented parallel to the electrode interface (Pec // Pc), encouraging compact, uniform deposition rather than irregular growth perpendicular to the surface. These contrasting requirements demonstrate that optimal crystallographic alignment depends critically on the underlying electrochemical mechanism: intercalation processes favor orientations that maximize in-plane ion diffusion (Pec // Sc), while plating processes favor orientations that promote controlled lateral metal growth (Pec // Pc).

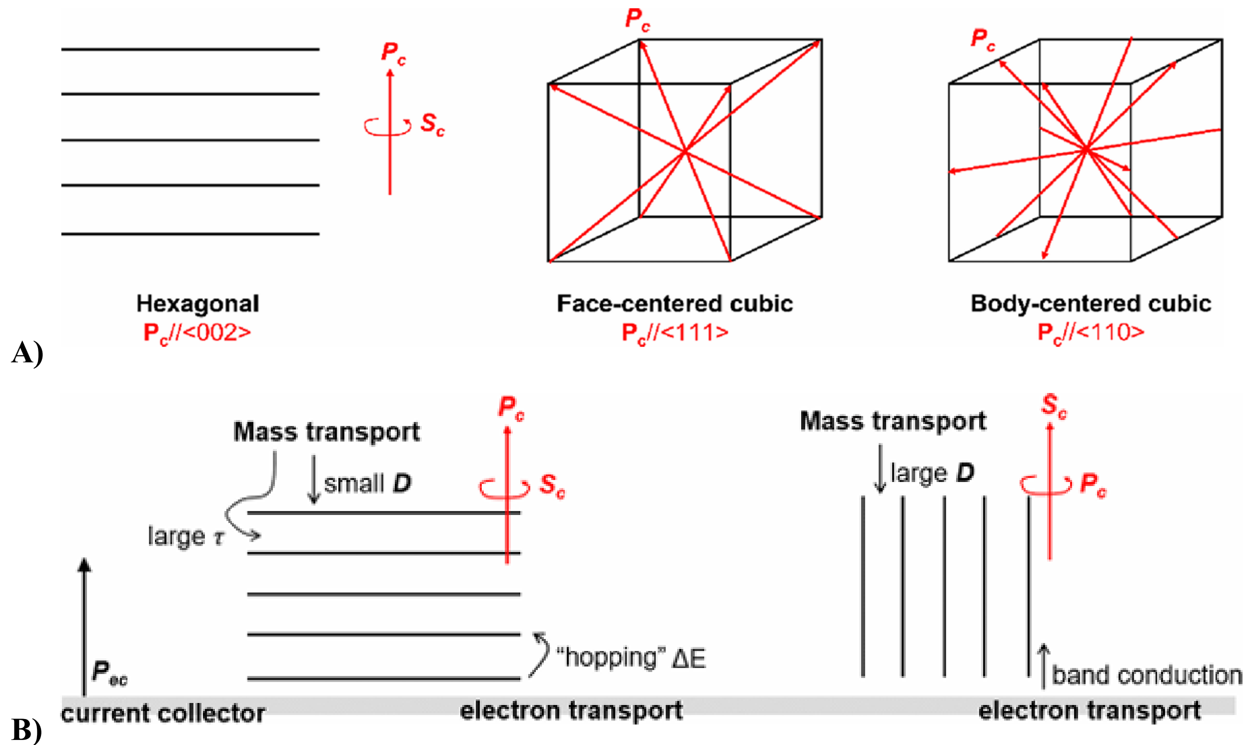

Figure I.2: (A) Definition of principal crystallographic axes in electrode materials: Pc is normal to the densest-packed planes, while Sc represents directions normal to less densely packed planes. (B) Anisotropic transport in crystals: Schematic showing mass and electron transport in crystallites aligned with the electrochemical cell axis (Pec), comparing Pec // Pc (left) and Pec // Sc (right) [21].

Importantly, the findings show that epitaxial alignment minimizes nucleation barriers and facilitates lateral coalescence of Zn grains, ultimately reducing non-planarity. The study also highlights the role of interfacial energy and lattice symmetry in driving the orientation relationship, suggesting that even partial texture in the substrate can induce directional growth if it aligns energetically favorable planes [29]. Collectively, these observations affirm that substrate-induced epitaxial electrodeposition is a viable and scalable strategy to engineer textured uniform Zn layers. By leveraging substrate crystallography—particularly Cu(111)—the deposition process can be tailored to yield anisotropic films with superior electrochemical performance, thereby establishing the foundation for durable and dendrite-free metal anodes. The research discussed in the subsequent sections of this thesis builds upon this emerging paradigm by developing and characterizing (111)-textured copper substrates as platforms for controlled Zn electrodeposition and interfacial engineering, thereby harnessing the anisotropic properties of FCC Cu in a scalable & manufacturable form.

I.1 The Most Stable Crystal Facet of Copper for Planar Zinc deposition

In electrochemical cells, the directional response of crystalline materials to external stimuli, such as applied potential and ion flux, is profoundly influenced by their crystallographic orientation [21, 23]. For metal anodes that undergo plating and stripping at the solid–liquid interface, aligning the electrode's basal plane (P_c) with the electrochemical principal axis (P_{ec})—a condition denoted as $P_{ec}//P_c$—has been shown to promote lateral crystal growth, suppress out-of-plane protrusions, and mitigate morphological instabilities during cycling [28]. In FCC metals like copper, the (111) plane is the most densely packed, exhibiting both the lowest surface energy and the highest symmetry. As such, substrates with out-of-plane (111) texture are considered optimal templates for guiding the morphology of metal deposits such as zinc. Theoretical considerations, reported later in this section, support the notion that textured Cu(111) substrates can stabilize electrodeposition by favoring compact, planar Zn growth, reducing dendritic propagation, and enabling reversible cycling. This thesis employs mechanically and thermally induced (111)-textured Cu substrates to evaluate the $P_{ec}//P_c$ alignment principle, thereby establishing a robust foundation for controlled epitaxial growth and interface engineering in Zn-based anodes.

Although various epitaxial substrates for zinc metal batteries have been identified, there remains a debate over which zinc facet and which substrate facet are optimal. Some assert that Zn(002) is the superior zinc facet, [30, 31] while others advocate for Zn(1011), some claim Cu(220) [32] is the optimal substrate facet for Zn growth, while others favor or Cu(111) [33, 34]. Ongoing dispute is likely rooted in the absence of high-quality single-crystal Cu substrates and a systematic understanding of the epitaxial growth processes for various zinc facets. To understand the facet-dependent variations in zinc nucleation, it is essential to consider the differences in surface diffusion energy barriers across copper crystallographic planes. Although the distribution of Zn^{2+} ions is relatively uniform on flat single-crystal Cu surfaces, the mobility of reduced Zn atoms varies with facet orientation. This difference governs how easily atoms diffuse and form nuclei, leading to distinct nucleation behaviours even under identical electrochemical conditions. Figure I.1.1 illustrates the post-reduction sequence during Zn electrodeposition, where

Zn^{2+} ions are first reduced to neutral Zn^0 atoms on the copper substrate, followed by surface diffusion and aggregation into stable nuclei. The efficiency of this process—and ultimately the uniformity of the deposit—is determined by the energy landscape associated with each Cu facet. Density functional theory (DFT) calculations show that Cu(111) has the lowest diffusion energy barrier favoring a uniform zinc layer formation [35], and that these Zn facets are the most thermodynamically favorable for their respective Cu facets (Figure I.1.2), aligning with the presumed epitaxial relationships.

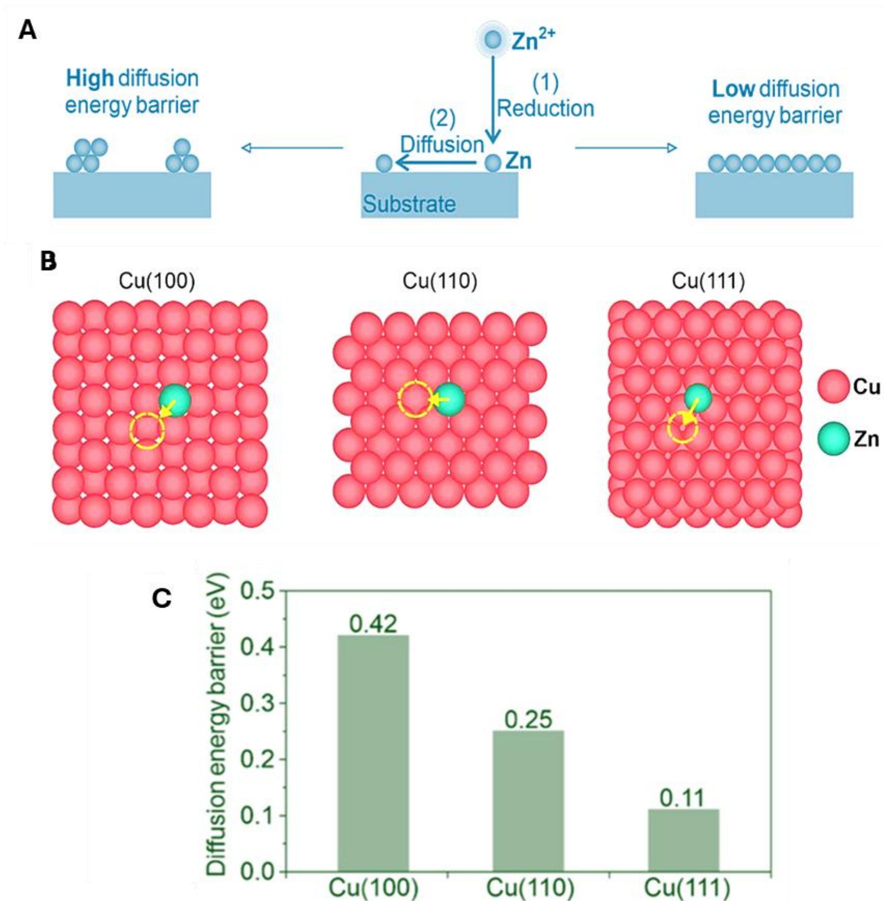

Figure I.1.1: (a) Schematic illustrating the role of diffusion energy barriers in zinc nucleation. (b) Diffusion pathways of a zinc atom on various Cu crystal facets used for energy barrier calculations. (c) Example energy profile for zinc diffusion on the Cu(100) surface. (d) Computed diffusion energy barriers for zinc atoms on different Cu facets [36].

This theoretical insight supports the observed epitaxial patterns. To quantitatively evaluate the thermodynamic feasibility and orientation selectivity of Zn deposition on various copper crystallographic surfaces, the interfacial and surface energies of multiple Zn and Cu facet combinations have been compared [35, 36]. The interfacial energy between Zn(0002) and Cu(111) is –0.1902 J/m^2, which is not only the lowest among potential Cu–Zn combinations, but also the only negative value, indicating spontaneous and energetically favorable interfacial formation. In contrast, all other Zn–Cu facet combinations, including Zn(0002) on Cu(100) (0.2265 J/m^2) and Cu(110) (0.3704 J/m^2), exhibit significantly higher and positive interfacial energies, denoting less favorable interactions. Further supporting this, Zn(0002) possesses the lowest intrinsic surface energy (0.334 J/m^2) among all Zn facets, favoring its natural exposure during growth. Simultaneously, Cu(111) exhibits the lowest surface energy (1.339 J/m^2) among the low-index Cu planes, which not only enhances its thermodynamic stability as a substrate but also promotes coherent epitaxial templating [36]. Taken together, the low surface energies and uniquely negative interfacial energy for the Zn(0002)/Cu(111) interface strongly affirm that this configuration is the most optimal for achieving uniform, basal-oriented Zn deposition with high interfacial stability. This energetic alignment corroborates later experimental findings of preferential Zn(0002) texture on Cu(111) substrates and provides a foundational thermodynamic basis for the observed epitaxial growth behavior.

The closest-packed planes are typically associated with the lowest density of unsaturated surface bonds, minimal surface energy, and enhanced resistance to parasitic reactions in aqueous battery environments [37, 38]. This is particularly relevant for hexagonal close-packed (HCP) zinc, where theoretical and computational studies suggest that deposition with the (002) plane oriented parallel to the electrode surface results in the highest energy barrier for the hydrogen evolution reaction (HER) [39]. Since HER is known to generate gas bubbles that obstruct electron and ion transport, alter local pH, and reduce accessibility to active electrode surfaces, it leads to pronounced capacity fading during battery cycling [40-42].

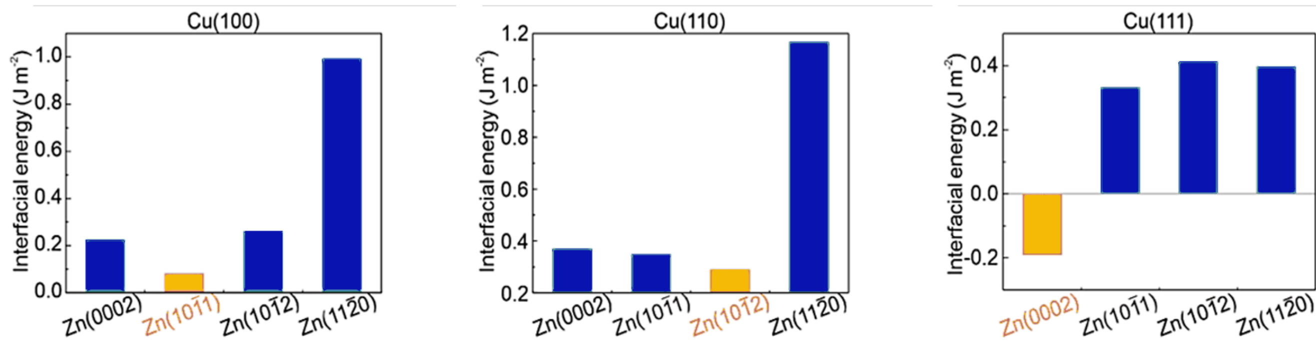

Figure I.1.2: Theoretically computed Zn-Cu interfacial energies' comparison, where four typical Zinc facets [Zn(0002), Zn(101$\bar{1}$), Zn(101$\bar{2}$), Zn(112$\bar{0}$)] were selected as the candidates to interact with copper facets [35, 36].

The crystallographic orientation of the Cu(111) surface plays a critical role in governing both its deformation behavior and its suitability as a substrate for epitaxial growth. Figure I.1.3 illustrates the geometric relationship between Cu(111) and Zn(002) planes in the context of epitaxial alignment. The Cu(111) surface, being the most densely packed plane in the FCC crystal structure, facilitates slip primarily along the {111}⟨110⟩ systems—considered the dominant slip systems in FCC metals due to their low critical resolved shear stress [29, 43]. Furthermore, the angle between Cu(111) and Cu(100) planes is ~54.8°, as per the standard crystallography of FCC lattices. This angular relation defines the preferred shear directions and directly influences how stress is transmitted across the substrate during compaction and epitaxy. In Figure I.1.1 panel (A), the in-plane angle $\Delta\Phi = 60°$ between the Cu(111) and Zn(002) planes reflects a lattice-matched epitaxial relationship where slip activity in Cu may help mediate strain transfer to the Zn overlayer. The dense atomic packing and close interplanar spacing of Cu(111), combined with its favorable slip geometry, renders it a favorable substrate for controlling lattice orientation, mitigating interfacial mismatch, and facilitating anisotropic deposition processes during Zn electrodeposition.

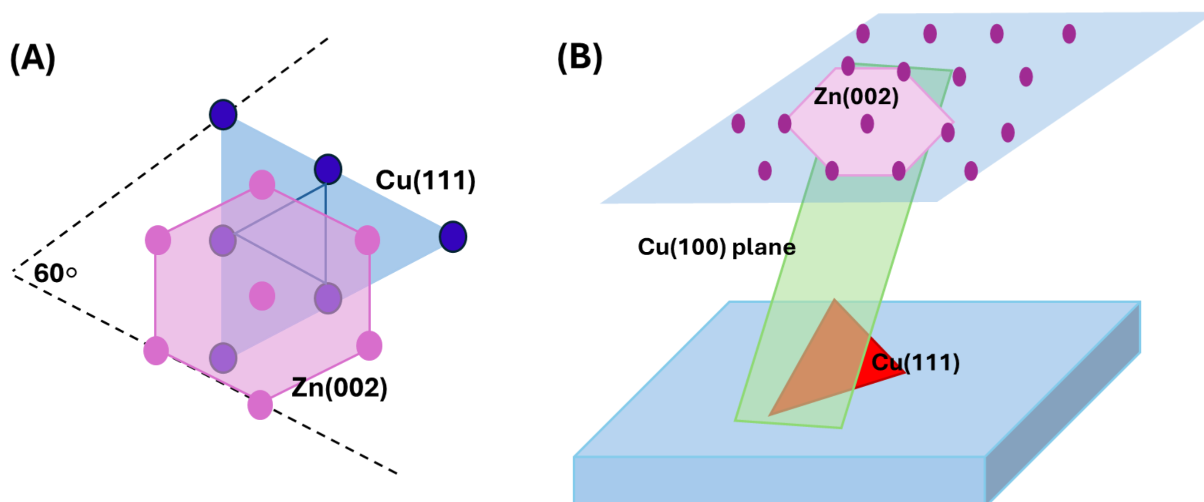

Figure I.1.3: (A) Illustration of Cu (111) and Zn (0002) planes intersecting their respective unit cells, with the in-plane angular difference (ΔΦ) between them determined as 60°. (B) 3D schematic highlighting the in-plane alignment (ΔΦ) between epitaxially matched Cu (111) and Zn (0002).

Additionally, among the basic crystal facets of Cu, the (111) facet shows the minimum lattice mismatch (~5%) with Zn(002), as shown in Figure I.1.4. Therefore, developing electrolytic Cu foils with highly preferred [111] orientation as current collectors is of fundamental and practical interest as substrates for dendrite-free Zn anodes with high reversibility [43]. The Zn(002) facet, which corresponds to the basal plane of hexagonal close-packed (HCP) zinc, is widely recognized as the most stable crystallographic orientation for Zn electrodeposition due to its high atomic packing density and lowest surface energy. When deposited on a Cu(111) textured substrate, this facet exhibits good morphological stability and preferential lateral growth. The Cu(111) plane, as the most densely packed facet of the face-centered cubic (FCC) lattice, offers both crystallographic symmetry and minimal interfacial energy mismatch with Zn(002), creating an ideal template for epitaxial alignment. This alignment realizes the Pec//Pc condition, where both the substrate and deposit have their basal planes oriented parallel to the electrode normal, minimizing vertical protrusions and suppressing out-of-plane growth.

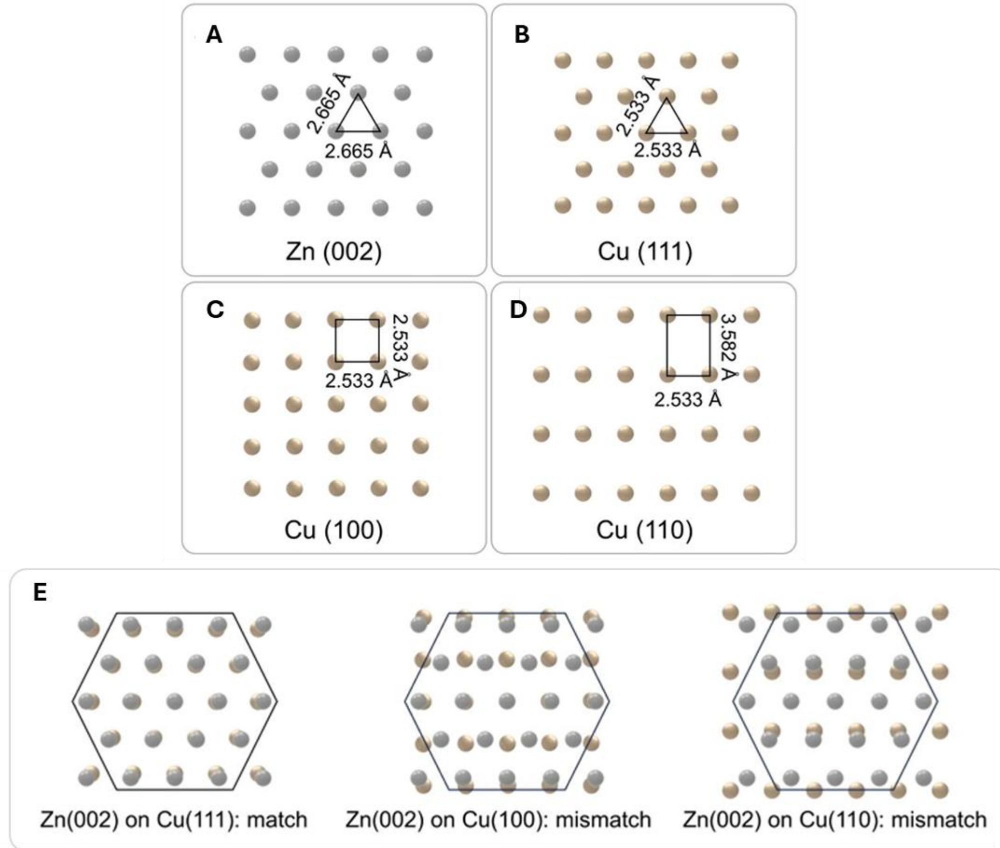

Figure I.1.4: Atomic arrangement in A) Zn(002), B) Cu(111), C) Cu(100), and D) Cu(110); (E) Interface models for the (002) facet of Zn on the three fundamental facets of Cu.

The out-of-plane orientation is preserved due to the low-energy preference of Zn(002), while the in-plane rotation accommodates the mismatch between the HCP and FCC structures. As discussed earlier, such orientation control is critical to achieving uniform plating/stripping and enhancing coulombic efficiency in rechargeable Zn systems [23, 24]. Moreover, the presence of Zn(002) on Cu(111) satisfies the thermodynamic drive for surface energy minimization and promotes planar coalescence of nuclei. Zinc dendrite growth typically exhibits both thermodynamic and kinetic favorability due to electric field concentration and enhanced deposition rates at protruding tips. Studies have shown that zinc dendrites developing in slightly acidic or neutral electrolytes manifest as two-dimensional hexagonal structures originating from hexagonal close-packed crystallography, with dimensions varying based on electrolyte composition and operational parameters, reflecting the minimal free energy associated with the (002) plane exposure in

hexagonal metals. Consequently, when the careful equilibrium between growth suppression and deposition is disrupted in conventional methods, dendrites tend to propagate continuously due to existing potential gradients. Our approach involves engineering zinc deposition layers at the atomic level using copper current collectors with predominant (111) crystallographic orientation. This methodology embraces controlled non-planar growth while directing their propagation orientation, rather than attempting complete dendrite elimination.

I.2. Fabrication of Single (111) Crystalline Textured Copper Substrates

Achieving crystallographic texture in metallic electrodes through scalable fabrication methods is critical for their widespread integration in electrochemical energy storage devices. Among the various approaches, mechanical deformation techniques—such as compaction, rolling, and pressing—have proven particularly effective for inducing orientation alignment in high-density crystal planes like Cu(111) [21]. In this work, we employ a hydraulic pressing process capable of delivering up to 10 metric tonnes of uniaxial force to compress Cu metal powders of varying particle sizes into dense, consolidated substrates. To induce a strong (111) texture through this method, it is essential to understand the deformation mechanisms in face-centered cubic (FCC) metals. Copper primarily deforms through activation of the $\{111\}\langle 110\rangle$ slip systems, where the $\{111\}$ planes represent the most densely packed crystallographic planes and the $\langle 110\rangle$ directions offer the least resistance to dislocation motion (Figure I.2.1). Under uniaxial compression in a confined die, the system undergoes plane strain deformation, where lateral strain is restricted, concentrating plastic flow in the axial and tangential directions. These conditions promote shear stress development along $\{111\}$ planes, triggering coordinated plastic slip, grain rotation, and reorientation. As pressing proceeds, this strain-induced realignment encourages the (111) planes to align parallel to the loading axis, reducing intergranular misorientation and driving the formation of large-area, low-energy textured domains. The resulting out-of-plane (111) texture is a direct consequence of the material's tendency to evolve toward thermodynamically and kinetically favorable configurations during deformation. To further enhance this texture, a post-pressing annealing step was implemented under an Argon atmosphere. Thermal treatment facilitates strain relaxation, grain growth, and orientation-selective coarsening, reinforcing the

prevalence of the stable Cu(111) facet. As demonstrated in prior studies [43], such deformation-driven and thermally assisted processes enable dramatic grain enlargement—from tens of micrometers in commercial polycrystalline foils to millimeter-scale grains in annealed Cu(111) samples—without requiring expensive single-crystal templates. Thus, our combined press–anneal strategy provides a low-cost, scalable pathway to engineer highly textured Cu(111) electrodes with superior morphological and crystallographic features, ideally suited for epitaxial metal deposition in advanced electrochemical systems.

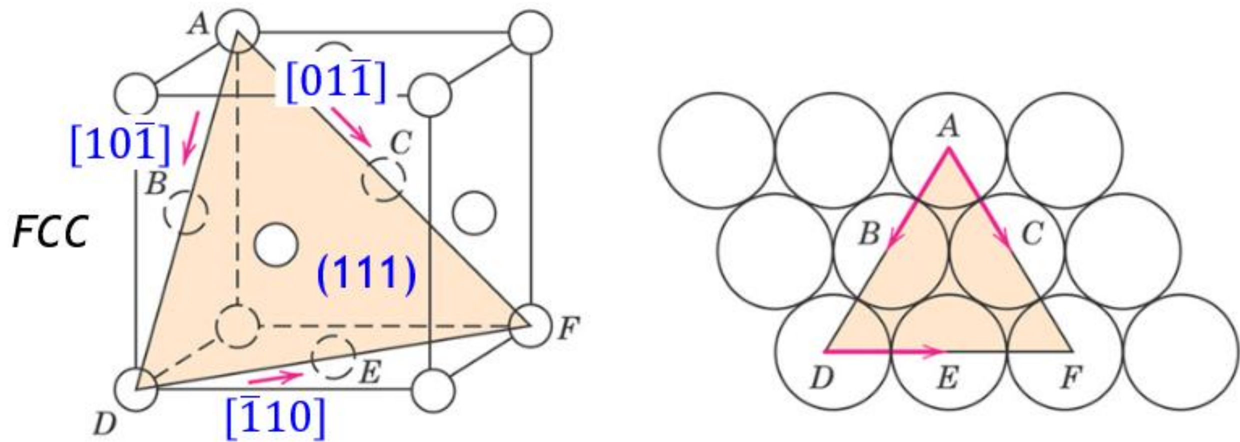

Figure I.2.1:Slip planes and directions of dislocation slip in the FCC Copper Crystal

For a wide range of metals, the most densely packed crystallographic planes tend to coincide with the primary slip planes [44, 45]. Consequently, scalable metallurgical techniques such as cold pressing and accumulative roll bonding [46, 47-49], which impart significant shear strain throughout bulk polycrystalline samples, can be effectively used to induce preferential texturing. At sufficiently high strain levels, these processes facilitate the emergence of the primary slip plane as the dominant crystallographic orientation at the surface. When a single solid metal particle is compressed under normal load, it undergoes plane strain deformation; upon reaching critical strain levels, plastic slip is initiated along the close-packed basal planes. In assemblies of multiple particles, this deformation leads to plastic flow, pore elimination, and eventual consolidation, resulting in a macroscopic material exhibiting strong crystallographic texture [50-52]. In the case of FCC copper, such deformation is expected to promote significant alignment along the (111) planes.

To experimentally validate this approach, we used a manual hydraulic laboratory press capable of exerting up to 10 metric tonnes of uniaxial load to introduce varying degrees of in-plane shear into Cu powder particles. The textured Cu substrates were produced through this "strain-induced texturing" process. A separable pump-type hydraulic press (MTI Corporation) and a 0.5" (12.7 mm diameter) dry-pressing die set from MSE Supplies were employed (Figure I.2.2). The procedure involved assembling the die column by first placing the die sleeve on the base plate, inserting a spacer, and then adding the copper powder. A second spacer was placed atop the powder, followed by the plunger. All samples were subjected to a maximum applied load of 10 metric tonnes. For the subsequent XRD analysis, the dwell time under pressure was varied between immediate release (instantaneous pressing) and extended compression up to 30 minutes.

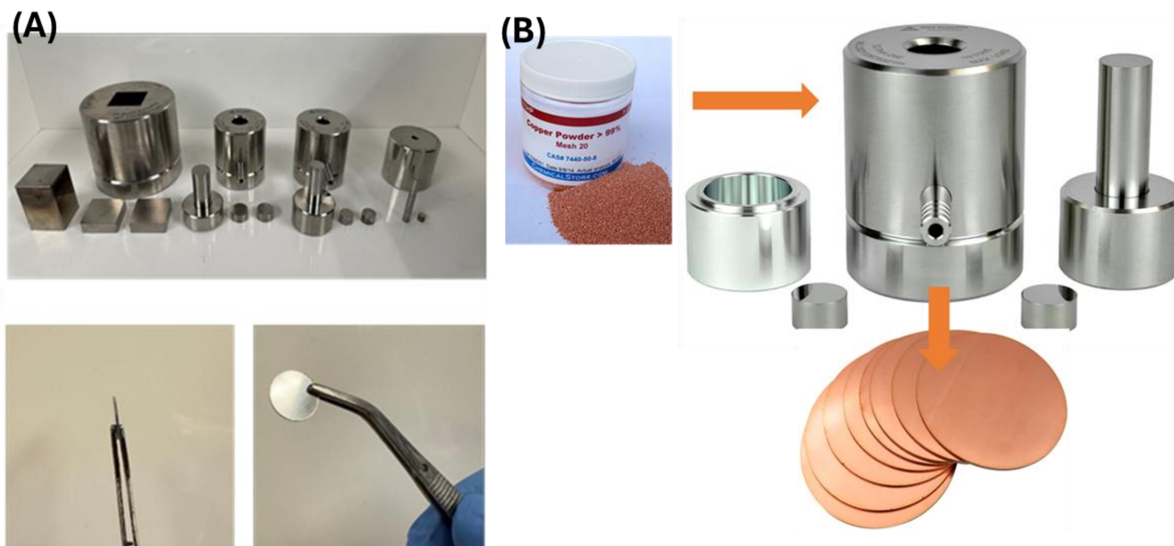

Figure I.2.2: Image of hydraulic press (A) with different pressing dies (B) pressed free standing Cu Substrate

In the specific case of face-centered cubic (FCC) copper, the mechanical compression of Cu powders would lead to the development of highly oriented (111) textures along with planar morphology as compared to commercial polycrystalline copper foil (Figure I.2.3). To evaluate this practically, a hydraulic laboratory press was applied which can apply uniaxial loads higher than 10T, generating substantial planar shear on copper metal particles. Under uniaxial compression, individual copper particles undergo lateral strain that activates the characteristic $\{111\}\langle 110\rangle$ slip systems of the FCC lattice. As deformation progresses, additional slip systems are engaged,

allowing inter-particle voids to close through particle elongation, rotation, and reorientation. This process facilitates the coalescence of grains along energetically favorable (111) planes, in line with prior studies on FCC metal plasticity and texturing mechanisms [29].

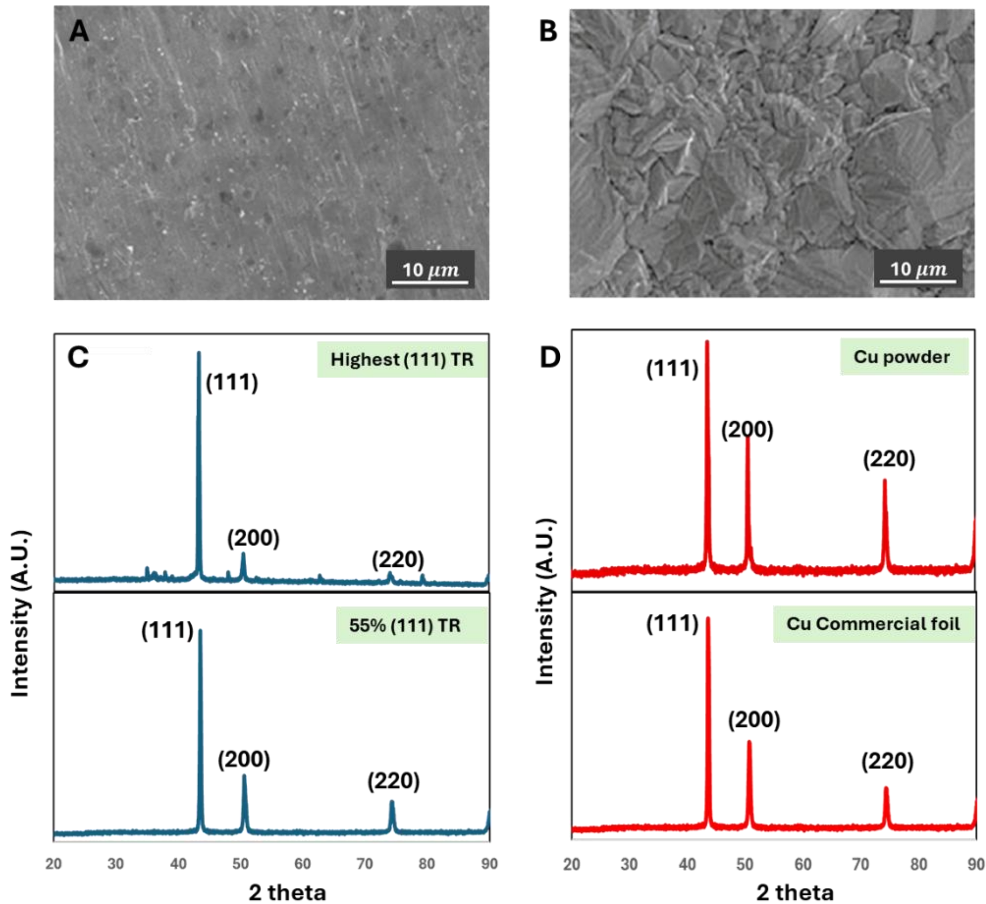

Figure I.2.3: (A and B) SEM image of Textured Cu(111) substrate & polycrystalline Cu foil. (C) XRD spectra of Cu pellet with max (111) TR and 55% (111) TR; (D) XRD of Cu powder and Cu commercial foil.

The degree of lattice reorientation—and thus the extent of (111) texture development—was evaluated as a function of both compression time and applied pressure. We anticipate that the onset and progression of plastic slip, governed by stress and strain parameters such as Hencky strain (ε), directly influences texture formation. XRD analyses conducted at a fixed pressure of 10 T for varying durations (5 to 30 minutes), and at a fixed duration of 5 minutes for increasing pressures (0.5 T to 10 T), confirmed these expectations. Specifically, the intensity of the Cu(111) diffraction peak increased from 220.6 to 325 A.U. (Arbitrary Unit) as the compression time increased from 5

to 30 minutes (Figure I.2.4 (A)). The corresponding texture ratio—defined as the intensity of Cu(111) divided by the sum of all major Cu peak intensities—rose from 34.67% to 75.30%. Similarly, when pressure varied at a constant time of 5 minutes, the Cu(111) peak intensity increased from 149.56 at 0.5 T to 243.67 at 10 T, while the texture ratio improved from 29.48% to 49.36% (Figure I.2.4 (B)).

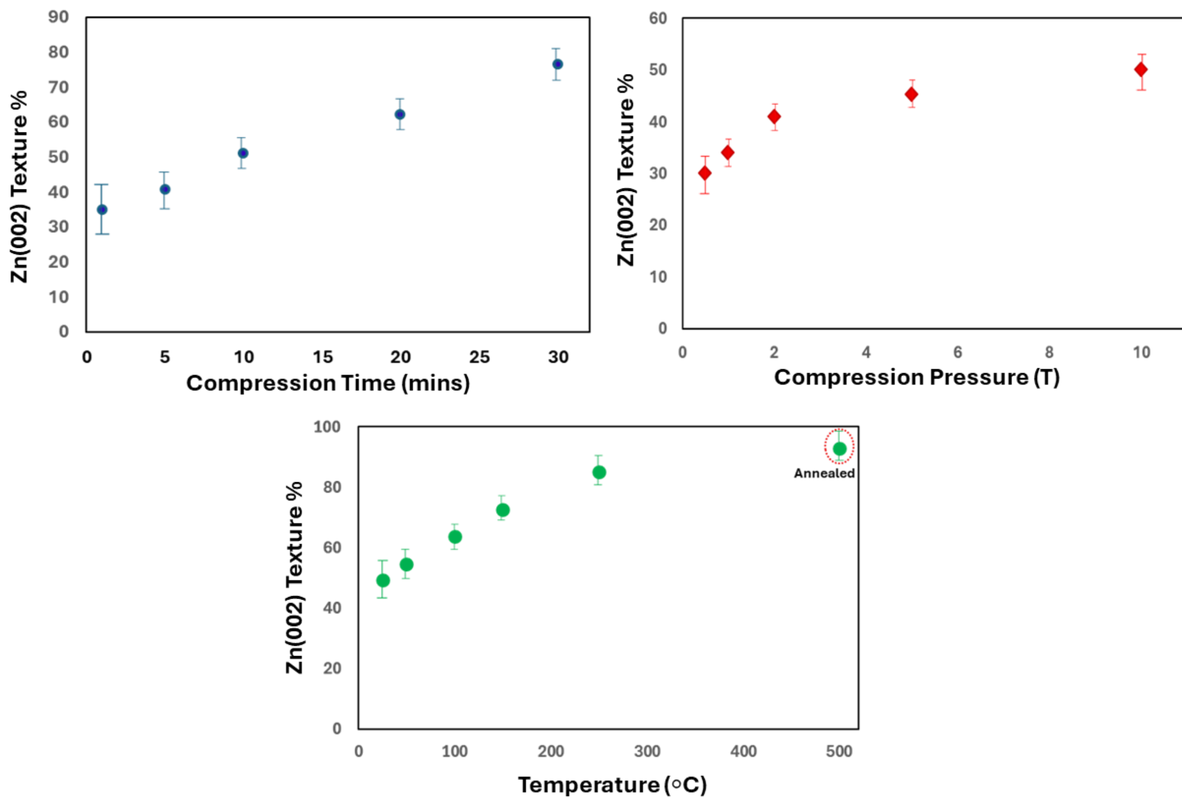

Figure I.2.4: XRD analysis of Cu powders as a function of compression time. Ratio of (111) peak relative to all other XRD peaks as a function of (A) Compression Time; (B) Applied Pressure; & (C) Applied Temperature during compaction

These trends are consistent with the crystallographic and mechanical expectations for FCC metals. The {111} planes are the most densely packed and exhibit the lowest surface energy, making them thermodynamically favorable for alignment during deformation. The observed enhancement in texture with increasing time suggests a cumulative effect of plastic flow and grain rotation, possibly supported by dislocation glide and dynamic recovery processes. In the case of pressure variation, the sharp increase in Cu(111) orientation at higher loads aligns well with Schmid's law [53], which requires that the applied load surpass the critical resolved shear stress to activate slip.

These findings confirm that the texturing mechanism is strongly deformation-driven and can be controlled through process parameters such as pressure and time. Together, these findings demonstrate that mechanical compaction of Cu powders—when optimized for particle size, pressure, and time—offers a practical and controllable route to engineer free-standing substrates with highly developed Cu(111) texture.

To further investigate the role of thermal activation on crystallographic texturing, a series of XRD measurements were conducted at fixed compression conditions (10 T pressure, 5-minute duration), while varying the substrate temperature from room temperature (25 °C) up to 250 °C, as well as a post-compaction annealing treatment. The results, presented in Figure I.2.4 (C), reveal a clear trend of progressive enhancement in Cu(111) orientation with increasing temperature. At 25 °C, the Cu(111) peak intensity was 243.67 with a texture ratio of 49.36%. As the temperature increased to 100 °C, 150 °C, and 250 °C, the Cu(111) peak intensities rose to 284, 314 and 547, respectively, while the corresponding texture ratios improved to 63.82%, 72.65%, and 84.96%. The most significant enhancement in crystallographic orientation was observed in the sample annealed at 500 °C for 10 hours under an argon atmosphere, following compaction at 10 T for 5 minutes. This sample exhibited a Cu(111) peak intensity of approximately 650 A.U. and a corresponding texture ratio of 92.71%. When the compaction duration was extended to 30 minutes prior to annealing, the Cu(111) texture ratio further increased to ~96%, approaching near-single-orientation dominance (Figure I.2.3 (C)). These observations are consistent with thermomechanical models of texture evolution in FCC metals. Elevated temperatures reduce the critical resolved shear stress, enabling more facile activation of the {111}⟨110⟩ slip systems. Concurrently, thermal energy promotes dislocation mobility, recovery, and sub-grain rotation, all of which enhance the alignment of grains along low-energy crystallographic orientations such as (111). The pronounced increase in texture ratio at higher temperatures thus reflects the combined effects of thermally assisted plastic deformation, enhanced atomic diffusion, and orientation-selective grain coarsening. Moreover, the progressive decrease in the relative intensities of higher-energy planes such as Cu(200), Cu(220), Cu(311), and Cu(222) confirms the suppression of competing orientations.

To further improve crystallographic ordering and lateral grain growth, an independent annealing protocol was employed to produce large-area Cu(111) facets. Specifically, a pressed Cu

substrate was subjected to annealing at 500 °C, under a reducing atmosphere of Argon supplied at 2 psi, inside a Quartz Tube Furnace (GSL-1100X, MTI Corporation) as shown in Figure I.2.5. The heating ramp rate was 5 °C/min, and the temperature was held at 500 °C for 10 hours before natural cooling. The formation of Cu(111) during annealing is governed by surface energy minimization, favoring the growth of the thermodynamically stable facet. As characterized in Figure I.2.3, the annealed Cu pellet exhibited highly uniform orientations dominated by (111) facets. Together, these results demonstrate that thermal activation—both during compaction and through post-processing annealing—plays a pivotal role in driving orientation selection, lattice reconfiguration, and grain growth. When combined with optimal pressure, time, and particle size selection, thermal processing provides an effective and scalable route for fabricating highly oriented Cu(111) surfaces, perfect for epitaxial growth and interface engineering in zinc-batteries.

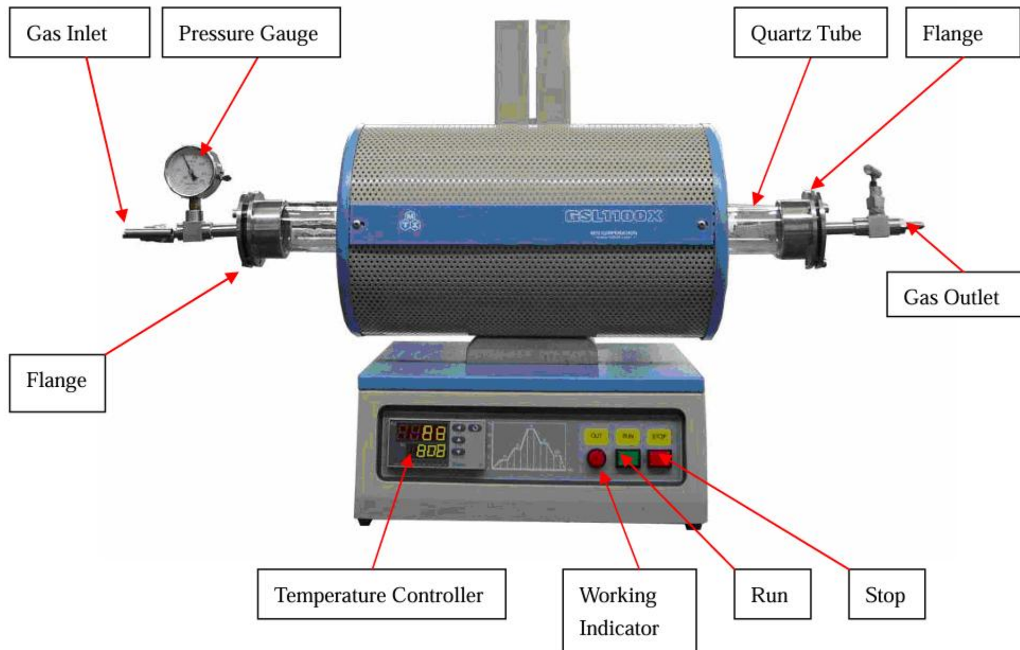

Figure I.2.5: Argon and Quartz tube furnace system used for annealing the prepared Cu pellets.

SECTION II: Evaluating Zn(002) Texture Evolution on Cu(111) & its Electrochemical Performance

The electrodeposition behavior of zinc is profoundly influenced by the crystallographic orientation of the underlying copper substrate—a factor often overlooked in traditional Zn battery research, which tends to prioritize electrolyte composition and surface additives. This section investigates, in detail, the comparative impact of polycrystalline and highly textured Cu(111) substrates on Zn electrodeposition across multiple metrics—ranging from nucleation behavior and texture evolution to electrochemical performance and long-term cycling stability. The motivation for this stems from the critical challenges faced by rechargeable aqueous zinc batteries, particularly the issues of dendritic growth, poor Coulombic efficiency, and morphological degradation during repeated cycling. These instabilities are often rooted in uncontrolled nucleation and anisotropic ion flux near the electrode surface. By using single-crystal-like Cu(111) substrates with controlled surface orientation and atomic-scale order, this study demonstrates that the Zn(002) basal plane can be selectively and uniformly grown via epitaxial templating. This crystallographic guidance not only governs the microstructure and compactness of deposited Zn layers but also facilitates a self-sustaining underpotential deposition (UPD) cycle that drastically improves reversibility and cycle life.

To explore these effects comprehensively, the subsequent section combines electrochemical characterizations, SEM imaging, and XRD-based texture analysis across a wide range of deposition conditions. The findings reveal that Cu(111) substrates consistently promote smoother, planar Zn deposition, suppress dendrite formation, and maintain crystallographic registry over practical film thicknesses. Importantly, these advantages persist even under high current densities and large areal capacities—conditions relevant for real-world battery applications. Collectively, this section establishes a clear link between substrate crystallography and Zn plating performance, presenting Cu(111) as a model host for scalable, high-performance zinc anodes. The insights presented here not only advance the understanding of interfacial control in metal electrodeposition but also offer a pragmatic route toward engineering next-generation Zn-based energy storage systems with enhanced efficiency and durability.

II.1 Comparison of Zinc Electrodeposition on Textured Cu (111) & Polycrystalline Cu

The crystallographic orientation of the copper substrate plays a decisive role in governing the electrodeposition behavior, reversibility, and long-term stability of Zn anodes in aqueous rechargeable batteries. Cyclic voltammetry (CV) revealed striking differences in redox kinetics across the two systems – textured Cu(111) and polycrystalline Cu (Figure II.1.1). The cell with predeposited Zn on Cu(111) electrodes exhibited the highest peak current densities and the lowest overpotentials among the compared substrates, indicating superior charge transfer kinetics and more reversible Zn plating/stripping behavior. These advantages are attributed to the low-energy, densely packed nature of the Cu(111) plane, which promotes uniform nucleation and lateral growth of Zn(002), minimizing morphological instabilities during cycling.

To further investigate the deposition dynamics, chronoamperometry (CA) measurements were conducted at a fixed overpotential of –150 mV (Figure II.1.2). This potential was carefully chosen to provide an optimal balance between thermodynamic driving force and kinetic control, lying just below the equilibrium potential for Zn^{2+}/Zn on Cu. Operating in this mild underlimiting regime avoids mass transport limitations and minimizes hydrogen evolution, thereby allowing surface-controlled processes—such as 2D nucleation, localized Zn^{2+} adsorption, and early-stage surface diffusion—to be distinctly observed. The selected overpotential is sufficiently negative to surpass the nucleation energy barrier, yet moderate enough to prevent uncontrolled 3D growth or dendritic formation, especially on the epitaxy-favourable Cu(111) surface. This electrochemical window enables the resolution of key interfacial events, including induction periods, nucleation site activation, and growth behavior under quasi-equilibrium conditions. Accordingly, –150 mV serves as a thermodynamically and kinetically justified potential for probing the fundamental mechanisms governing Zn electrodeposition. To validate this approach, comparative electrochemical analyses were performed across three substrate types: highly textured Cu (111) and two commercial polycrystalline copper foils, Comm-Cu (I) and Comm-Cu (II). The former (Comm-Cu (I)) has a higher intensity of (111) peak plane as compared to other Cu facets while latter (Comm-Cu (II)) has a higher intensity of the (110) peak as compared to the other peaks. These substrates were evaluated under identical conditions in symmetric and half-cell configurations using a 2 M $ZnSO_4$ aqueous electrolyte. While commercial Cu@Zn substrates showed a continuous increase in

current over time—indicative of uncontrolled 2D surface diffusion and dendritic growth—the Cu(111) @ Zn substrate displayed a brief 2D growth phase (~5 s) followed by stable 3D diffusion-dominated behavior. This transition reflects a more uniform Zn deposition process and is consistent with substrate-induced crystallographic control that guides Zn^{2+} diffusion and incorporation.

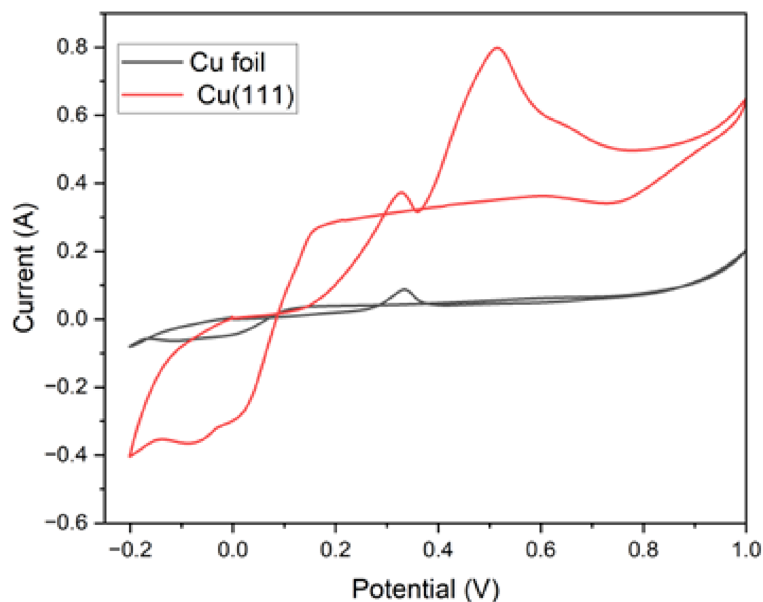

Figure II.1.1: CV curves of Zn plating/stripping on Cu substrates at a scan rate of 2 mV/s.

Linear polarization (LP) measurements provided insights into corrosion behavior (Figure II.1.2). The (111)-Cu@Zn electrode showed a more positive corrosion potential (−0.939 V) compared to Comm-Cu(II)@Zn (−0.947 V) and Comm-Cu(I)@Zn (−0.971 V), suggesting improved resistance to parasitic reactions. This enhanced stability is attributed to the preferential exposure of the Zn(002) facets during electrodeposition on Cu(111), which are chemically more stable than other crystallographic planes. In contrast, cells built on commercial Cu foils failed significantly earlier, highlighting the importance of substrate crystallography for cycle life and reversibility.

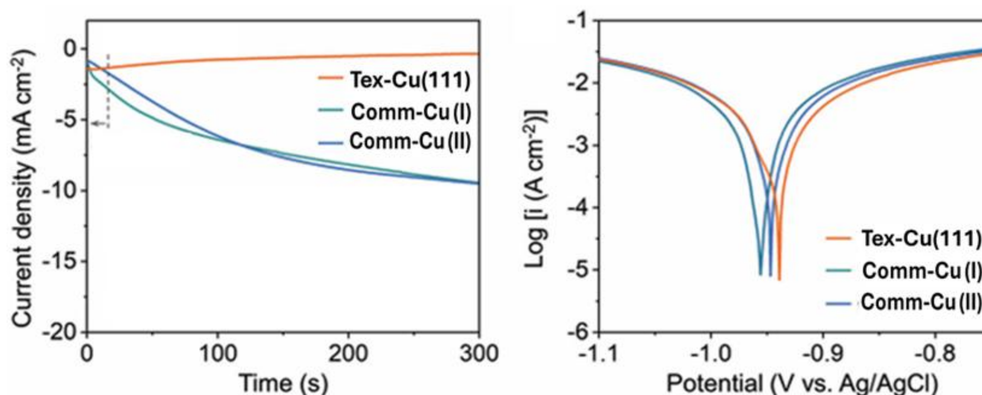

Figure II.1.2: CA curves of different Cu substrates anodes at an overpotential of −150 mV; and the LP curves of different Cu substrate anodes.

The electrochemical behavior was also evaluated through scan rate-dependent CV analyses, where the peak current (Ip) was plotted as a function of voltage scan rate (v). For all Cu substrates under study, a linear relationship (Ip ∝ v) was observed, with high correlation ($R^2 = 0.998$), indicating a pseudo-capacitive response (Figure II.1.3). This suggests that Zn deposition on Cu involves a surface-confined alloying reaction rather than classical diffusion-limited bulk alloying. These findings are supported by observations of "underpotential deposition" (UPD) phenomena on Cu, which arise due to spontaneous Zn-Cu alloy formation and is comprehensively discussed in later section of this thesis. Because these surface alloys have lower Gibbs free energies than pure Zn, they facilitate deposition at potentials more positive than the Zn^{2+}/Zn^0 equilibrium value.

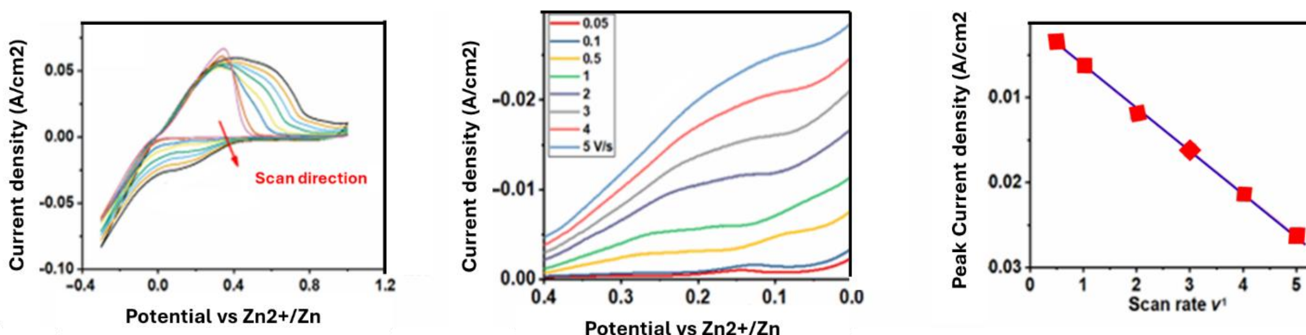

Figure II.1.3: CV scans in the range -0.35 to +1.0 V versus Zn^{2+}/Zn at Cu(111) substrate in 2 M $ZnSO_4$ (aq) electrolyte: (A) CV scans, (B) enlarged plot of CV and (C) plot of peak current density versus scan rate.

The trend in nucleation overpotentials (Commercial-Cu > Cu(111)) also reflects the facet-dependent nature of Zn deposition (Figure II.1.4). Higher nucleation overpotentials, such as those

observed on polycrystalline, correlate with non-uniform Zn growth and an increased fraction of reactive surface area, making them more prone to corrosion. In contrast, Cu(111) exhibits the lowest nucleation overpotential, supporting fast lateral diffusion and compact deposition. This behavior is further explained by the lower Zn^{2+} diffusion energy barrier on Cu(111), which facilitates rapid ion transport across the interface and promotes uniform nucleation. Morphological imaging and diffusion simulations in earlier works confirm that Zn deposits on Cu(111) form dense, continuous films, whereas random or poly-Cu substrates yield dispersed, dot-like clusters. Together, these electrochemical analyses affirm that Cu(111)-textured substrates not only direct the crystallographic growth of Zn but also significantly enhance the plating kinetics, reduce corrosion susceptibility, and extend cycle life. These characteristics make 111-textured Cu a superior host for Zn anodes in practical zinc-based battery systems.

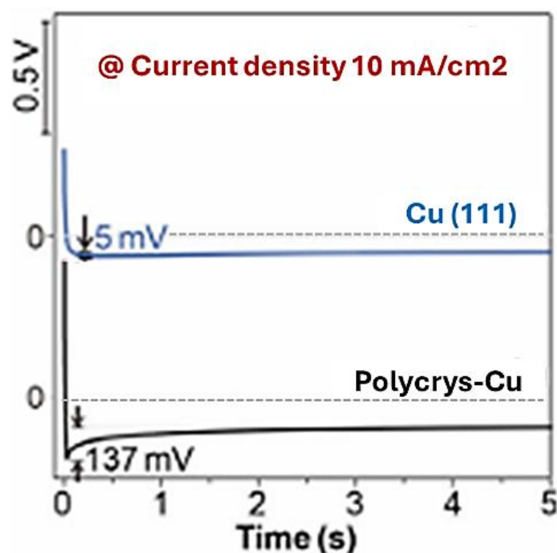

Figure II.1.4: (A) V-t curves for the in-situ zinc deposition onto copper; (B) Nucleation overpotential of zinc plating on different copper surfaces: polycrystalline-Cu & Cu(111).

To systematically investigate the influence of copper substrate crystallography and deposition parameters on the morphology and quality of electrodeposited zinc, we examined the plating behavior on two distinct copper substrates: commercial polycrystalline copper (poly-Cu) and highly oriented single-crystal Cu(111). All experiments were performed in 2 M $ZnSO_4$ aqueous electrolyte, with varying areal capacities and current densities to simulate practical plating conditions for rechargeable Zn-based battery systems. While the substrate plays a crucial role, the

applied current density significantly affects dendritic growth. To better understand the nucleation behavior at the onset of Zn deposition, early-stage plating experiments were conducted at current density of 1 mA/cm² for lower aerial capacity of 0.1 mAh/cm². As shown in Figure II.1.5, highly textured (>85 %) Cu(111) facilitates the formation of uniformly distributed, thin, hexagonal Zn nuclei aligned parallel to the substrate. In contrast, commercial Cu exhibits slanted or vertical nucleation orientations, indicating poor registry and higher energetic variability across its polycrystalline grains. This early-stage alignment on Cu(111) is a crucial precursor to the uniform morphology observed at higher capacities.

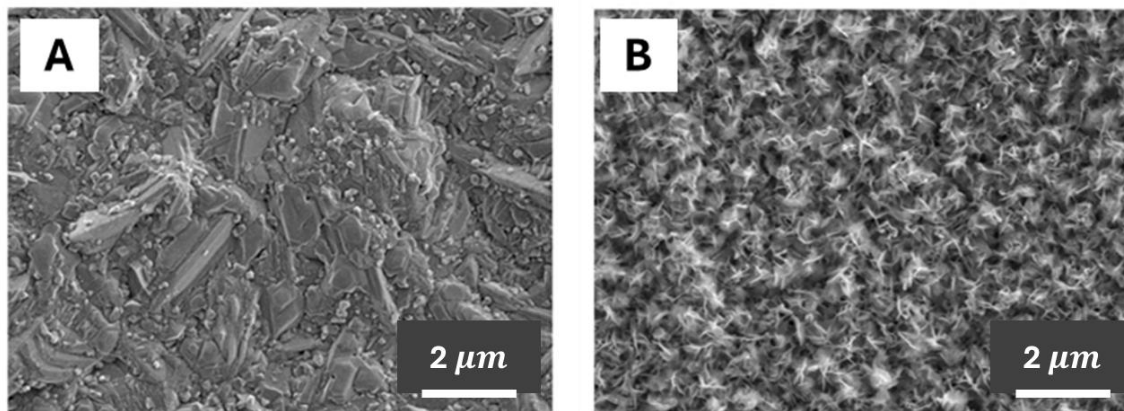

Figure II.1.5: SEM images of Zn deposited on 111-Cu & Cu foil at 1 mA/cm² for 0.1 mAh/cm² to reveal the nucleation behavior.

Upon increasing the deposition capacity to 2 mAh/cm² at the same rate of 1 mA/cm², distinct differences in Zn growth evolution emerge between the two substrates. On commercial Cu, nuclei evolve into blade-like, random structures (Figure II.1.6 (A)), consistent with unstable, diffusion-limited growth. Meanwhile, deposition on Cu(111) forms coaxially stacked hexagonal flakes alongside smaller immature nuclei, reflecting a more ordered and progressive nucleation-growth sequence (Figure II.1.6 (B)). When the deposited capacity is increased further to 5 mAh/cm², the Zn layer on Cu(111) becomes conformal and continuous, dominated by the (002) crystallographic orientation, indicating successful texture evolution driven by the epitaxial interaction (Figure II.1.6 (C)).

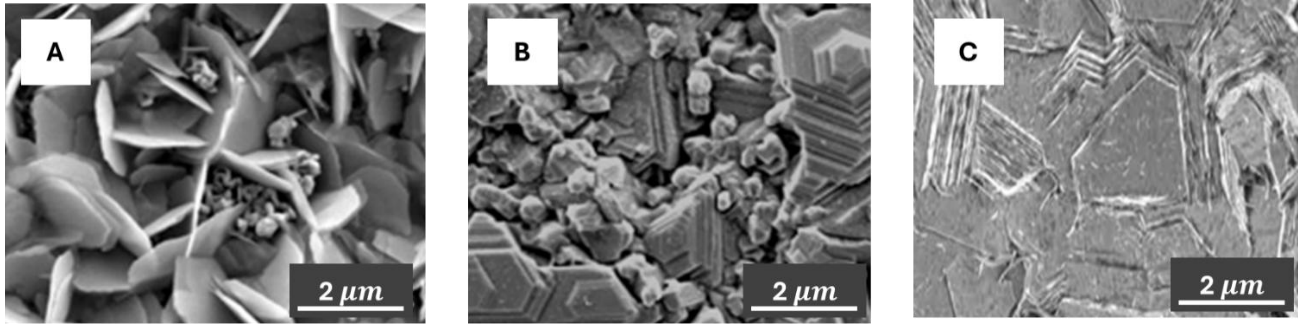

Figure II.1.6: SEM images of Zn deposited on (A) Commercial-Cu, (B) 111-Cu at 1 mA/cm² for 2 mAh/cm² to reveal the nucleation behavior; and (C) 111-Cu at 1 mA/cm² for 5 mAh/cm²

Now, keeping the areal capacity fixed at 1 mAh/cm² subsequent depositions were investigated at a higher current density of 10 mA/cm². As shown in Figure II.1.7 (A), zinc plating on commercial Cu foil resulted in randomly oriented hexagonal flakes, characterized by disoriented crystal alignment and a rough surface topography. The flakes often grew at perpendicular angles, resulting in a uneven top layer. In stark contrast, deposition on Cu(111) substrates led to highly compact, uniformly aligned Zn flakes, all oriented parallel to the substrate surface, even at 10 mA/cm². Figure II.1.7 (B) highlights the dense and ordered Zn layer on Cu(111), indicating strong epitaxial interaction between the depositing Zn atoms and the underlying substrate.

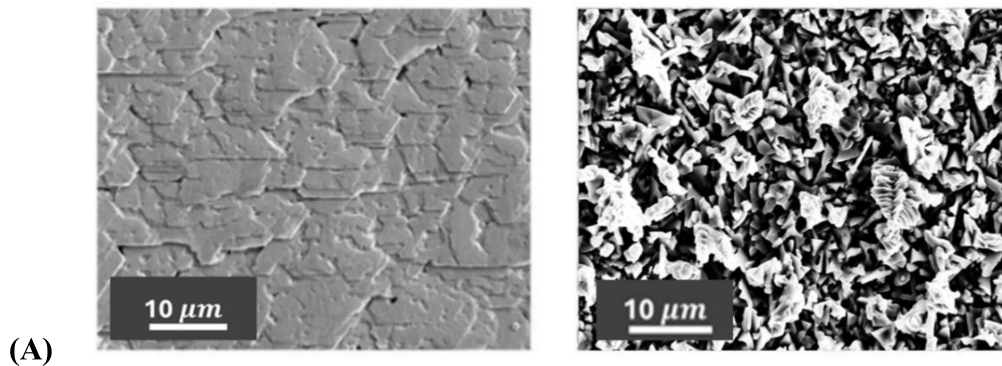

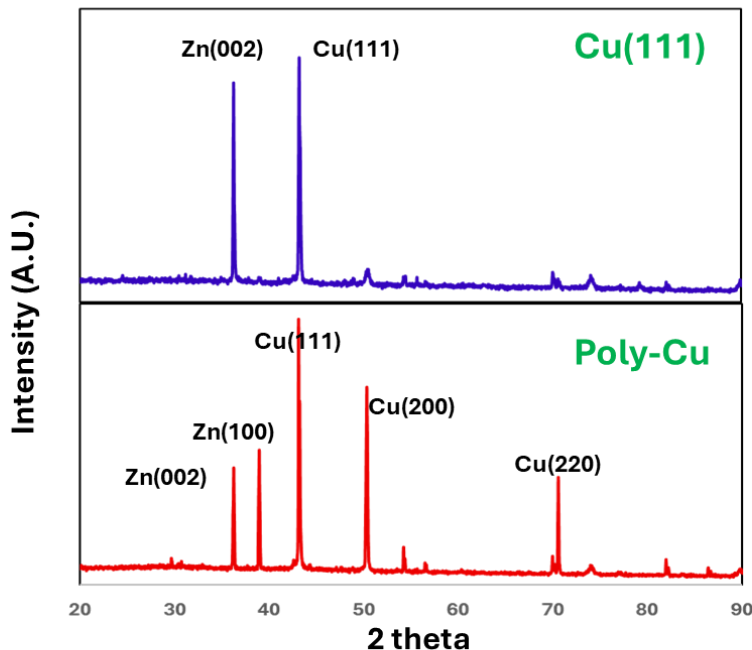

(B)

Figure II.1.7: SEM & XRD images of Zn (1 mAh/cm² @ 10 mA/cm²) onto Cu(111) & Commercial polycrystalline Cu.

Such epitaxial control proves instrumental in suppressing the formation of dendrites—a major cause of short-circuiting and capacity fading in zinc batteries even at high current densities. By leveraging the atomic-level alignment between Zn and Cu(111), it becomes possible to realize continuous, flat Zn plating even at high mass loading. To assess the practical scalability of epitaxy-guided Zn plating, the areal capacity was increased to 20 mAh/cm². Remarkably, deposition on Cu(111) remained dendrite-free and maintained a uniform morphology, forming a compact Zn layer of ~25 µm thickness, as illustrated in Figure II.1.8. In comparison, the same capacity deposited on polycrystalline commercial Cu couldn't achieve the same compaction until 100th micron, resulting in a very porous & moss-like Zn layer (~105 µm), emphasizing the inefficient packing and porous growth arising from uncontrolled nucleation and dendritic propagation. Cross-sectional SEM imaging further confirms that plating on Cu(111) is dense and conformal, whereas poly-Cu supports a more porous and anisotropic growth front. The synthesis of large-area, high-quality Cu(111) foil enabled the exploration of millimeter-scale deposition uniformity.

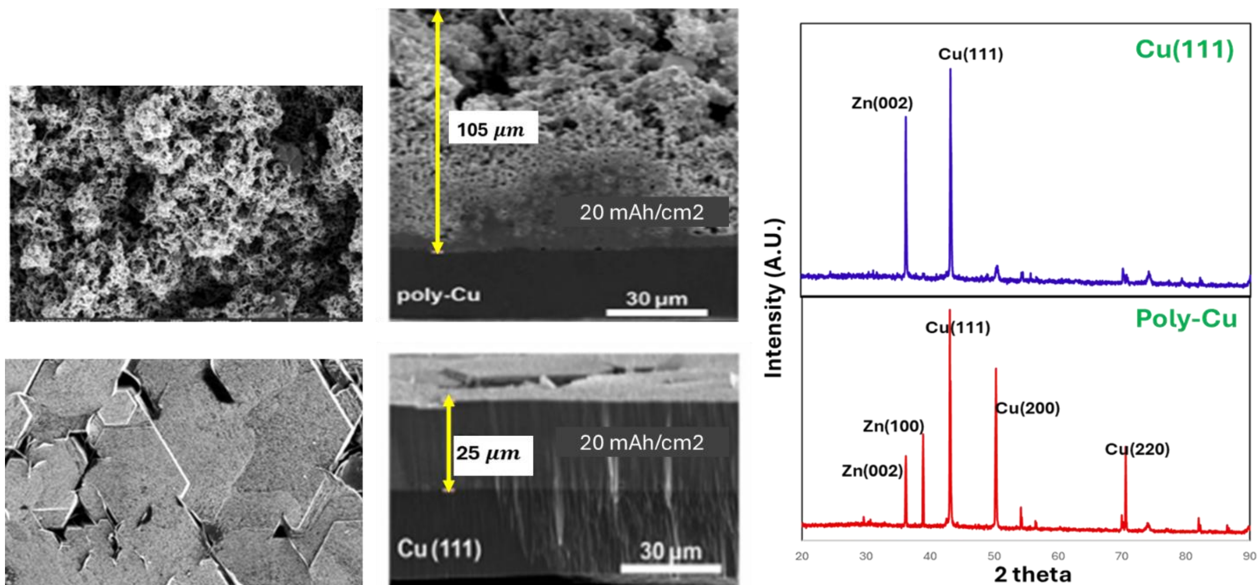

Figure II.1.8: (A) Top-view SEM images of Zn on poly-Cu and Cu(111) after deposited with 20mAh/cm² Zn. (current density = 10 mA/cm²); & Cross-sectional SEM image of high-capacity zinc loading (20 mAh/cm²) onto poly-Cu & Cu(111); (B) XRD spectra of Cu(111) & Polycrystalline Cu foil

II.2. Evolution of Zn (002) Texture with Zinc Electrodeposition Capacity

The ability of a crystalline substrate to guide the textured growth of an electrodeposited material would be expected to diminish progressively with increasing film thickness, as the registry between the deposited material and the underlying lattice becomes increasingly disrupted. This phenomenon is especially pertinent in metal-on-metal systems, where the strength of epitaxial correlation is dictated by interfacial bonding, electrochemical kinetics, lattice mismatch, interfacial strain accumulation, and mass transport limitations. For systems such as Zn grown on textured Cu(111), these effects result in a gradual decay of preferred (002) texture orientation as the deposition proceeds.

Figure II.2.1 presents the Zn(002) texture ratio variation results from XRD analysis of Zn films electrodeposited on Cu(111) substrates with varying initial texture ratios, ranging from 40% to 96%. The electrodeposition was carried out under galvanostatic conditions (5 mA/cm²) in symmetrical Cu | 2 M $ZnSO_4$ (aq) | Cu cells for a range of deposition capacities (5–50 mAh/cm²). Across all cases, Zn was observed to preferentially adopt the (002) orientation initially, especially when deposited on highly textured Cu(111) substrates. However, the (002) texture ratio (TR) of the Zn deposits exhibited a systematic decay with increasing deposited capacity. For each

substrate, the evolution of texture ratio with areal capacity (D) was observed to follow an exponential decay model:

$$T_R(D) = A \cdot e^{-D/\Lambda}$$

where A is the extrapolated texture ratio at D = 0, and Λ is a characteristic decay constant representing the capacity over which the (002) texture reduces by a factor of 1/e.

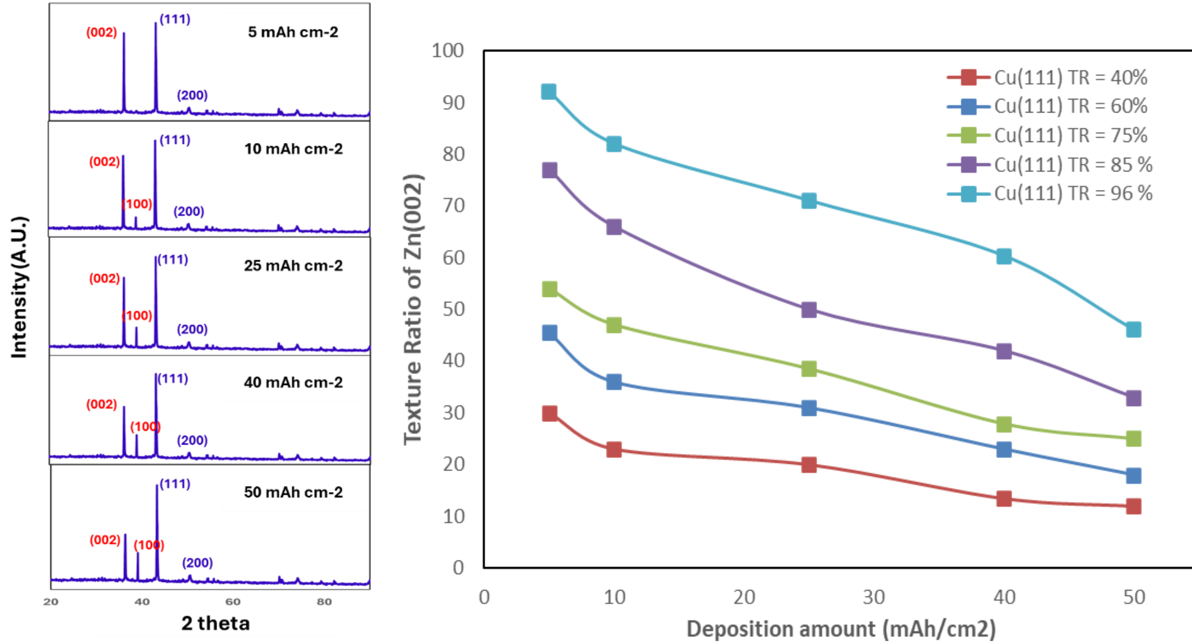

Figure II.2.1: Texture Ratio of Zn (002) vs Zn deposition amount or areal capacity (mAh/cm²)

Straight-line fits to the semi-log plots of Ln[TR Zn(002)] vs D (Figure II.2.2) confirm the appropriateness of this model across the entire set of substrates. The fitted decay constants Λ span a broad range, from 51.5 mAh/cm² for moderately textured Cu (40%) to over 68 mAh/cm² for the most highly textured Cu (96%). The decay constants Λ reflect the texture correlation length, which when multiplied by an estimated layer thickness of ~1.8 µm per mAh/cm² (assuming bulk Zn density). The decay of Zn(002) texture ratio with increasing areal capacity on Cu(111) substrates follows an exponential trend, allowing the extraction of characteristic decay constants (Λ) for each initial Cu texture condition. These Λ values were used to estimate correlation lengths, representing the effective thickness of Zn over which epitaxial growth persists. The results reveal that correlation lengths range from ~93 µm to over 129 µm, with the highest value corresponding to the most highly textured Cu(111) substrate (96% TR).

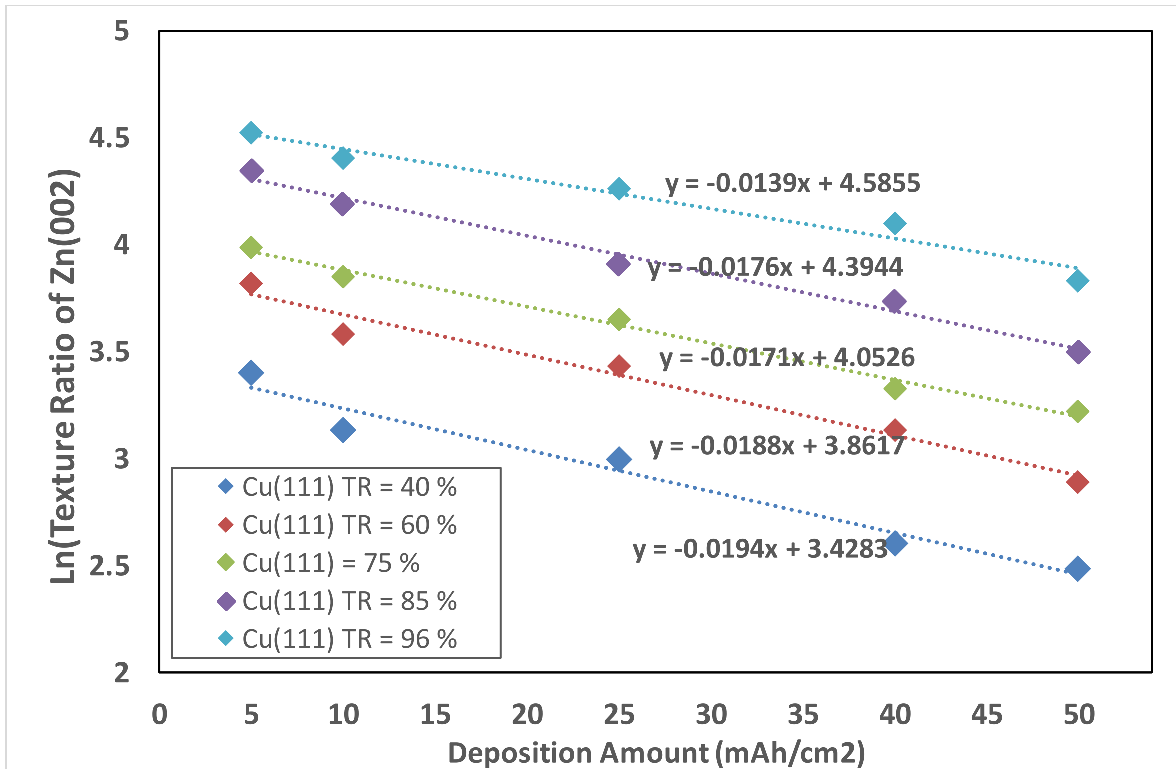

Figure II.2.2: Semi-log of the Zn (002) Texture ratio vs Zn deposition amount (mAh/cm²)

This suggests that stronger initial substrate texture enables significantly longer-range epitaxial control over Zn crystallographic orientation during electrodeposition, providing a practical strategy for controlling anode morphology in aqueous Zn batteries. These are substantial and confirm that significant crystalline registry is retained over practical electrode thicknesses used in rechargeable battery systems. For typical Zn anode loadings in the range of 1–10 mAh/cm², the epitaxial influence of a well-textured Cu(111) substrate can be expected to dominate the deposited Zn microstructure.

Moreover, it has been observed that for all substrates except the most highly textured (96%), the Zn(002) texture ratio converges toward a limiting value in 20–35% at high deposition capacities. This asymptotic behavior is indicative of the accumulation of randomly oriented Zn grains or pulverized Zn, especially prevalent when the epitaxial registry is overwhelmed by electrocrystallization noise, mass transport gradients, or interfacial strain. Taken together, these findings underscore the critical role of substrate crystallography in directing Zn texture evolution and suggest that engineering Cu substrates with high (111) texture can serve as a practical strategy

to promote long-range epitaxial growth of Zn(002) — thereby potentially improving cycling stability, shape retention, and suppressing dendritic formation in aqueous Zn-ion batteries.

II.3. Investigating Surface-Controlled Zn Growth via Underpotential Deposition on Copper

Underpotential deposition represents an intriguing electrochemical process where metallic species undergo reduction at electrode interfaces when subjected to potentials less negative than their standard reduction values [20, 54, 55]. This phenomenon enables metals to electrodeposit onto certain foreign substrates with greater ease compared to deposition onto their own surfaces or inert substrates like glassy carbon or platinum, resulting in enhanced thermodynamic stability and accelerated reaction kinetics. Exploiting zinc's UPD characteristics and achieving homogeneous electrodeposition presents a viable approach for improving zinc electrode performance. This investigation examines underpotential deposition mechanisms to mitigate zinc non-planar deposition challenges & also identify favorable conditions for Zn-Cu alloying in electrolytes that do not contain additives. To characterize zinc's underpotential deposition characteristics on copper surfaces, comparative studies were conducted using zinc metal and glassy carbon materials. Cyclic voltammetry (CV) experiments demonstrated that the initial nucleation potential of zinc on copper was more positive compared to zinc substrate, as shown in Figure II.3.1.

This observation confirms the UPD phenomenon, which enables abundant nucleation with lower energy requirements and consequently guides uniform zinc deposition [55, 56]. The preferential deposition becomes more pronounced with increasing scanning speeds (from 0.005 to 5 V/s). At higher scan rates, the timescale of the potential sweep becomes too short for slower diffusion-limited or bulk nucleation processes to occur, favoring instead the rapid, surface-specific adsorption characteristic of underpotential deposition. This kinetic constraint enhances the selectivity for Zn nucleation at high-affinity Cu sites, such as terraces or low-index planes, where Zn–Cu interactions are strongest. As a result, the UPD process becomes more pronounced with increasing scan rate, while competing overpotential deposition pathways are effectively suppressed.

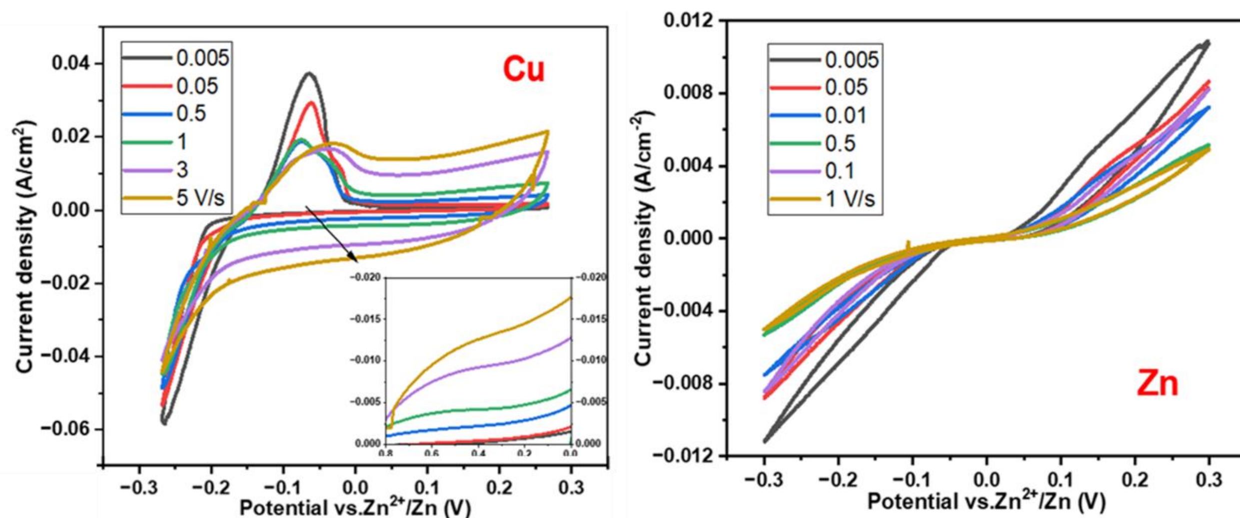

Figure II.3.1: Voltammograms of Zn metal plating/stripping on 2 different substrates (Scan rate from 0.005V/s to 5V/s): (A) Cu foil, (B) Zn foil

Chronoamperometry (CA) studies further validated the two-dimensional rapid nucleation and growth process characteristic of Zinc UPD as shown in Figure II.3.2 (A) [57, 58]. On zinc substrates, current stabilization was significantly delayed—taking up to 300 seconds at an overpotential of –150 mV—due to a prolonged two-dimensional surface diffusion phase during which Zn^{2+} ions accumulated at protrusions, favoring dendritic growth. In contrast, on Cu (111) substrates, this initial surface diffusion phase was markedly brief, reaching steady-state behavior within 20 seconds, after which uniform three-dimensional deposition dominated. This rapid transition suggests that Zn^{2+} ions adsorbed on the Cu (111) surface undergo near-immediate local reduction with minimal lateral migration [58]. The underlying cause is the strong electronic interaction between Zn^{2+} species and the Cu (111) facet, which compels the ions to deposit directly at their initial adsorption sites rather than migrating toward lower-energy nucleation sites. As a result, the deposition proceeds in a compact, planar fashion, promoting smooth and uniform Zn layer formation.

Furthermore, Xray Photoelectron Spectroscopy (XPS) analysis confirmed that the deposits on both zinc and copper substrates were metallic zinc (Zn^0) rather than adsorbed ions (Figure II.3.2 (B)). Notably, the binding energy of $Zn2p_{3/2}$ electrons in UPD deposits on copper substrate increased by 0.28 eV compared to those on zinc substrate, indicating stronger interactions. Scanning Electron Microscopy (SEM) observations and Energy Dispersive X-ray

Spectroscopy (EDS) mapping demonstrated numerous zinc nuclei on the copper substrate, corroborating the CA test results.

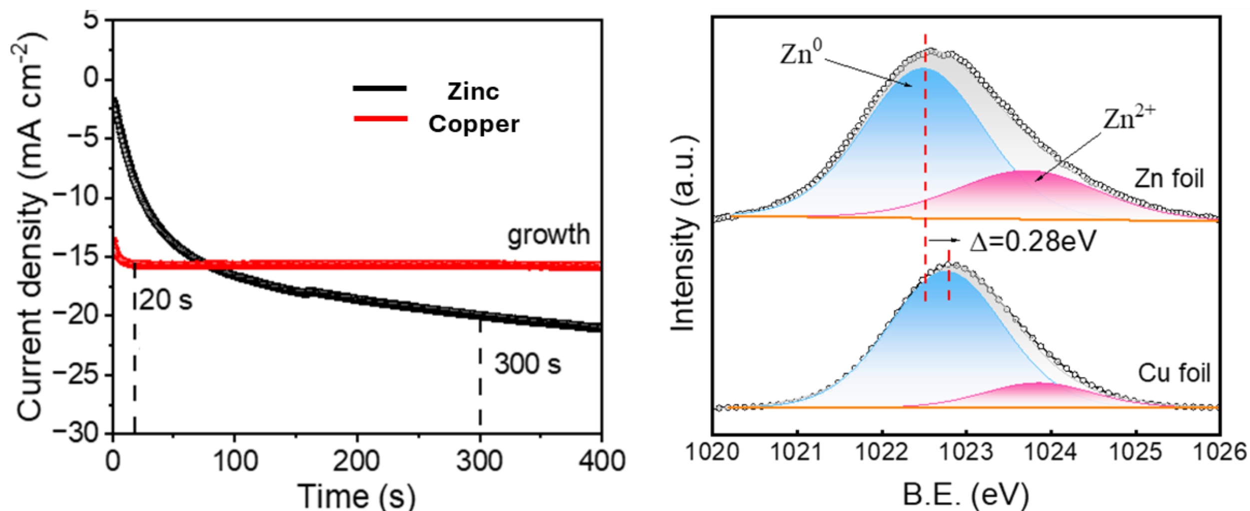

Figure II.3.2: (A) Chronoamperograms of Zn on Zn & Cu at an overpotential of -150mV; (B) High-resolution Zn $2p^{3/2}$ XPS spectrum after Zinc metal deposition.

The zinc affinity characteristics of Cu(111) deposits obtained in lower I-V regimes from the 2 M zinc sulfate electrolyte were examined using cyclic voltammetric analysis. Electrochemical measurements revealed that the initial zinc reduction on copper (111) surfaces commenced at approximately 0.57 V relative to Zn^{2+}/Zn reference, exceeding the standard Nernst potential for zinc reduction, which indicates underpotential deposition occurrence on copper (111) interfaces. A subsequent reduction process appeared at -0.45 V versus Zn^{2+}/Zn, below the equilibrium potential, signifying bulk zinc deposition. Notably, bulk zinc deposition initiated earlier on copper (111) compared to standard copper foil, demonstrating superior zinc affinity of (111)-oriented copper relative to polycrystalline copper surfaces. This distinction became evident through galvanostatic discharge profiles (Figure II.3.3), where standard copper exhibited pronounced voltage drops at deposition onset followed by stable plateaus, while copper (111) surfaces showed minimal voltage perturbations. The measured nucleation overpotential difference between initial and plateau voltages reached 42 mV for copper (111), substantially lower than the 75 mV observed for commercial copper foil, indicating reduced nucleation barriers on (111)-oriented surfaces.

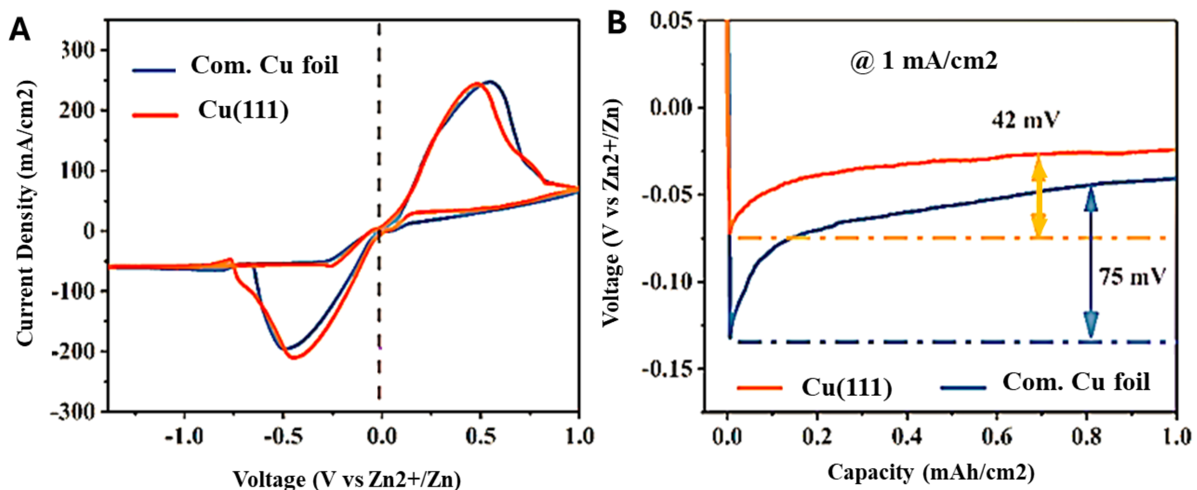

Figure II.3.3. Zincophilicity of different Cu foils. (a) Cyclic voltammograms of Cu(111) and routine Cu electrodes in 2 M $ZnSO_4$. (b) Voltage profiles recorded during Zn plating at 1 mA/cm^2.

II.4. Evaluating Zn Plating/Stripping & Cycling Performance on Cu (111) Substrate

To understand the influence of substrate crystallography and interfacial reactivity on Zn electrodeposition behavior, a systematic investigation of Zn plating/stripping reversibility on textured Cu substrates, especially Cu(111), compared to conventional stainless steel (SS) and polycrystalline Cu foil, was conducted. The results reveal a dependence of electrochemical performance on substrate interaction strength and crystallographic alignment. The voltage profiles of Zn plating/stripping at a high areal capacity (5 mAh/cm^2) highlight the stark contrast between interacting and non-interacting substrates (Figure II.4.1). While stainless steel exhibited severe voltage polarization and cycle instability, Cu substrates demonstrated superior reversibility. More significantly, Cu(111) substrates enabled remarkably stable cycling with low hysteresis and negligible degradation over extended periods. These behaviors are attributed to the interfacial alloying process and lattice matching effects that guide Zn deposition morphology.

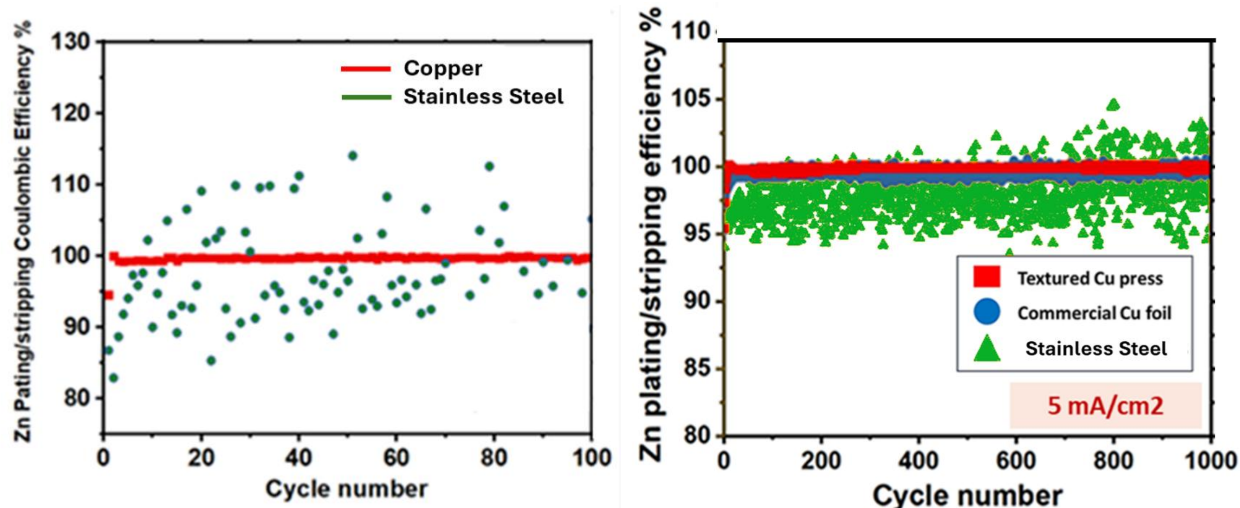

Figure II.4.1: Zn plating/stripping measurements at 5 mAh/cm². Cu and Stainless Steel are chosen as representatives of interacting and non-interacting substrates, respectively, for evaluation at this high areal capacity.

As shown in Figure II.4.2, the plating/stripping behavior of Zn on Cu substrates exhibits remarkable consistency across a wide range of current densities, affirming the substrate's capacity to support highly reversible metal deposition. At a low current density of 2 mA/cm², the deposition proceeds under near-equilibrium conditions, which permits sufficient time for surface diffusion and interfacial alloying phenomena to manifest more clearly in the potential profiles. Under these conditions, subtle signs of Zn–Cu intermetallic interaction may appear, including a "kink" in the stripping branch — a signature of dealloying dynamics associated with underpotential deposition (UPD) and re-extraction of Zn from alloyed sites. This behavior, while subtle, indicates a surface-mediated alloy formation process that does not significantly compromise overall reversibility. As the current density increases to 40 mA/cm², the system enters a kinetically driven regime where deposition and stripping occur more rapidly, and the time window for interfacial rearrangement becomes limited. Notably, under such high-rate conditions, any traits of alloying or UPD-induced dealloying become less pronounced in the potential profiles. This reduction in interfacial complexity coincides with an improvement in Coulombic efficiency (CE), reflecting a more straightforward and diffusion-limited electrochemical reaction pathway that avoids energy losses associated with complex intermediate states.

What is particularly significant is that across both the low and high current density regimes, Cu substrates consistently support stable Zn plating/stripping, without signs of

morphological instability or excessive hysteresis. This highlights the chemically favorable yet moderately interactive nature of the Zn–Cu interface, which neither leads to inert behavior (as seen in weakly interacting substrates like stainless steel) nor irreversible alloying. Instead, it creates an ideal interfacial landscape wherein Zn can nucleate uniformly, undergo reversible partial alloying at underpotential conditions, and be stripped cleanly, preserving the surface for repeated cycling. This behavior underscores a broader mechanistic insight: a moderately strong interfacial interaction, such as that between Zn and Cu, is critical to achieving high-efficiency and long-life electrodeposition systems. The interface must be chemically active enough to direct uniform nucleation and promote a self-sustaining underpotential cycle, yet not so reactive that it results in irreversible surface modifications or loss of reversibility. The consistently high CE and stable potential profiles observed on Cu over a range of current densities affirm their unique suitability as a substrate for reversible Zn anodes in rechargeable battery systems.

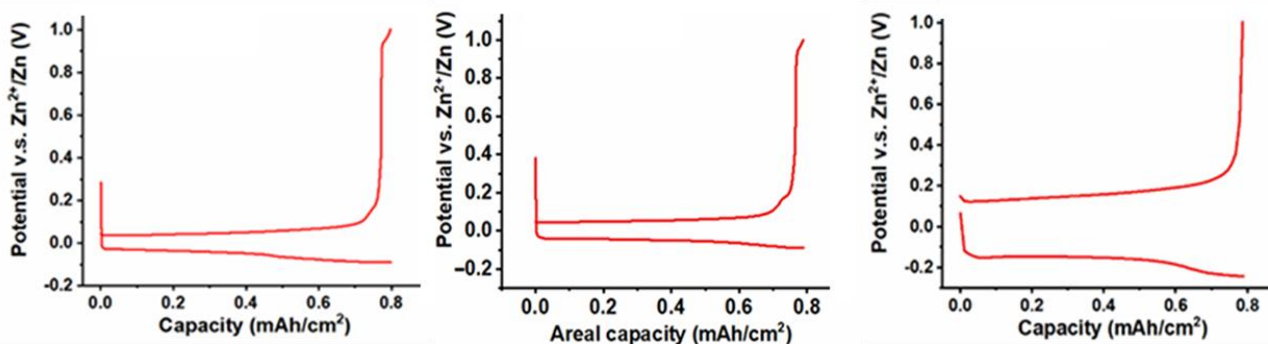

Figure II.4.2: Galvanostatic electrochemical plating/stripping behaviors of Zn on Cu(111) at different current densities (a) 2 mA/cm^2; (b) 10 mA//cm^2 and (c) 40 mA/cm^2

To eliminate any contribution from copper dissolution and confirm interfacial behavior, the upper cutoff voltage was limited to 0.5 V vs. Zn^{2+}/Zn — well below the Cu^{2+}/Cu standard potential of ~1.0 V vs. Zn^{2+}/Zn. Even under this restriction, the voltage profiles retained the distinct "kink" during stripping, characteristic of dealloying phenomena, and the Coulombic efficiency (CE) remained high (Figure II.4.3). This suggests that the observed behavior stems from alloy-mediated UPD mechanisms rather than bulk Cu oxidation. To rule out any possible influence from Cu oxidation/dissolution, Zn plating/stripping was performed on Cu(111) using an upper cutoff voltage of 0.5 V vs. Zn^{2+}/Zn, which is ~0.6 V below φ^o (Cu^{2+}/Cu) and should avoid Cu dissolution. Evidently, the high Zn plating/stripping reversibility and the shape of the voltage profile observed under this condition were in line with the results obtained with a +1.0 V cutoff voltage.

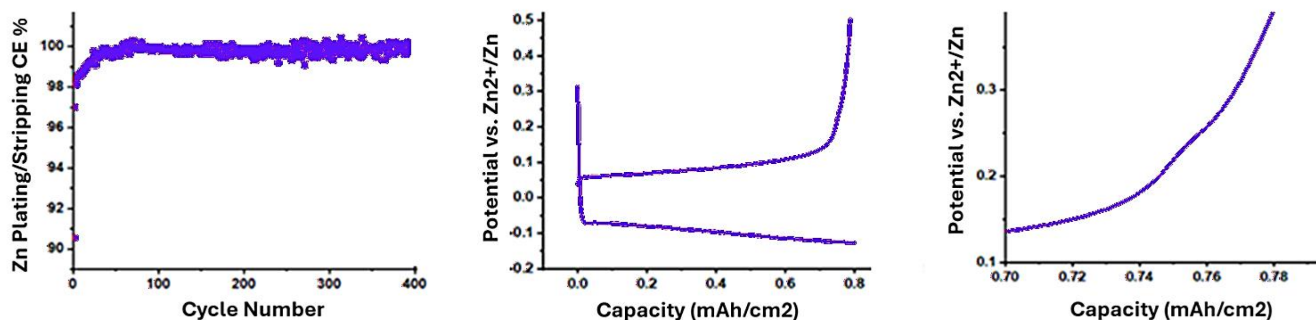

Figure II.4.3: Zn plating/stripping measurement on Cu(111) with an upper cutoff voltage of 0.5 V vs Zn^{2+}/Zn.

Due to the uncontrolled growth of Zn dendrites during repeated cycling, cells utilizing commercial polycrystalline Cu as the substrate experienced an abrupt failure after only 260 cycles, caused by an internal short circuit. In stark contrast, when the substrate was switched to single-crystal-like Cu(111), the system exhibited remarkably stable and efficient cycling, maintaining a Coulombic Efficiency (CE) exceeding 99% over 2000 cycles (Figure II.4.4 (A)). This dramatic improvement reflects the ability of Cu(111) to guide uniform Zn deposition and suppress dendritic growth effectively. Moreover, the voltage hysteresis—a key indicator of interfacial reaction kinetics and polarization losses—was significantly reduced for the Cu(111)-based cells, measuring only 0.147 V, which is notably lower than that observed in cells employing commercial Cu (Figure II.4.4 (B)). This reduced hysteresis indicates enhanced charge transfer kinetics and lower energy loss during each plating/stripping cycle on the Cu(111) surface. The superior performance of Cu(111) can be attributed to the epitaxial relationship between the Cu(111) surface and the basal Zn(002) plane. This lattice-matching promotes an ordered, planar deposition pattern, which not only enhances the uniformity of Zn nucleation and growth but also mitigates the formation of high-surface-area structures like dendrites.

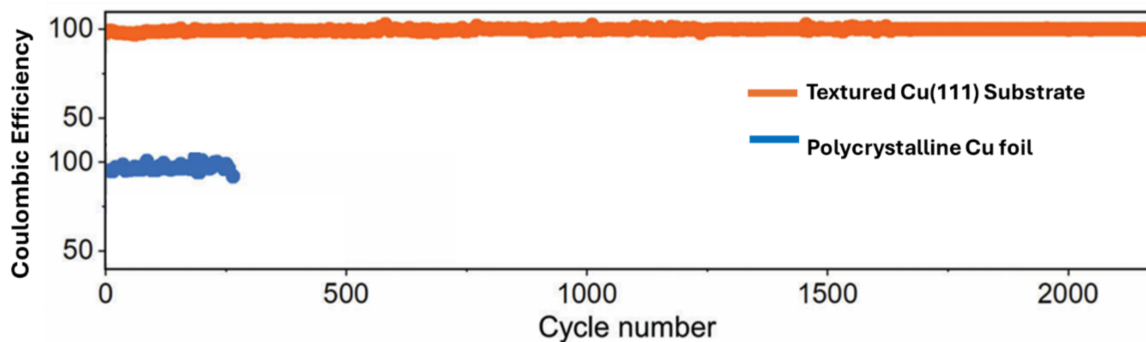

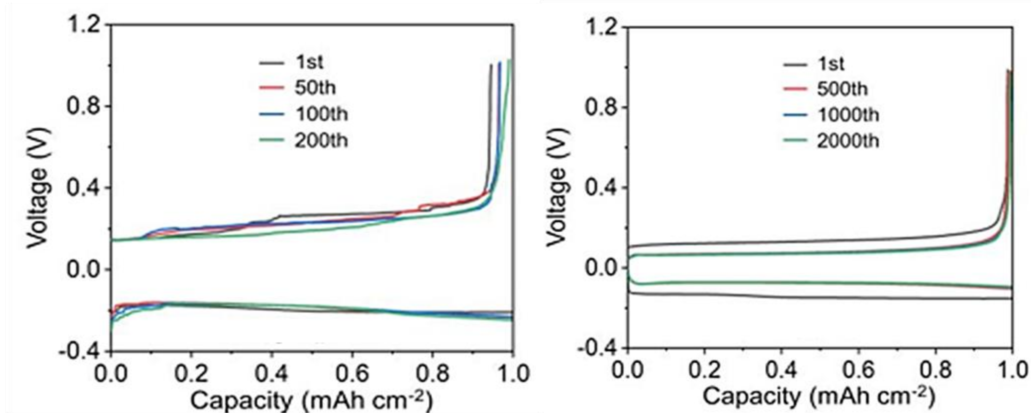

Figure II.4.4: Charge/discharge curves of cells at selected cycles.

To establish practical relevance, high rate cycling at 40 mA/cm² was performed. Zn deposition on Cu (111) substrates maintained a CE of 99.9% over 10,000 cycles (Figure II.4.5), surpassing most literature benchmarks. These findings emphasize that a close-to-unity CE is achievable when the substrate promotes a self-sustaining underpotential cycle — a dynamic wherein Zn continuously deposits at UPD sites regenerated by ongoing Cu–Zn alloying and dealloying. This mechanistic insight — a self-sustaining underpotential deposition loop — captures the essence of how interfacial alloy formation at a moderately interactive substrate such as Cu(111) enhances deposition reversibility. This mechanism not only initiates Zn UPD at favorable nucleation sites but also perpetuates their regeneration through surface alloying, thus bridging the initial nucleation step with bulk plating in a continuous cycle.

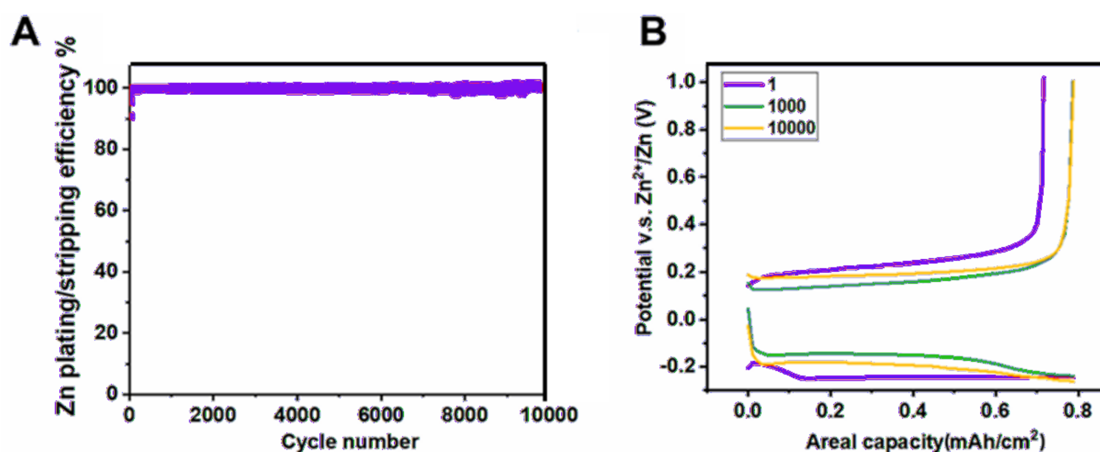

Figure II.4.5: Plating/stripping of Zn on Cu at 40 mA/cm². (A) CE values and (B) representative plating/stripping voltage profiles. The cell shows an extremely stable plating/stripping behavior over prolonged cycling, with an average CE of 99.9%.

SECTION III: Interfacial Control in Binary Metal Electrodeposition in Aqueous Medium

This section explores how substrate crystallography, electrolyte composition, and interfacial electrochemistry collectively govern metal electrodeposition, focusing on both pure copper and binary Zn–Cu systems. A central question addressed is whether the crystallographic stabilization observed for zinc on Cu(111) surfaces—particularly the promotion of planar, compact growth—is a consequence of zinc's hexagonal structure or a more general phenomenon applicable to other face-centered cubic (FCC) metals such as copper itself. The investigation begins with an in-depth study of copper electrodeposition from aqueous $CuSO_4$ solutions under varying concentrations and current densities. Despite copper's FCC structure, its deposition behavior exhibits notable similarities to that of zinc, including the preferential emergence of the (111) texture at low overpotentials and clear morphological transitions as mass transport becomes limiting. Enhanced ion transport through electrolyte agitation is shown to restore thermodynamically favorable orientations even under high-current conditions, underscoring the dynamic interplay between transport and crystallographic control.

Building upon this, the analysis of binary Zn–Cu electrodeposition reveals how underpotential deposition (UPD) of Zn onto Cu surfaces plays a critical role in alloy formation and morphology control, even in systems characterized by substantial redox potential mismatch. At low overpotentials, Zn forms Cu-rich α-brass solid solutions via UPD, whereas more negative potentials lead to the formation of three-dimensional Cu–Zn clusters. These clusters act as catalytic platforms that lower nucleation barriers and enhance exchange current densities, promoting dense, uniform Zn films devoid of dendritic features. Structural and compositional analyses using XRD and EDS indicate a progression from solid solution to Zn-rich intermetallic phases with increasing potential and Zn content. Overall, the findings highlight that interface engineering—through substrate crystallography and mechanistic exploitation of UPD—offers a powerful strategy for achieving uniform, compositionally controlled deposition of binary alloys with widely separated redox potentials. Building on this understanding of alloy formation driven by redox asymmetry and interface-stabilized nucleation, the Ni–Co system provides a natural progression in alloy electrodeposition studies to gain further mechanistic insights on binary alloy electrodeposition in aqueous media. In contrast to Zn–Cu, nickel and cobalt possess closely matched standard redox potentials (–0.25 V for Ni^{2+}/Ni and –0.277 V for Co^{2+}/Co), minimizing electrochemical asymmetry

and enabling co-deposition under near-equilibrium conditions. The atomic radii of Ni and Co differ by less than 1% (Ni: 124.6 pm; Co: 125 pm), and both elements exhibit high mutual solubility, forming a continuous solid solution across the full composition range. Though Ni is FCC and Co is HCP at room temperature (analogous to FCC Cu & HCP Zn in Cu-Zn binary system at room temperature), the Co can attain FCC crystallinity at temperatures above 417°C, making structural integration more feasible [59]. The enthalpy of mixing for Ni–Co is mildly negative, approximately –1 to –2 kJ/mol, and the electronegativity difference is negligible (Ni: 1.91, Co: 1.88), supporting alloy stability without requiring UPD [60]. Despite this, anomalous codeposition is frequently observed, where the less noble Co deposits preferentially even when Ni is present in higher concentration, due to surface adsorption effects and intermediate species such as MOH^+ that alter local deposition kinetics.

III.1. Crystallographic Analysis of Electrodeposited Copper in Different I-V Regimes

To explore whether the interfacial stabilization phenomena observed during Zn electrodeposition are material-specific or generalizable across metallic systems, a comparative investigation was conducted on Cu electrodeposition from aqueous $CuSO_4$ electrolytes of varying concentrations. Copper, with its face-centered cubic (FCC) lattice, differs from Zn's hexagonal close-packed (HCP) structure, making it an ideal candidate to evaluate whether crystallographic texturing and morphological control are influenced solely by electrolyte composition and transport dynamics, rather than crystal symmetry. Moreover, like Zn, Cu does not form a passivating solid-electrolyte interphase (SEI), ensuring that the subsequent observations are unaffected by interfacial barrier layers.

Morphological evaluations of Cu deposits grown in 1 M $CuSO_4$ (concentrated) and 0.05 M $CuSO_4$ (dilute) electrolytes reveal a distinct transformation in growth characteristics with concentration. Under overlimiting conditions, deposits from the concentrated electrolyte exhibit uniform, porous, yet planar morphologies. In contrast, dendritic and heterogeneously distributed Cu deposits dominate in the dilute electrolyte (Figure III.1.1 & Figure III.1.2). These results parallel those seen in Zn systems and confirm that the suppression of dendrites in concentrated media is not unique to hexagonal metals like Zn. Instead, they suggest that ionic concentration, and its effect on ion transport and local electric fields, governs the morphological regime.

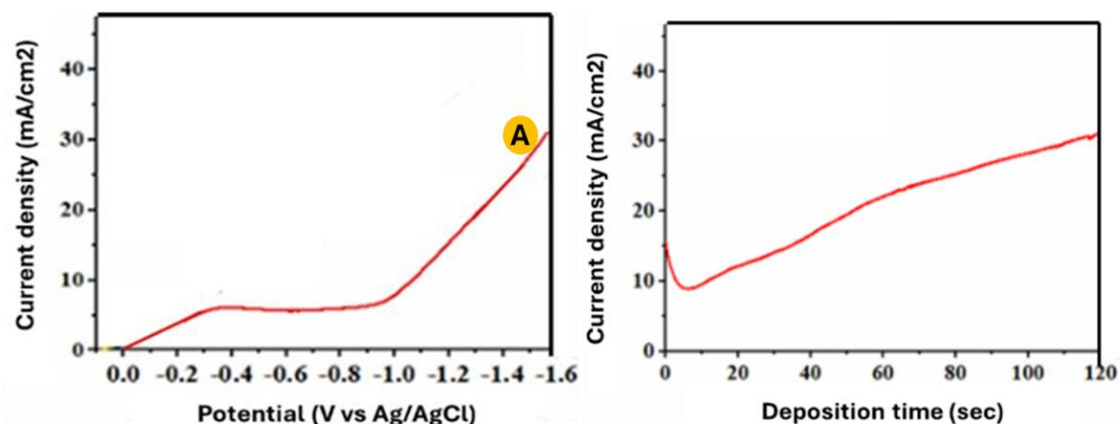

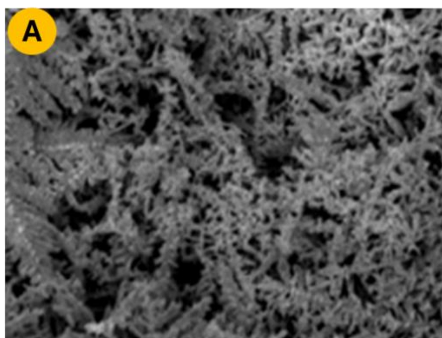

Figure III.1.1: Electrochemical characteristics of Cu deposition on a glassy carbon electrode from 0.05 M $CuSO_4$ (aq) electrolyte. (Left) Current-voltage (I-V) curves measured during Cu electrodeposition without rotation. (Right) Time-dependent current measured in constant-voltage.

The electrodeposition morphology at different overpotentials in the 1 M $CuSO_4$ system was assessed using SEM at -0.5 V, -1.0 V, and -1.5 V vs Ag/AgCl (Figure III.1.2). At progressively more negative potentials, the porosity of Cu deposits increased significantly, although notably, dendritic growth remained suppressed. When a hydrodynamic flow (1000 rpm rotation) was applied at -1.5 V, the porosity was drastically reduced, illustrating the critical role of convection in controlling growth morphology under high driving forces.

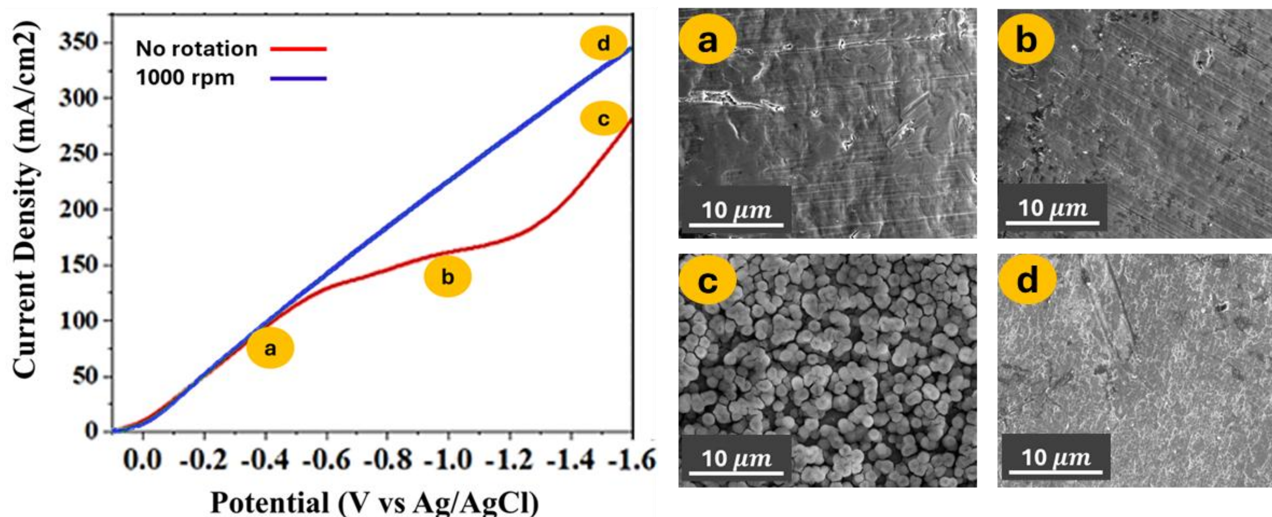

Figure III.1.2: Electrochemical characteristics of Cu deposition on a glassy carbon electrode from 1 M $CuSO_4$ (aq) electrolyte. (A) Current-voltage (I-V) curves measured during Cu electrodeposition with and without rotation; (B) SEM images showing morphological evolution of Cu electrodeposits in 1 M $CuSO_4$ (aq) electrolyte at different potentials.

A deeper understanding of crystallographic evolution in these deposits was obtained through galvanostatic Cu electrodeposition by systematically varying current density, in a 1 M $CuSO_4$ solution. X-ray diffraction (XRD) analyses at 0.1 A/cm² ($< i_L$), 0.18 A/cm² ($\approx i_L$), and 0.27 A/cm² ($> i_L$) revealed significant texture transitions (Figure III.1.3 (A)). At low current density (0.1 A/cm²), where diffusion rate dominates ($\nu_1 > \nu_2$, ν_1 is the rate of ionic diffusion from the bulk to the electrode surface and ν_2 is the rate of cation reduction on the electrode), Cu deposits developed a strong (111) orientation, which is consistent with the system's tendency to minimize surface energy under low-overpotential conditions. As current density approached and surpassed the limiting current (iL ≈ 0.18 A/cm²), a transition to mixed (111)/(110) and eventually dominant (110) textures was observed. This trend corresponds to the development of ion depletion zones, where $\nu_1 < \nu_2$, and electrodeposition becomes mass-transport limited.

This texture evolution is further supported by SEM imaging, which revealed that Cu deposited at low current densities formed large, flat grains indicative of thermodynamically favored growth. In contrast, high current densities led to finer, more branched structures. Current density was found to directly impact nucleation dynamics and crystallite size, consistent with classical electro crystallization theory and the Butler–Volmer framework. At lower current

densities and overpotentials, nucleation proceeds more slowly, allowing the formation of larger critical nuclei and, consequently, larger grain dimensions. These structural features were confirmed through SEM (Figure III.1.3 (B)), where the low-current-density Cu deposits showed coarser grains with fewer tip-effect-induced islands, while higher-current deposits exhibited smaller, less uniform grains with pronounced tip-growth effects. Furthermore, the influence of mass transport was further examined by introducing electrolyte stirring (Figure III.1.3 (C)). With enhanced convection, Cu foils deposited at higher current densities (0.25 – 0.3 A/cm²) displayed improved (111) orientation with diminished (200) peaks; however, slight increase in the intensity of (110) peak was also observed. This demonstrates that increasing the rate of ion delivery (ν_1) can counterbalance the effects of elevated consumption (ν_2), thereby promoting surface-energy-minimized growth even under higher deposition rates.

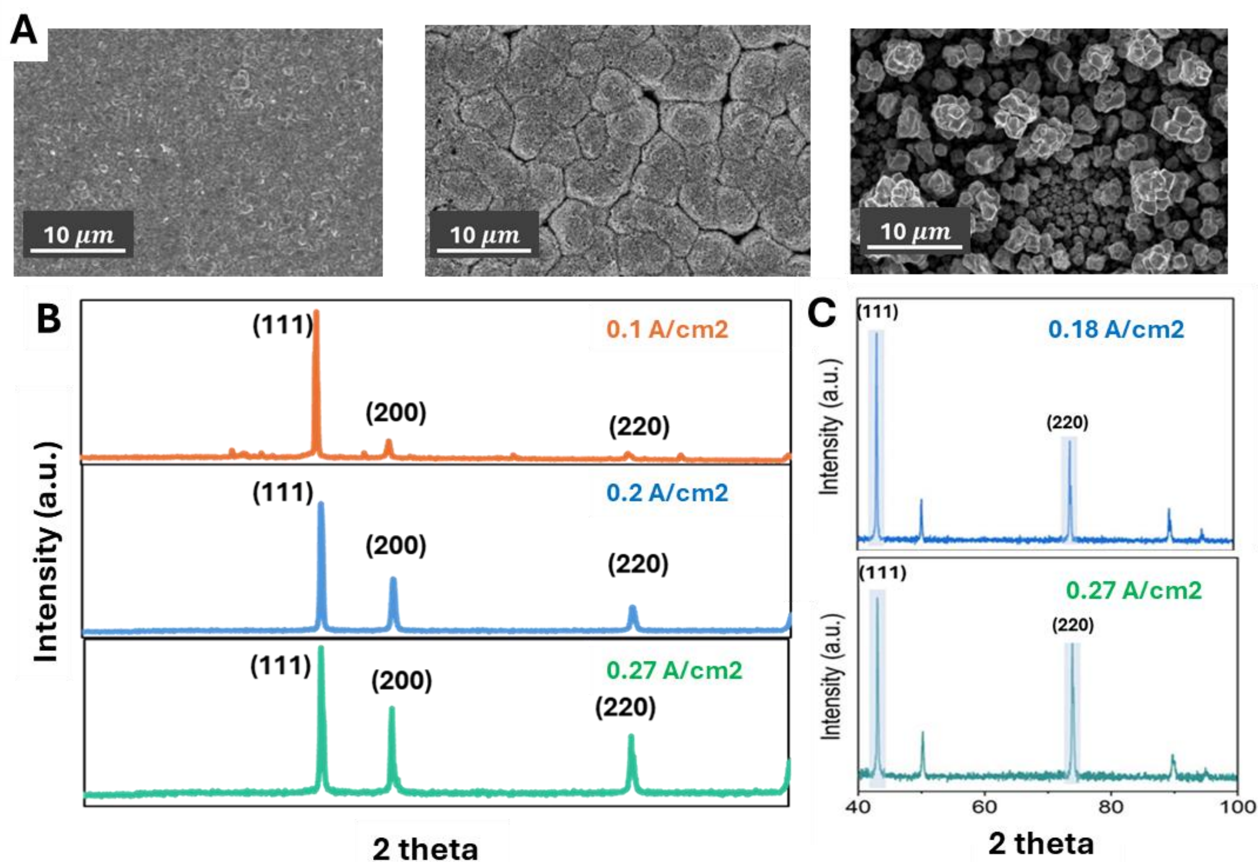

Figure III.1.3: (A) SEM images of Cu deposits obtained at different current densities – 0.1, 0.18 & 0.27 A/cm²; (B) XRD patterns of Cu deposits obtained at different current densities. (C) XRD patterns of Cu foils obtained at high current densities in stirring electrolytes.

Together, these findings offer an electrochemical-crystallographic framework for Cu deposition. They reinforce the concept that deposition morphology and texturing are governed not only by intrinsic material properties but also by the interplay between mass transport, interfacial reaction kinetics, and applied electrochemical parameters. These insights directly inform the strategic engineering of textured Cu substrates—especially Cu(111)—for applications such as Zn anodes, where crystallographic templating plays a pivotal role in achieving uniform, stable, and dendrite-free metal growth.

III.2. Harnessing UPD for Sustained Electrodeposition of Zn-Cu Alloy & Planar Zn Growth

The electrodeposition of zinc-copper alloys presents a fundamental challenge rooted in the substantial difference between their standard reduction potentials ($\Delta E° = 1.1$ V). This thermodynamic bias creates an inherent tendency for preferential copper deposition, making uniform binary alloy formation extremely difficult through conventional electrochemical approaches. However, the phenomenon of underpotential deposition (UPD) offers a promising pathway to overcome these limitations by enabling zinc atom deposition & nucleation on copper surface at potentials significantly more positive (or less negative) than its bulk reduction potential on zinc or inert substrate. Building upon our previous observations of epitaxial zinc growth on highly textured copper substrate, we now explore how concentration & substrate-controlled interface effects can enable uniform Cu-Zn alloy formation & high-quality Zn coatings without using any additives in aqueous electrolyte. This investigation reveals how UPD mechanisms can be systematically exploited to achieve controlled co-deposition of metals with widely separated reduction potentials, representing a transition from surface-confined alloying to bulk type alloying.

The investigation began with a systematic exploration of how electrolyte concentration, with equimolar $ZnSO_4$ and $CuSO_4$, affects the fundamental deposition mechanism. Linear sweep voltammetry of binary zinc-copper solutions at three concentration levels (0.05 M, 0.1 M, and 0.5 M) revealed a striking transformation in electrochemical behavior. At low concentrations (0.05 M), the binary Zn–Cu system demonstrates distinct underpotential co-deposition behavior that evolves through multiple mechanistic regimes. The LSV results (Figure III.2.1) reveal that copper is the first species to undergo reduction and deposit at the onset of the current response. This

nucleation step promotes the subsequent growth of Cu-rich atomic layers. Although zinc begins to undergo underpotential deposition (UPD) immediately following the formation of the first few Cu monolayer, its distinct electrochemical signature becomes visibly apparent starting at approximately –0.2 V. The strong Zn–Cu binding interactions stabilize this UPD layer at potentials more positive than the standard Zn^{2+}/Zn redox potential, consistent with classical UPD theory. This asymmetric UPD behavior is unidirectional; while Zn readily deposits underpotentially on Cu, the reverse is not observed. Cu does not exhibit UPD behavior on a Zn substrate. Instead, due to the large redox potential gap (Cu^{2+}/Cu = +0.34 V vs SHE; Zn^{2+}/Zn = –0.76 V vs SHE), Cu^{2+} can be spontaneously reduced on metallic Zn surfaces via displacement reaction, even in the absence of an applied potential. This galvanic displacement pathway becomes particularly relevant once Zn atoms are incorporated into the deposit, thereby providing localized cementation sites for Cu, in addition to the electrochemically controlled Cu^{2+} reduction pathway.

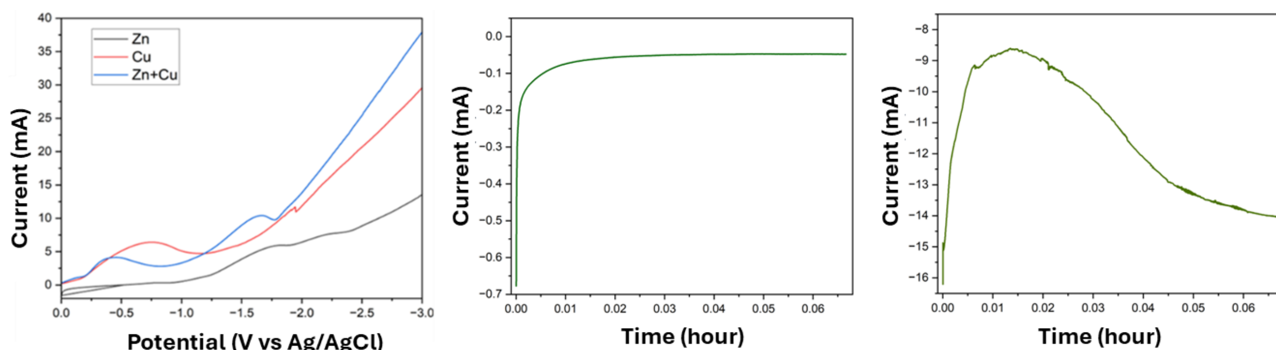

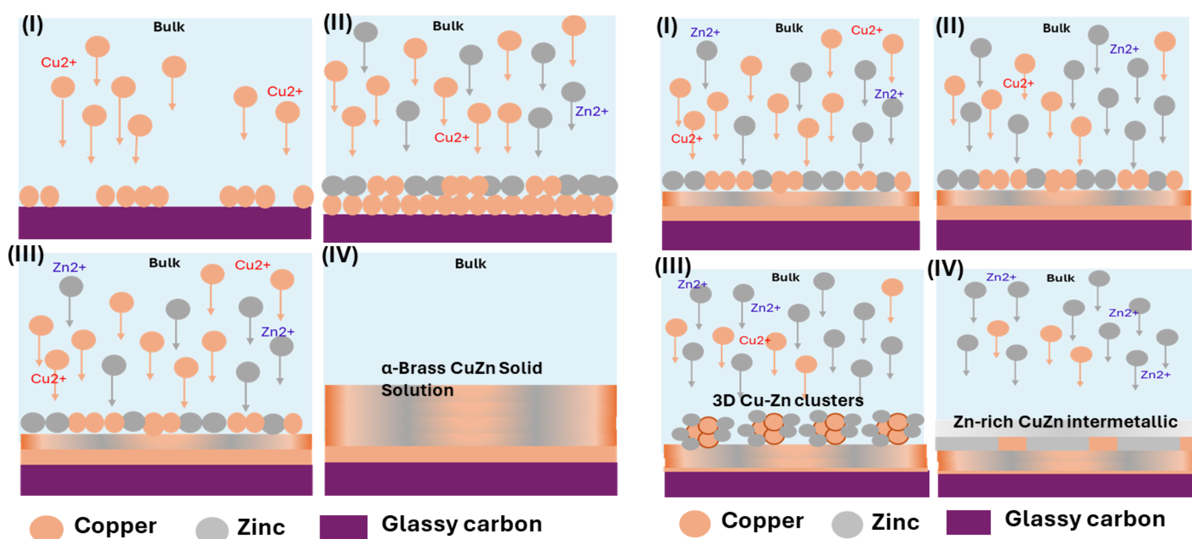

Figure III.2.1: (A) Voltammogram (I-V) and Chronoamperograms (I-t) of Zn-Cu binary (0.05 M each in aqueous solvent) – left at -0.35 V and right at – 1.5 V vs Ag/AgCl; (B) UPD-mediated co-deposition mechanism of Zn & Cu for alloy formation.

When both Zn^{2+} and Cu^{2+} are present in solution, deposition initially proceeds via electrochemical reduction of Cu^{2+}, forming a Cu(111)-textured layer that simultaneously supports UPD of Zn. As deposition continues and Zn atoms become increasingly incorporated, the electrode surface transitions from pure Cu to a mixed Cu–Zn interface. Subsequent Cu deposition now occurs on this modified surface, with a different surface energy, altered electronic structure, and possibly galvanic microdomains. This evolving substrate further catalyzes Cu^{2+} reduction through both direct electrochemical pathways and spontaneous displacement reactions, thereby accelerating Cu accumulation. However, the growing Zn fraction in the deposit weakens Zn–substrate binding affinity, thus progressively shifting Zn^{2+} reduction to more negative potentials and diminishing the efficiency of UPD. This dynamic results in a system where Cu deposition remains dominant through both faradaic and non-faradaic processes, while Zn deposition becomes increasingly dependent on higher overpotentials.

XRD analysis of the sample obtained by potentiostatic electrodeposition at -0.5 V (Figure III.2.2 (A)) reveals a systematic shift of the Cu(111) peak to lower 2θ values in the binary electrolyte, indicative of Zn incorporation into the Cu FCC lattice to form a metastable α-brass solid solution. The absence of distinct Zn(002) reflections supports alloying rather than phase separation. SEM images (Figure III.2.2 (B)) corroborate this by showing smooth, compact morphologies in the low potential regime (around –0.35 V), consistent with layered growth and homogeneous nucleation. EDS analysis of deposits formed in this potential regime reveals a Cu-rich composition with 28 at% Zn, confirming that Zn is incorporated substitutionally into the Cu lattice rather than forming separate domains. These structural and compositional findings align well with the electrochemical trends observed in LSV confirm the formation of α-Brass solid solution of Zn & Cu. In the LSV profile (Figure III.2.1), the initial reduction peak near –0.4 V is shifted positively relative to the Cu-only control experiment, suggesting that the presence of Zn^{2+} accelerates the Cu^{2+} depletion near the electrode. Following this peak, a brief current drop is observed due to local mass transport limitation, where Cu^{2+} and Zn^{2+} ions are rapidly consumed at the electrode interface.

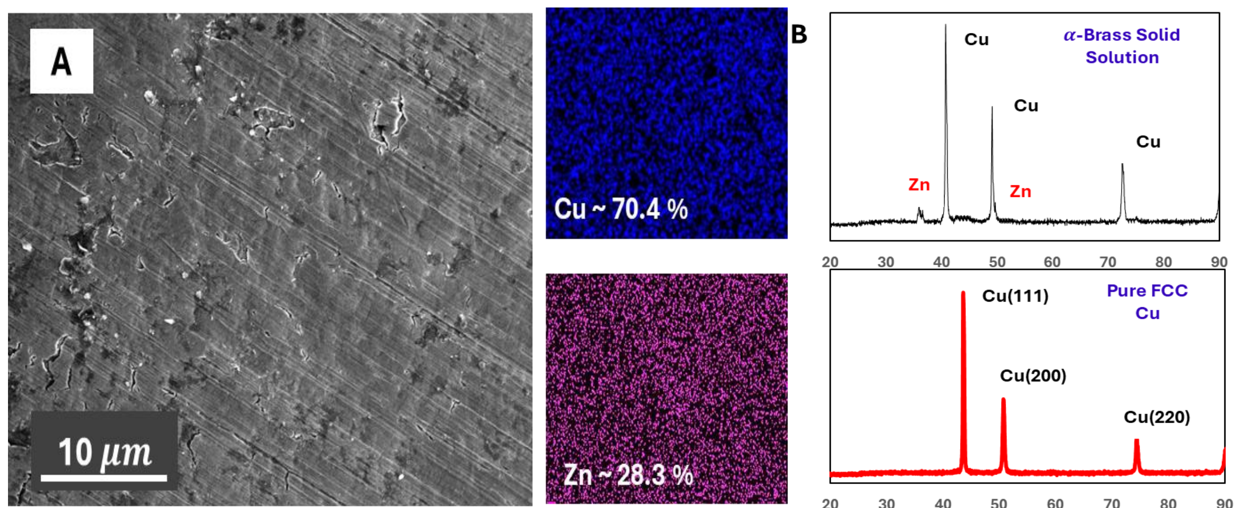

Figure III.2.2: (A) SEM images showing smooth, compact morphologies at low potential (–0.35 V), (B) XRD spectra revealing the Cu-rich alpha brass phase crystallinity vs Pure FCC Cu.

As the applied potential becomes more negative (–1.0 V to –1.65 V), the current response in the binary system surpasses that of both control systems. This marks the transition from interfacial alloying to bulk alloy growth and kinetically enhanced Zn deposition. The rapid current rise in this range can be ascribed to the formation of three-dimensional Cu–Zn clusters (Figure III.2.3). These clusters function as zincophilic scaffolds that facilitate Zn^{2+} desolvation and adsorption. However, deposition in this regime becomes non-epitaxial and structurally more complex, deviating from the smooth layer-by-layer growth observed at lower potentials. SEM images of deposits from this range reveal globular morphologies with increased surface roughness, consistent with 3D cluster formation. EDS results show increased Zn content (~57%), indicating a shift toward Zn-rich intermetallic formation (Figure III.2.3).

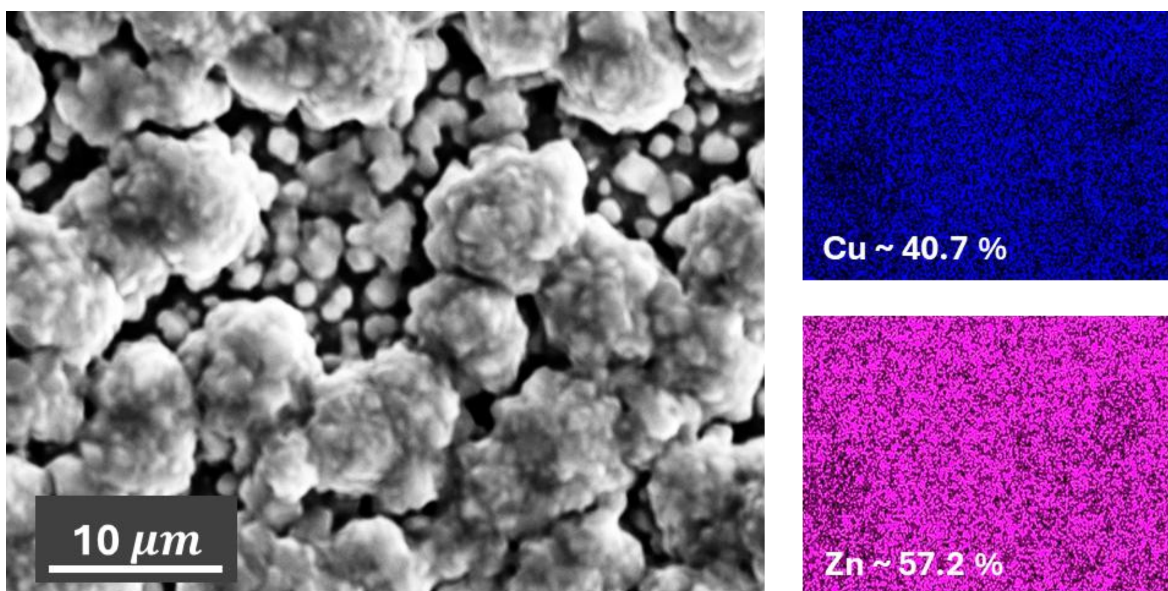

Figure III.2.3: SEM images of deposits from intermediate voltage range revealing globular morphologies with increased surface roughness, consistent with 3D cluster formation. EDS results show increased Zn content (57%), indicating a shift toward Zn-rich growth

Beyond –1.7 V, a subtle inflection in the LSV curve point to a transient diffusion limitation due to Zn^{2+} depletion. This is quickly overcome as the system enters an overlimiting regime, where surface area expansion, enhanced desolvation kinetics, and possibly localized convection promote continued Zn^{2+} transport to the interface. The current rises steeply in this region, and Zn becomes the dominant component in the growing deposit. At this stage, Zn-rich deposits are obtained which are confirmed by significant increase in Zn atomic percentage (~ 76 %) in EDS analysis. In conclusion, the dilute Zn–Cu binary system demonstrates a voltage-dependent transition from Cu-dominated Zn UPD (α-brass alloy formation) to Zn-rich intermetallic growth.

As the concentration of Zn^{2+} and Cu^{2+} salts in the electrolyte are increased from 0.05 M to 0.1 M and 0.5 M, the overall current density in voltammograms increases significantly across all applied potentials (Figure III.2.4), but the mechanistic features of deposition evolve in a more complex and distinguishable fashion. In the underlimiting regime (up to approximately –1.0 V), the I–V trends in both concentrated binary electrolytes resemble those observed in the dilute case, suggesting initial co-deposition of Cu and Zn. However, due to the high ion availability and faster nucleation kinetics, the epitaxial growth characteristic of dilute systems is lost at much lower

potentials in concentrated systems, giving way to the formation of the three dimensional globular Cu-Zn clusters that serve as high-surface-area active centers for further growth. These clusters are observable in SEM (Figure III.2.5) as uniformly distributed fine grains at lower overpotentials, which later coarsen to cauliflower-like structures with increasing voltage. The broader current plateaus and decreased slope in the subsequent diffusion-limited regime suggest that although Cu reduction remains active, the concurrent Zn deposition begins to compete more effectively, modulating the Cu^{2+} flux toward the electrode.

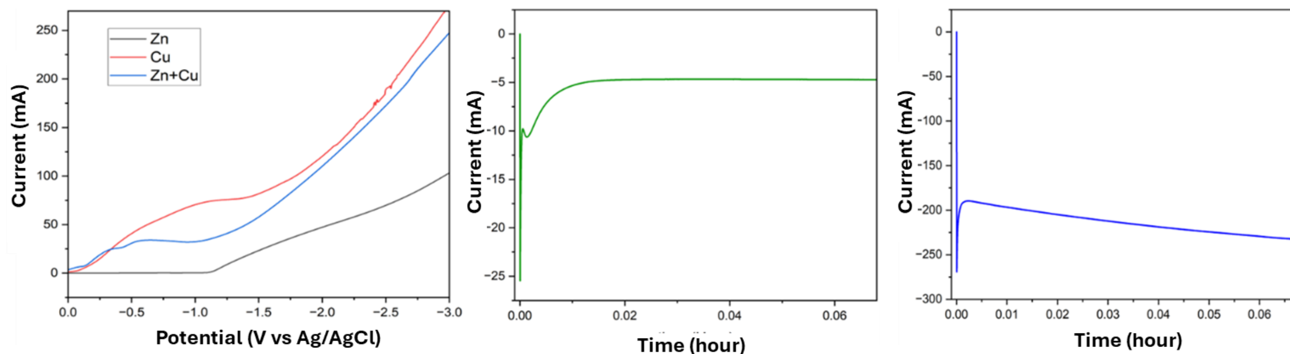

Figure III.2.4: Voltammogram (I-V) and Chronoamperograms (I-t) of Zn-Cu binary (0.1 M each in aqueous solvent) – left at -0.4 V and right at – 1.5 V vs Ag/AgCl

To further investigate the role of the intermediate 3D Cu–Zn cluster growth regime in enabling stable and uniform zinc deposition, a representative potential within -1 to -1.6 V vs Ag/AgCl regime was selected i.e., -1.3 V, and a separate set of structural and electrochemical analyses were performed on the same. The aim was to understand how these Cu–Zn clusters influence Zn^{2+} nucleation behavior, deposition uniformity, and kinetics. In the voltage window from –1.0 to –1.6 V, the formation of globular Cu–Zn alloy clusters create a highly active interface that promotes favorable Zn growth dynamics. These clusters act as a structural and electronic scaffold that lowers the nucleation barrier for Zn^{2+} ions. Due to UPD behavior, Zn preferentially nucleates on the copper domains, leading to reduced nucleation overpotentials. The structure of 3D Cu-clustered hosts allows zinc nuclei to initially form on the cluster surfaces and then expand laterally, filling surface depressions and yielding a smooth, dendrite-free Zn film.

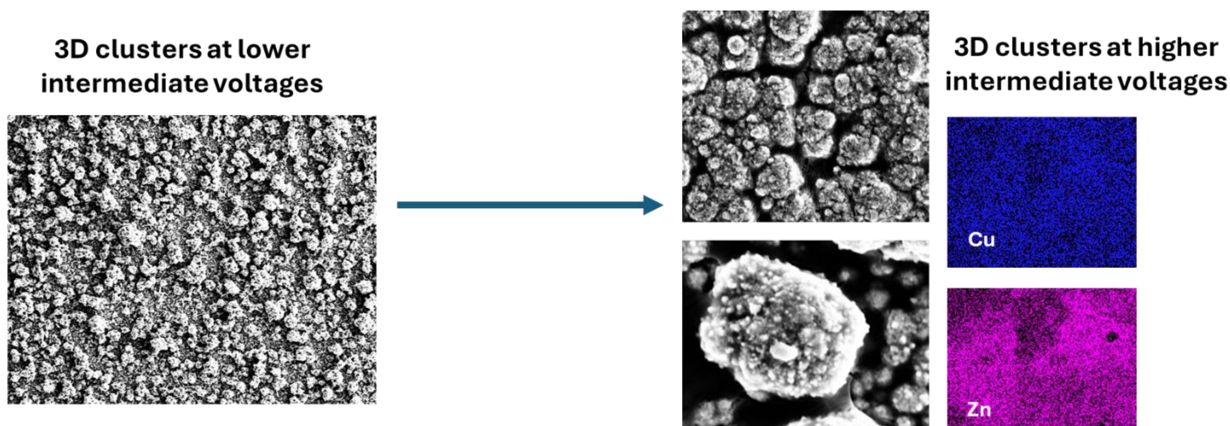

Figure III.2.5: 3D Cu-Zn clusters as fine grains at lower intermediate overpotentials, which later coarsen to cauliflower-like structures with increasing voltage.

Electrochemical impedance spectroscopy reveals that the 3D Cu–Zn cluster-modified electrode exhibits markedly lower charge-transfer resistance compared to the Zn@GC substrate (Figure III.2.6 (A)). This indicates enhanced interfacial kinetics and improved ion/electron transport at the electrode–electrolyte interface. The reduced impedance supports the role of Cu–Zn clusters in facilitating more efficient and uniform Zn^{2+} deposition, validating their function as catalytic active centers. Electrochemical measurements on 3D Cu-Zn cluster deposits systems report Zn nucleation overpotentials as low as 70 mV, in contrast to 100 mV for zinc-on-glassy carbon, highlighting the role of UPD and uniform electron distribution in kinetics (Figure III.2.6 (B)). In addition, the exchange current density of zinc on Zn-Cu clustered structures (7.97 mA/cm^2) exceeds that on bare zinc (7.05 mA/cm^2), affirming the catalytic role of copper in Zn^{2+} reduction (Figure III.2.6 (C)). Morphological comparisons further reveal that while zinc plated on bare Zn substrates tends to form large dendritic chunks, deposition on 3DH-Cu results in evenly distributed, fine zinc particles that coalesce into smooth planes (Figure III.2.6 (D)). Among various heterogeneous substrates studied, copper consistently supports the highest density of active nucleation sites, attributable to the favorable energetics of Zn UPD and potential pseudo-capacitive alloying behavior. These combined effects make the 3D Cu–Zn clustered interface an optimal intermediate for achieving uniform Zn growth prior to the onset of stable Zn-rich deposition at higher potentials.

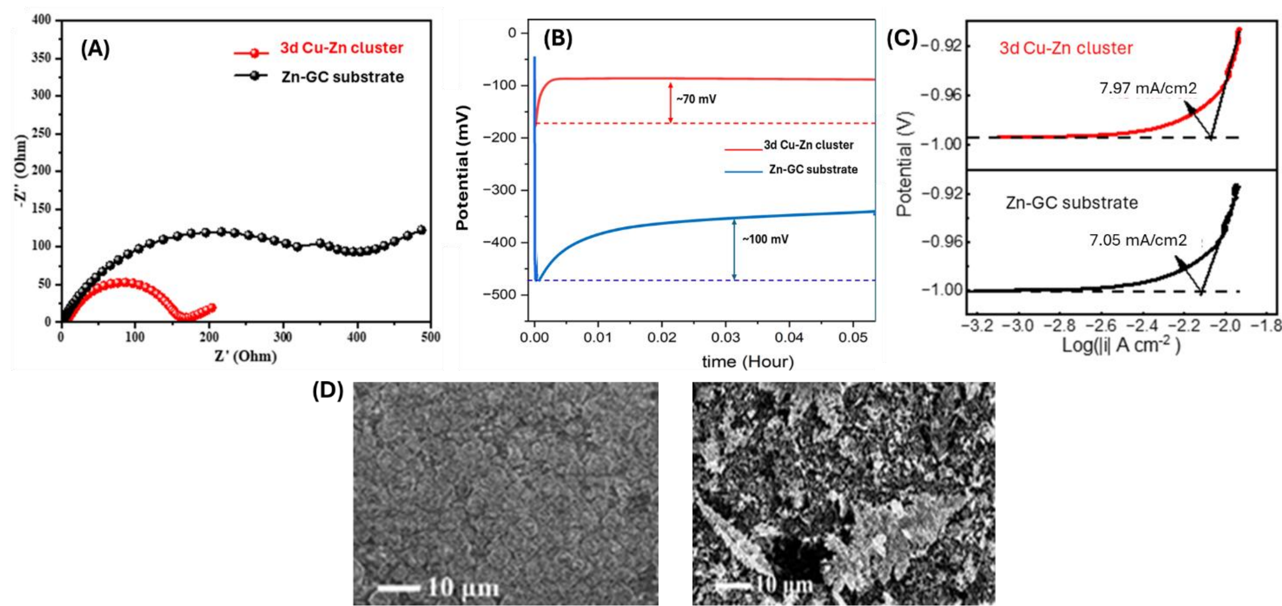

Figure III.2.6: (A) EIS curve of 3D Cu-Zn clusters obtained at intermediate voltages from binary electrolyte vs predeposited zinc on GC substrate. (B) Zn nucleation potentials on 3D alloy clusters and bare Zn-GC, (C) Exchange current density from the polarization curves for 3D clusters for Zn deposition, (D) Morphological comparisons of zinc plated on GC substrate forming large dendritic chunks (right), while deposition on 3D Cu-Zn clusters is evenly distributed laterally (left)

In the 0.1 M Zn–Cu electrolyte, the diffusion-limited plateau in the LSV becomes significantly wider compared to the Cu-only control, where the Cu^{2+} reduction follows classical Butler–Volmer kinetics. In contrast, the binary system exhibits an earlier onset of overlimiting behavior, occurring around –1.25 V (Figure III.2.5 (A)), whereas the exclusive $CuSO_4$ system transitions to overlimiting behavior near –1.45 V. The wider plateau observed in the binary electrolyte is indicative of a mixed cationic transport limitation, where both Cu^{2+} and Zn^{2+} are being depleted near the electrode simultaneously. This co-depletion leads to the formation of a space charge region and contributes to the suppressed current magnitude relative to the Cu-only case. The chronoamperometric curve at –1.5 V (Figure III.2.5 (B)) corroborate this, showing a rapid initial current spike followed by stabilization at lower steady-state currents in the binary system, despite the higher bulk concentration of ions—highlighting the kinetic interplay between rapid Cu nucleation and emerging Zn participation.

In the more concentrated 0.5 M Zn–Cu electrolyte, this behavior becomes more pronounced. The LSV reveals three well-defined regimes: an initial underlimiting region with co-

deposition, a distinct diffusion-limited plateau, and a sharp overlimiting rise beginning around –2.0 V (Figure III.2.7). Interestingly, the exclusive Cu electrolyte at 0.5 M shows no such diffusion plateau, instead displaying an almost linear increase in current consistent with kinetically controlled Cu^{2+} reduction. However, in the binary case, the diffusion-limited behavior re-emerges despite the high ionic strength, indicating a unique interfacial phenomenon: the rate of co-reduction is so significant that Zn^{2+} begins reducing at potentials more positive than its standard value, aided by alloy-favorable nucleation environments and localized desolvation acceleration due to the 3D Cu–Zn clusters.

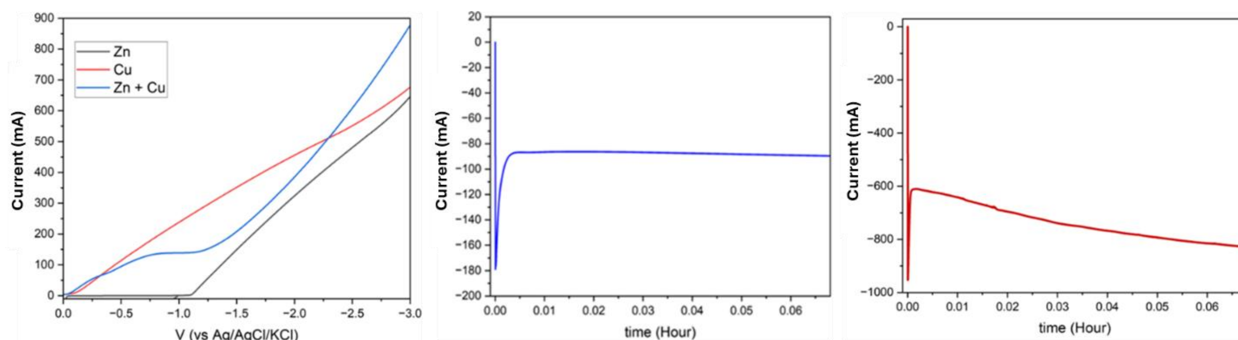

Figure III.2.7: Voltammogram (I-V) and Chronoamperograms (I-t) of Zn-Cu binary (0.5 M each in aqueous solvent) – left at -0.4 V and right at – 1.5 V vs Ag/AgCl

XRD patterns from this regime (Figure III.2.8 (A)) show diminished Cu(111) peak intensity and the appearance of new reflections corresponding to β or γ brass (CuZn) intermetallics, consistent with Zn contents exceeding the α-brass limit [61]. EDS analysis confirms this transition, with Zn atomic percentage increasing from ~56 % at moderate potentials to ~75% at more negative potentials. These compositions exceed the solubility limit of Zn in Cu, indicating that intermetallic phases dominate rather than a substitutional solid solution. SEM imaging shows that the deposit transitions from uniform fine grains at –1.0 V to coarser structures, characteristic of 3D cluster growth and high-rate alloy deposition. However, with further high overpotentials, the subsequent Zn deposit layers are relatively planar and uniform—unlike the rough, dendritic growth typically seen for Zn-on-Zn systems (Figure III.2.8 (B)). This smooth morphology is attributed to the templating effect of the pre-deposited Cu–Zn alloy layer, which facilitates lateral growth and suppresses tip-induced electric field intensification.

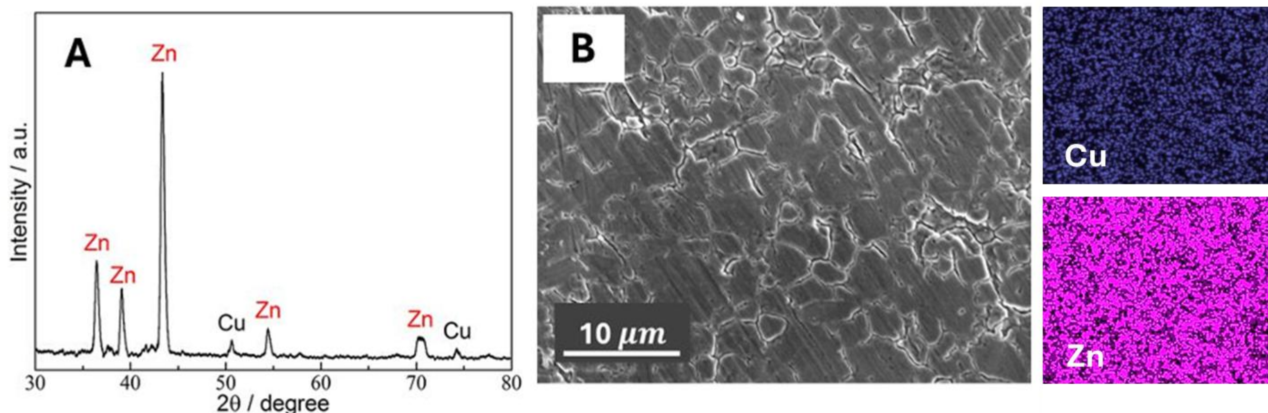

Figure III.2.8: (A) XRD reflections corresponding to β or γ brass (CuZn) Zn-rich intermetallics obtained at higher potentials, (B) Deposit morphology obtained at very high potentials from the mildly concentrated (0.5 M each Zn-Cu) binary electrolyte, exhibiting relatively planar and laterally uniform Zn growth.

Mechanistic Integration & Interface-Controlled Alloy Design in Electrodeposition

The systematic investigation of binary Zn–Cu electrodeposition across a broad concentration and potential range reveals a self-sustaining, underpotential deposition (UPD)-driven mechanism that enables uniform alloy formation between two metals with widely separated redox potentials. At low concentrations (e.g., 0.05 M), Cu deposition dominates due to its more favorable reduction potential, while Zn^{2+} undergoes UPD onto freshly formed Cu(111) surfaces, forming Cu-rich α-brass phases with limited Zn incorporation. The growth in this regime remains sequential and thermodynamically governed, yielding epitaxial films with moderate structural uniformity, as confirmed by XRD and SEM.

As the concentration increases to 0.1–0.5 M, a dramatic transition occurs wherein abundant Cu-rich nucleation sites promote sustained UPD behavior across later deposited layers. In the intermediate potential window (–1.0 to –1.6 V), synergistic co-deposition of Cu and Zn leads to the formation of three-dimensional Cu–Zn alloy clusters that serve as scaffolds. These clusters reduce the nucleation barrier for Zn^{2+} and enhance electron distribution across the interface, resulting in uniform Zn growth. Chronoamperometry indicates improved Zn^{2+} kinetics, while SEM/EDS reveal fine-grained, compact alloy structures. XRD data show a transition from α-brass solid solutions to emerging intermetallic phases as Zn content rises. This cluster-driven deposition mechanism enables dendrite-free Zn growth, even under high overpotentials. The Zn

nuclei initially form on Cu-rich surfaces and grow laterally to form dense, smooth layers—a result of minimized nucleation overpotential (~20 mV) and increased exchange current density. Unlike deposition on bare Zn or inert substrates, which show coarse growth in porous, non-planar morphologies, this interface-guided growth yields structurally stable Zn-rich films. Notably, even in the overlimiting regime (0.5 M), Cu residues in the subsurface continue to template growth and crystallinity. Importantly, this work demonstrates that UPD effects, traditionally limited to monolayer processes, can be harnessed for bulk alloy deposition and morphology control. The identification of optimal deposition conditions (–1.0 to –1.5 V at 0.5 M) offers a practical strategy for achieving high-performance Zn–Cu alloys with tailored electrochemical and structural properties. The insights bridge substrate-limited epitaxy with solvent-mediated interface engineering, thus providing a generalizable platform for compositionally controlled dendrite-free alloy formation via electrochemical interface design.

III.3. Anomalous Co-deposition of Nickel-Cobalt Binary Alloy

Ni–Co binary alloys and their coatings represent a widely studied class of functional materials, particularly valued for their protective, decorative, and magnetic properties. Among the fabrication techniques available, electrodeposition stands out due to its cost-effectiveness, high current efficiency, room-temperature operation, and adaptability for both single-layer and multilayer gradient coatings. Compared to high-temperature methods such as chemical vapor deposition (CVD), sputtering or flame spraying [62-64], electrodeposition offers a simpler and more scalable route to film formation.

Nickel (Ni), a transition metal with a molar mass of 58.69 g/mol and a density of 8.90 g/cm³ at 25 °C, crystallizes in a face-centered cubic (fcc) structure. It has a melting point of 1453 °C and demonstrates excellent corrosion and oxidation resistance under moderate to high temperatures. Ni exhibits negligible electrical resistivity at low temperatures (as low as 68.44 nΩ·m at 20 °C) and is generally considered chemically inert, though its corrosion resistance diminishes in strongly oxidizing environments [59]. Ni also readily forms alloys with a broad range of elements, making it a versatile matrix metal. Cobalt (Co), adjacent to Ni and Fe in the periodic table, has physical properties like Ni — a molar mass of 58.93 g/mol and a density of 8.85 g/cm³. Like Ni, it is ferromagnetic. Structurally, Co adopts a hexagonal close-packed (hcp) form below

417 °C (ε-Co) and transforms into a face-centered cubic (fcc) form (α-Co) between 417 °C and its melting point of 1493 °C [59]. When alloyed, Ni and Co form substitutional solid solutions throughout the entire compositional range, as seen in the binary phase diagram (Figure III.3.1). Such alloys typically exhibit reduced corrosion and wear rates compared to their pure metal counterparts [65].

Due to their superior mechanical strength, corrosion resistance, magnetic behavior, and electrocatalytic activity, Ni–Co alloys are widely explored for advanced engineering applications [59, 62, 63, 65]. Electrodeposition is particularly well-suited for fabricating such alloys. However, the process is often influenced by the phenomenon of anomalous codeposition, wherein Co preferentially deposits over Ni, despite their similar electrochemical potentials ($E°_{Ni}$ = –0.250 V; $E°_{Co}$ = –0.277 V vs SHE). Alloys of Ni, Co, and Fe — three closely related iron-group metals — can form binary and ternary alloy systems via co-electrodeposition, with favorable nucleation behavior due to their comparable standard reduction potentials and overlapping deposition window at highly negative overpotentials [66].

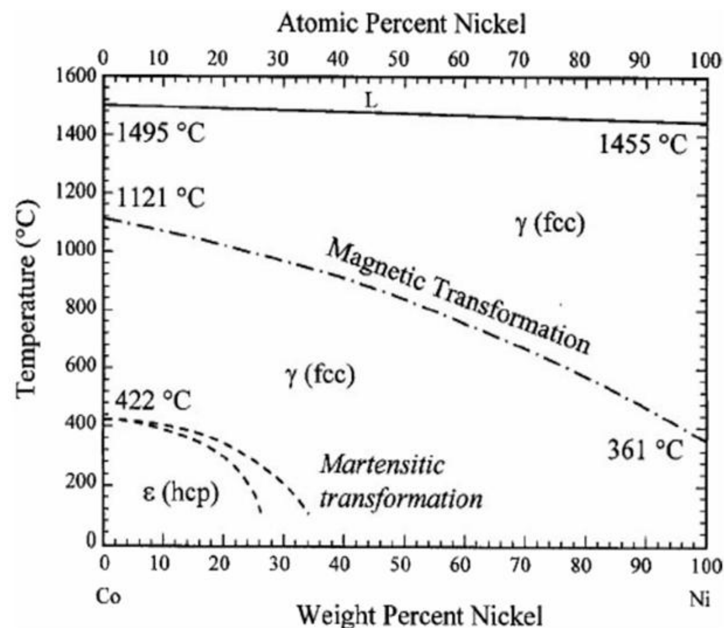

Figure III.3.1: Phase diagram of the Ni-Co binary system [66]

The codeposition of nickel and cobalt is classified as "anomalous" according to Brenner's definition [67], a characteristic behavior commonly observed in systems involving iron-group

metals such as Ni, Co and Fe. Similar anomalous trends have also been reported when these metals are co-deposited with more active elements like zinc or cadmium [68]. In these alloy systems, the elemental composition of the deposit often diverges significantly from that of the electrolyte, which is a result of kinetic and interfacial effects. Interestingly, increasing the concentration of Ni^{2+} ions in the electrolyte often leads to a higher proportion of Co in the deposit, contrary to what might be expected based purely on thermodynamic considerations [67]. For example, in a Watts-type electrolyte where the cobalt-to-nickel sulfate molar ratio is maintained at 1:10, the resulting deposit still contains up to 40 wt.% cobalt — demonstrating a strong deviation from electrolyte composition [69].

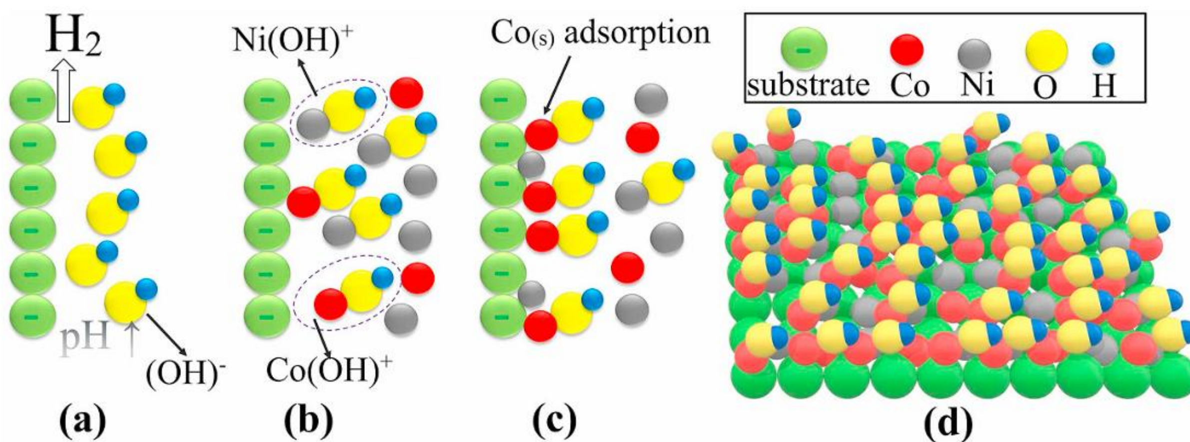

Figure III.3.2: Schematic of anomalous Ni–Co codeposition:(a) Local pH increase near the cathode due to water hydrolysis;(b) Formation of $Ni(OH)^+$ and $Co(OH)^+$ complexes;(c) Preferential adsorption and reduction of $Co(OH)^+$ at the electrode surface blocks Ni^{2+} access, leading to anomalous Co-rich deposition;(d) 3D representation of the resulting non-uniform alloy growth.

Dahms et al. [70] proposed that metal hydroxide species from iron-group metals could adsorb at the electrode interface prior to undergoing reduction. Their interpretation indicated that these adsorbed hydroxides might impede nickel ion reduction, thus restricting Ni content in the electrodeposit. However, later investigations that measured interfacial pH demonstrated that the alkalinity was insufficient to cause metal hydroxide precipitation [71, 72]. Despite this, precise measurement of surface pH continues to pose substantial difficulties in electrochemical environments. Consequently, various research groups have suggested that metal monohydroxy

cations (MOH^+) could directly participate in interfacial charge transfer reactions [73, 74], indicating that metal ion hydrolysis represents an essential mechanistic component in the deposition process.

Expanding upon this concept, Hessami et al. [75] developed a mechanistic framework that integrated one-dimensional mass transport with hydrolysis reactions of metal cations like Ni^{2+} and Fe^{2+}, plus water, within the cathodic zone. Their model proposes that the total cathodic current comprises multiple contributions: reduction of hydrogen ions (H^+), water molecules, and various metal species in both hydrated and hydrolyzed forms — specifically Ni^{2+}, Fe^{2+}, $NiOH^+$, and $FeOH^+$ — all occurring under diffusion-limited conditions. This approach therefore emphasizes how hydrogen and hydroxide species compete during the electrochemical deposition of iron-group metals. Subsequently, Sasaki and coworkers [76, 77, 78] adapted the hydrolysis-based model initially formulated by Grande and Talbot [73] to include other binary alloy combinations like Ni–Co and Fe–Co. Their modified models uncovered inconsistencies between calculated equilibrium constants and experimental observations in Ni–Co systems. To address these disparities, additional refinements were implemented — particularly, incorporating competitive adsorption at the surface between metal hydroxide species and hydrogen atoms, which could obstruct active sites and diminish nickel electrodeposition rates.

A different approach, proposed by Matlosz [79], centered on adsorbed monovalent metal species, particularly Ni(I)-ads, generated as intermediate product during metal cation reduction. This mechanism involves two distinct stages: initially, metal cations adsorb at the cathode interface as monovalent entities, then these surface-bound intermediates undergo further reduction to produce metallic deposits. Baker and West [80, 81] provided experimental verification of this model through electrochemical impedance spectroscopy, which confirmed the two-stage kinetic pathway and established that monovalent adsorbed species govern alloy composition. Arenas and Pritzker [82], expanding on these prior investigations, suggested a mechanistic model comprising three simultaneous reactions during Ni–Co alloy electrodeposition. These encompass separate reduction of Ni^{2+} and Co^{2+} cations, plus additional reactions involving catalytic intermediate species. Podlaha and Landolt [83, 84] previously established that these induced codeposition processes involve formation of entities such as NiCo(II)-ads, which function as catalytic species that enhance Co^{2+}

reduction rates. These pathways operate independently rather than interdependent, representing auxiliary routes that increase cobalt deposition kinetics.

Nevertheless, it is also proposed that although these intermediates may enhance cobalt reduction, they could suppress nickel deposition through occupation of surface sites essential for Ni(I)-ads and Co(I)-ads formation. This competitive surface adsorption creates site blocking effects, diminishing the number of active locations available for nickel reduction. The following reduction of NiCo(II)-ads species represents a continuation of this phenomenon, influencing the final deposition characteristics. Taken together, these various models share a fundamental finding: during anomalous codeposition of iron-group metals, the more reactive (less noble) element preferentially accumulates in the resulting alloy. This outcome contradicts thermodynamic predictions and cannot be rationalized through simple equilibrium considerations. A recurring observation is that when electrodeposition occurs at more negative overpotentials, the cobalt content within the resulting Ni–Co alloy tends to decline [85, 86, 87]. Moreover, inconsistencies persist in the literature regarding the mutual influence of bath constituents on codeposition. While most mechanistic models assume that the presence of the more electrochemically active ion (Co^{2+} or Fe^{2+}) suppresses the reduction of Ni^{2+} — thereby supporting the anomalous codeposition framework — the experimental evidence is not universally consistent. For instance, while many reports confirm that the addition of Fe^{2+} or Co^{2+} ions lead to the inhibition of Ni deposition [88, 89, 90, 91], other studies have shown that this effect is not always significant — with some indicating that Co^{2+} has only a limited or negligible impact on Ni^{2+} reduction [76]. Conversely, in several cases, the presence of Ni^{2+} appears to enhance Co^{2+} reduction rates, although this catalytic or synergistic effect remains mechanistically ambiguous. Some researchers have argued that Ni^{2+} enhances Co^{2+} reduction kinetics [73, 84, 92], whereas others report no such effect [93].

More recently, work by Vazquez et al. [94] explored the competition between Ni^{2+} and Co^{2+} for adsorption sites and found that the surface preferentially stabilizes Co(II) adsorption rather than Ni(II). This insight points to the importance of adsorption energy differences in controlling deposition pathways. Another study [95] linked the anomalous codeposition behavior directly to phase-dependent effects — specifically, the formation of an hcp phase structure during codeposition. Since the solubility of Ni within the hcp cobalt lattice is limited, the incorporation of Ni atoms is kinetically and structurally restricted in this phase. In contrast, normal codeposition

is associated with the formation of the FCC phase, in which Ni can be fully incorporated due to better lattice compatibility and miscibility.

Given the diverse and a few conflicting findings in the literature, the mechanistic understanding of anomalous Ni–Co codeposition remains complex and unresolved. To address this—and to establish a foundational framework for my subsequent efforts toward stable binary alloy electrodeposition—I undertook a systematic investigation of Ni–Co codeposition in a simplified aqueous environment, free from any supporting electrolytes or additives, to isolate and clarify the underlying kinetic and mass transport phenomena. The binary electrolytes were composed of $NiCl_2$ and $CoCl_2$ dissolved in deionized water. The use of chloride counterions, with their relatively small ionic radius and minimal steric hindrance, ensured compact coordination shells near the electrical double layer (EDL), thereby enhancing ion accessibility and reducing non-specific interfacial effects. Five to seven distinct electrolyte compositions were prepared with varying Ni:Co molar ratios ranging from 1:4 to 4:1. In each case, the total metal ion concentration was maintained at 0.05 M to ensure a constant anion concentration across all baths, thereby isolating the effect of cation ratio on deposition behavior. LSV was performed at a low sweep rate of 0.0025 V/s to allow for quasi-equilibrium analysis of the reduction kinetics and onset behavior. The resulting voltammograms for all binary compositions, along with corresponding control setups, are presented in Figure III.3.3, enabling direct comparison of current response, onset potentials, and potential-limited deposition features as a function of bath composition.

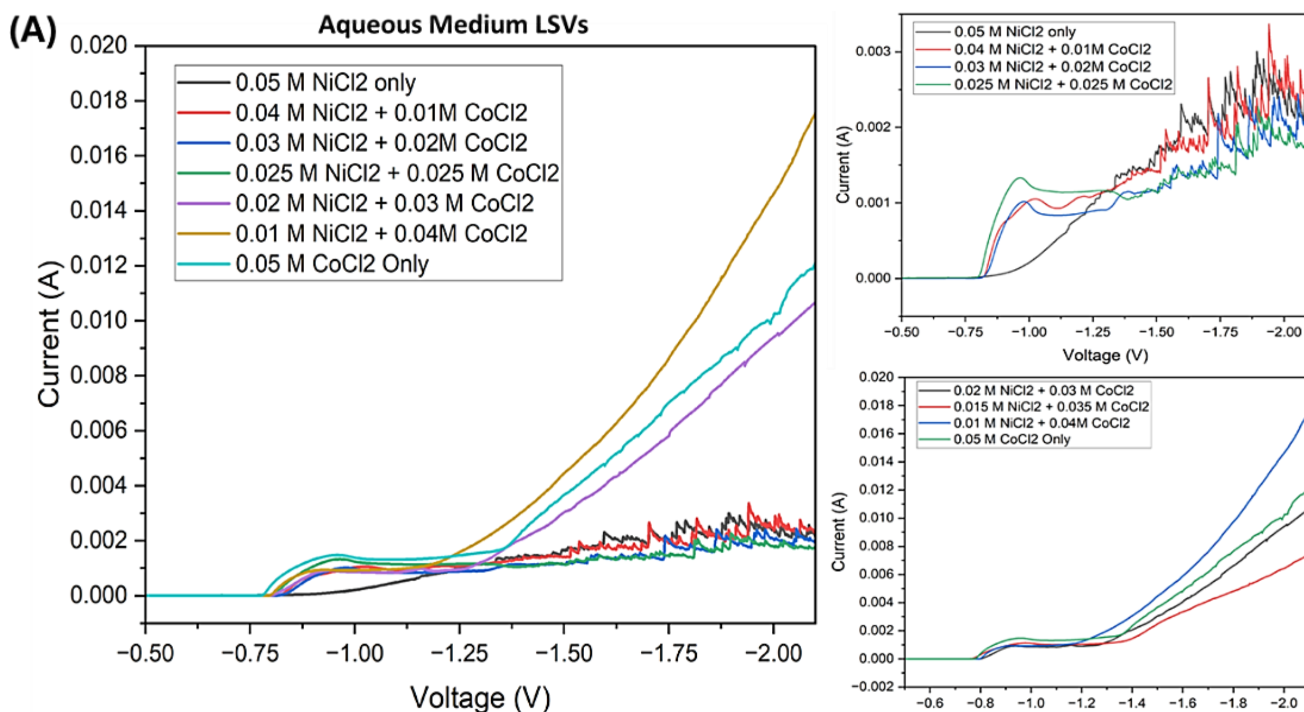

Figure III.3.3: LSV of Ni-Co binary electrodeposition from Aqueous medium (dilute conditions)

Despite similar standard redox potentials, cobalt exhibits more favorable electrochemical behavior than nickel in aqueous media due to differences in hydration and surface interactions. Ni^{2+} exists predominantly as the strongly hydrated $[Ni(H_2O)_6]^{2+}$ complex, requiring significant energy for dehydration prior to reduction, leading to sluggish kinetics and delayed current onset. In contrast, Co^{2+} undergoes faster ligand exchange, allowing for more facile reduction with lower overpotentials. In Ni-rich electrolytes, trace Co^{2+} can hydrolyze to $Co(OH)^+$ near the electrode, blocking active sites and suppressing nickel deposition rather than catalyzing it. Additionally, the overlap of Ni^{2+} reduction with the hydrogen evolution reaction (HER) further reduces faradaic efficiency in Ni-dominant systems. Co^{2+}, by reducing more readily, not only bypasses this competitive HER pathway but also achieves higher current densities and deposition efficiency, demonstrating a redox inversion where Co^{2+} outperforms Ni^{2+} under identical conditions.

III.4. Stable Ni-Co Solid Solution Electrodeposition Regime/Window in Aqueous Solvent

Based on insights drawn from prior studies on Ni–Co electrodeposition in aqueous media, the current experimental system demonstrated comparable anomalous codeposition behavior, wherein nickel deposition remained suppressed across the entire range of binary electrolytes, regardless of the relative Ni^{2+}:Co^{2+} concentration. In the low potential regime (–0.75 V to –1.0 V vs Ag/AgCl),

which is governed primarily by charge-transfer kinetics, voltammetric and morphological analyses revealed significant lateral inhomogeneity, particularly in cobalt-rich bulk electrolytes. The resulting deposits exhibited irregular microstructures and non-uniform nucleation, consistent with unbalanced Co-dominated growth. However, as the bulk Ni^{2+} concentration approached parity with Co^{2+}—notably at 1:1 Ni:Co ratio—and subsequently exceeded it, a marked improvement in compositional uniformity and morphological regularity was observed, even within the same voltage regime (Figure III.4.1). This transition reflects a shift in the interfacial dynamics, where co-reduction becomes more balanced, albeit still favoring cobalt. Within this underlimiting region, deposition adheres predominantly to classical Butler–Volmer kinetics.

Despite the increased Ni^{2+} concentration in Ni-rich baths, EDS analysis confirms that the alloy composition remains cobalt-rich at most binary ratios, indicating that nickel incorporation does not scale linearly with its bulk concentration. This disparity underscores the inherently sluggish kinetics of Ni^{2+} reduction compared to Co^{2+}, which remains dominant even under conditions where nickel is present in substantial excess. An exception to this trend occurs in the 4:1 Ni:Co bulk electrolyte, where the deposited alloy finally exhibits higher nickel incorporation. This suggests that only when nickel significantly dominates in the bulk phase (4 times Co) does its kinetic disadvantage begin to diminish in practical terms. As the applied potential is increased beyond –1.3 V and the system enters the diffusion-limited regime, the voltammetric profiles exhibit a well-defined and extended plateau, indicative of mass transport control (Figure III.3.3). Potentiostatic deposition at potentials within this regime reveals that, for bulk Ni:Co ratios ranging from 0.25 to 2.33, the deposited alloys continue to be cobalt-rich, mirroring the behavior observed under underlimiting conditions. XRD analysis shows that within this regime, equimolar and cobalt-rich compositions favor the formation of HCP Co-rich solid solutions, whereas the 4:1 Ni:Co system, deposited under kinetic control, yields FCC-dominant phase (Figure III.4.1). This contrast highlights the role of local deposition dynamics and lattice compatibility in determining the final crystallographic structure. Notably, the preference for cobalt deposition over nickel remains consistent across both kinetically and diffusion-limited regimes, and across varying bulk compositions, with the sole exception of the highly nickel-rich 4:1 electrolyte, where nickel finally assumes structural dominance.

Another critical observation that aligns well with prior literature is the emergence of pronounced current fluctuations or spikiness in the voltammograms, beyond the diffusion-limited I-V range—particularly for nickel-dominant electrolytes. These fluctuations correspond to increased surface roughness and cracking, as observed in SEM micrographs (Figure III.4.1), and are likely a manifestation of intensified HER competing with metal deposition. The correlation between HER and irregular nickel deposition suggests that surface pH changes and gas evolution can destabilize the Ni^{2+} reduction pathway under high overpotentials. In contrast, cobalt-rich electrolytes (e.g., 1:4 and 2:3 Ni:Co) exhibit relatively smooth and planar morphologies even in the overlimiting regime, with the 1:4 system yielding HCP-dominant solid solution. This observation further reinforces the kinetic favorability of cobalt deposition, its relative immunity to HER interference, and the stabilizing influence of cobalt on deposit microstructure.

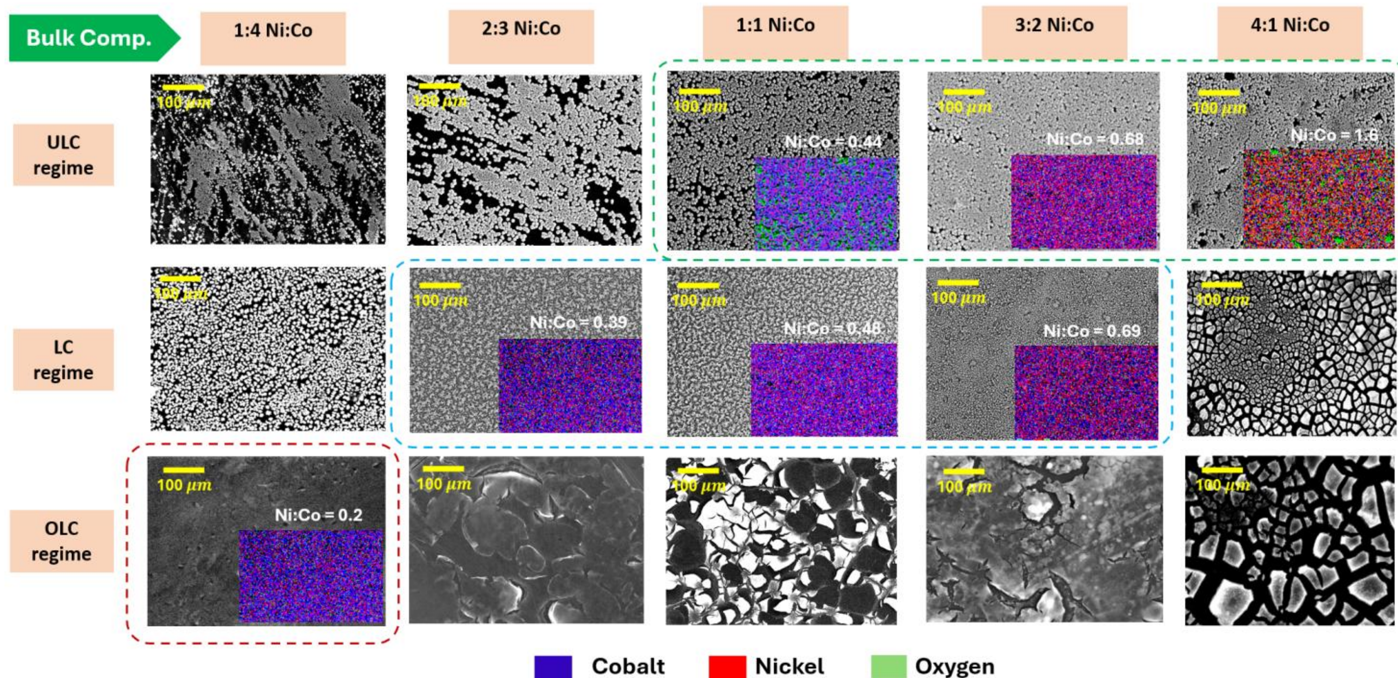

Figure III.4.1 (A): SEM images of Ni-Co electrodeposits in different electrochemical regimes for different bulk electrolyte compositions. Note: The dashed boxes indicate the solid solution alloys.

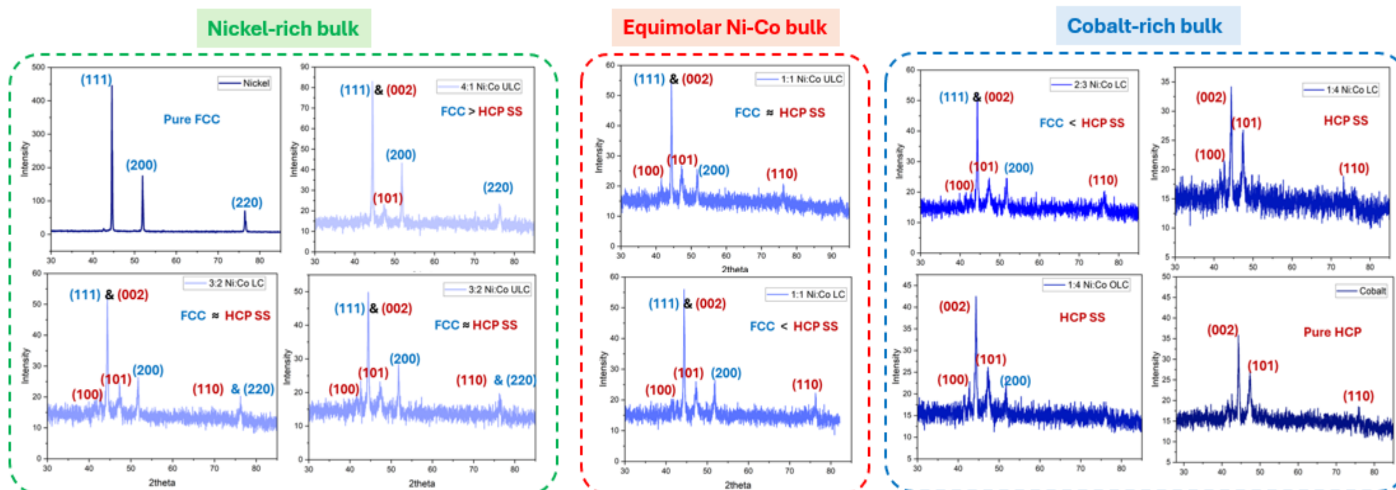

Figure III.4.1 (B): XRD spectra of Ni-Co electrodeposits in different electrochemical regimes for different bulk electrolyte compositions.

In summary, the combined insights from SEM–EDS analysis and XRD-based crystallographic evaluation clearly establish the existence of a tunable solid solution formation window within the Ni–Co binary electrodeposition system in aqueous media. Across the potential regimes investigated, the emergence of uniform, compositionally homogeneous solid solutions is distinctly tied to both the applied voltage and the Ni:Co ratio in the bulk electrolyte. Specifically, solid solutions are reliably obtained within the potential range from –0.75 V to –1.0 V vs Ag/AgCl for nickel-rich bulk electrolytes spanning from 1:1 to 4:1 Ni:Co. In the case of moderately cobalt-rich compositions (2:3 to 3:2 Ni:Co), this window also spreads into the limiting current regime (–1.1 V to –1.3 V). Notably, for cobalt-dominant compositions such as 1:4 Ni:Co, solid solution formation is observed only under overlimiting conditions, at voltages approaching –2.5 V. This progressive shift in the voltage window for solid solution stabilization, from underlimiting to overlimiting with increasing cobalt content, reveals a strong composition–voltage interdependence rooted in the asymmetric electrochemical behavior of Ni^{2+} and Co^{2+} ions. A particularly valuable outcome of this study is the discovery of a consistent linear correlation between the Ni:Co ratio in the deposited alloy and that in the bulk electrolyte across all regimes. Despite the anomalous codeposition behavior—where cobalt tends to be preferentially incorporated—this relationship remains highly linear with an average slope of approximately 0.4 in all potential regimes (Figure III.4.2). When focusing specifically on the regimes that yield stable solid solutions based on both compositional (EDS) and structural (XRD) validation—namely, the underlimiting and limiting

regions—the predictability of this relationship becomes even more compelling. In the underlimiting regime, the correlation follows a linear fit with a slope of 0.3829 (R^2 = 0.9995), while in the limiting regime, the slope is 0.3658 (R^2 = 0.9964) (Figure III.4.2). These strong linearities underscore the feasibility of using bulk electrolyte composition and applied voltage/current as dual control parameters for precisely tuning alloy composition and crystalline phase (FCC vs HCP) in Ni–Co systems. Therefore, this work not only maps out the stable solid solution I-V windows with high experimental fidelity but also offers a predictive framework for targeted alloy synthesis. By selecting appropriate electrolyte compositions and deposition voltages, one can reliably obtain Ni–Co solid solutions with desired atomic ratios and crystallographic structures. This establishes a foundational electrochemical design strategy for the rational synthesis of functional Ni–Co alloys tailored for applications in corrosion resistance, catalysis, magnetic materials, or electrochemical energy systems.

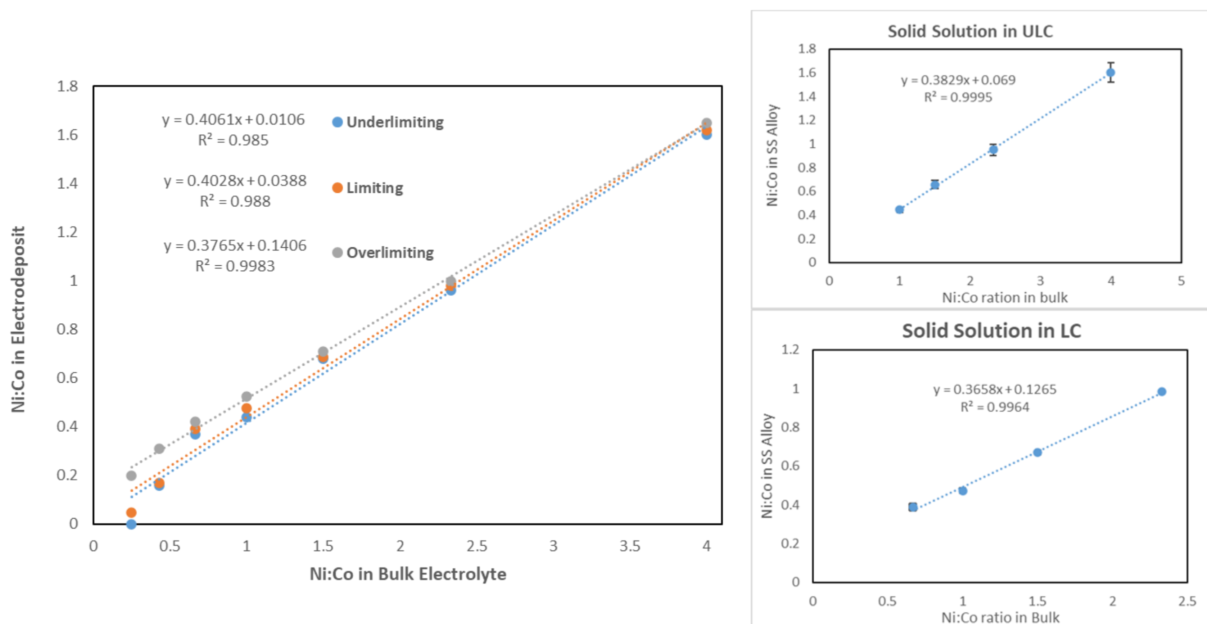

Figure III.4.2: Correlation between Ni:Co in Electrodeposit & Bulk Electrolyte in Aqueous media.

SECTION IV: Mechanistic Exploration & Optimization of Ni–Co Alloy Electrodeposition in Organic Solvent

While zinc and copper possess significantly different standard redox potentials (–0.76 V for Zn^{2+}/Zn and +0.34 V for Cu^{2+}/Cu versus SHE), their alloy formation in aqueous media becomes feasible through underpotential deposition, wherein Zn deposits at a potential more positive than its equilibrium value due to favorable interaction with the freshly deposited copper surface. This heterointerfacial interaction allows Zn to initiate nucleation on Cu substrates, enabling the formation of a stable α-brass phase at lower potentials despite the inherent redox mismatch. Although Zn crystallizes in a hexagonal close-packed (HCP) structure and Cu in a face-centered cubic (FCC) lattice—an apparent structural incompatibility—the atomic size mismatch is ~ 4.7% which is well within the solubility limit. Additionally, the moderately negative enthalpy of mixing between Cu and Zn combined with a moderately high configurational entropy of mixing (~4.93 J/mol·K) lying sufficiently close to the theoretical maximum for binary alloys (~5.76) [96], favored the formation of solid solutions under low voltage kinetically controlled regime as seen in earlier section. This comparative transition from the UPD-driven Zn–Cu alloying to the enthalpy-governed Ni–Co alloying framework provides a broader understanding of how crystallography, electrochemical kinetics, and interfacial thermodynamics collectively govern electrodeposited alloy formation.

In the previous section, the insights from voltammetry and compositional trends reveal a stable solid solution formation window under moderate cobalt enrichment and controlled overpotentials in aqueous solvent. However, limitations such as hydrogen evolution, surface passivation, and restricted potential range motivate a shift toward non-aqueous systems. Dimethyl sulfoxide (DMSO), a polar aprotic solvent with a wide electrochemical window and strong metal complexation capabilities, is introduced to overcome these constraints. Systematic electrochemical studies in DMSO highlight distinct reduction behaviors of Co^{2+} and Ni^{2+}, governed by their respective chloride-DMSO complexation and solvation dynamics. Cobalt, forming labile complexes, reduces readily with well-defined diffusion-limited currents, while nickel reduction is hindered by strong ligand stabilization and higher reorganization energies. Through compositional tuning and voltage optimization in DMSO, a broader and more controllable co-deposition regime is achieved. Notably, cobalt acts catalytically to facilitate nickel reduction, enabling smooth,

phase-pure Ni–Co solid solutions with excellent structural integrity and fidelity to bulk electrolyte composition.

IV.1. Limitations in Ni-Co Electrodeposition in the Aqueous Medium

Hydrogen ion (H^+) reduction occurring simultaneously with metal deposition creates competition at the electrode interface. The depletion of H^+ during deposition causes localized pH elevation, which subsequently promotes the generation of surface hydroxide species — establishing an additional hydroxide-based inhibition pathway for nickel reduction. Under certain deposition conditions, the local pH at the cathode interface becomes sufficiently elevated to allow the hydrolysis of metal ions via their interaction with hydroxide ions (OH^-). This can lead to the formation and accumulation of species such as $Co(OH)^+$, which, when adsorbed on the cathode surface, can obstruct further nickel deposition by occupying critical nucleation sites. Numerous prior investigations focused on the deposition behavior of pure Co, and Ni have identified that the hydrogen evolution reaction (HER) typically proceeds via adsorbed intermediates, notably atomic hydrogen (H-ads) [85]. This presents a notable limitation in the model proposed by Zech et al. [85, 86, 87], which did not incorporate such adsorbed species in its mechanistic considerations. At the electrode surface, adsorption sites may become congested not only by H-ads but also by metal intermediates such as Co(I)-ads, Ni(I)-ads and even bimetallic complexes like NiCo-ads. Competitive adsorption among these species plays a critical role in determining local kinetics and must be properly accounted for in any predictive model. It has been noted in the literature that under more cathodic overpotentials, some reduction reactions may be halted altogether [86], as seen in the suppression of specific mechanistic pathways.

In Ni-rich electrolytes, the elevated concentration of Ni^{2+} promotes the formation of $NiOH^+$ complexes with relatively high stability, which strongly adsorb onto the electrode surface and contribute to passivation. In contrast, the hydrolysis product of Co^{2+}, $CoOH^+$, is more labile and readily dissociates, releasing OH^- ions that react with free protons to form water, thereby shifting the equilibrium backward and mitigating surface blockage. The sluggish kinetics of Ni^{2+} reduction compared to Co^{2+} enhances the competitiveness of the hydrogen evolution reaction (HER), particularly on Ni-rich surfaces. These effects are further reflected in electrochemical behavior: under limiting current conditions, uniform metal films are favored, whereas overlimiting regimes promote dendritic growth. Recent studies have updated classical electrodeposition models

by accounting for the role of monohydroxo species and interfacial hydrogen adsorption, showing that cathodic currents include contributions not only from metal ion reduction but also from water and proton discharge. In Ni-dominant solutions, a post-diffusion spiking behavior is frequently observed at high overpotentials, particularly when the Co^{2+} content is low. This noisy electrochemical response, which diminishes with increased electrolyte stirring or Co addition, is attributed to the combined effects of HER and $NiOH^{+}$ adsorption, which blocks active sites for Ni^{2+} reduction and catalyzes further hydrogen evolution. This is corroborated by visible effervescence at high overpotentials (Figure IV.1.1 (B)), and the resulting morphological irregularities in the deposits (Figure IV.1.1 (A)). Together, these aqueous-phase observations establish a critical baseline for comparison with the behavior of Ni–Co systems in non-aqueous environments.

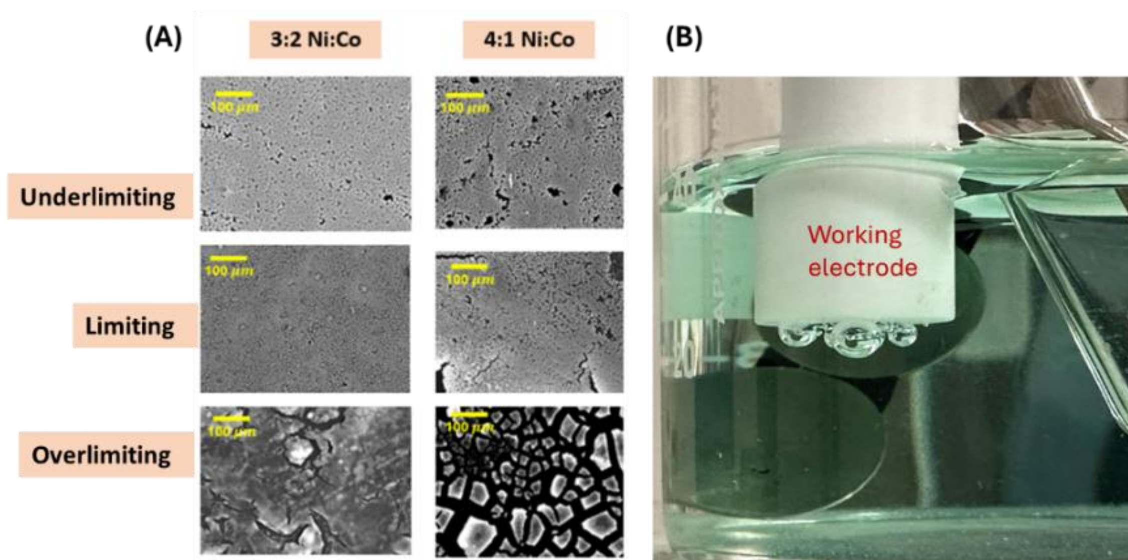

Figure IV.1.1: (A) SEM images of the morphology of electrodeposits obtained at constant potential from Ni-rich aqueous baths; (B) Effervescence observed during Potentiostatic electrodeposition from Ni-rich aqueous baths at high potential

IV.2. Ni-Co Alloy Co-deposition Mechanism in the Non-aqueous Medium

Due to the prevalence of hydrogen evolution reactions (HER) and the emergence of hydrodynamic and morphological instabilities in aqueous systems, we transitioned to a polar aprotic organic solvent that does not participate in proton-based side reactions. Dimethyl sulfoxide (DMSO) was selected as the solvent medium for metal electrodeposition owing to its favorable physicochemical

properties and electrochemical stability. While N,N-dimethylformamide (DMF) was initially considered—given its comparable coordination ability and ability to form similar solvated complexes with Ni^{2+} and Co^{2+} cations [97]—it was ultimately excluded based on a combination of practical and mechanistic limitations. Notably, DMF takes longer time to ensure complete dissolution of $NiCl_2$ and $CoCl_2$ salts, further it has a narrower electrochemical window compared to DMSO and exhibits greater susceptibility to electrochemical decomposition at the negative potentials under study for metal deposition. Furthermore, DMF's weaker donor strength (relative to DMSO) result in less stable metal-ligand complexes [98, 99]. DMSO offers several advantages over conventional aqueous systems & many non-aqueous systems for metal electrodeposition. First, its wide electrochemical window (-4 to +1 V vs. 1M KCl/Ag/AgCl) allows for the reduction of metals at potentials where water undergoes electrolysis. This expanded potential range is particularly crucial for metals like nickel and cobalt, which require relatively negative potentials for reduction. Second, DMSO's high dielectric constant (ε = 46.7 at 25°C) provides excellent solvation of metal ions while maintaining sufficient ionic conductivity even in the absence of supporting electrolyte [100]. This property is essential for our studies, as it allows us to investigate the intrinsic electrochemical behavior of metal complexes without the complicating effects of additional ionic species. Third, DMSO's aprotic nature eliminates hydrogen evolution reactions that compete with metal deposition in aqueous systems, potentially leading to higher current efficiencies and better-quality deposits.

Furthermore, DMSO's strong coordinating ability through its oxygen atom creates metal complexes with predictable electrochemical behavior. Unlike water, which forms labile complexes with rapid exchange kinetics, DMSO complexes exhibit intermediate exchange rates that can be studied using conventional electrochemical techniques (101, 102). This characteristic is particularly important for understanding the mechanistic aspects of co-deposition processes. DMSO coordinates to metal ions through its oxygen atom, forming octahedral $[M(DMSO)_6]^{2+}$ complexes for most first-row transition metals. The S=O bond in free DMSO exhibits a stretching frequency at 1045 cm^{-1}, which shifts to lower frequencies (980-1040 cm^{-1}) upon coordination, confirming oxygen-bonded complexation (103). This coordination mode is supported by the pyramidal geometry at sulfur, which would create steric hindrance for sulfur coordination. In the presence of chloride ions, DMSO molecules within the coordination sphere are successively replaced, forming a series of mixed complexes:

$$[M(DMSO)_6]^{2+} + Cl^- \rightleftharpoons [MCl(DMSO)_5]^+ + DMSO \ (K_1)$$

$$[MCl(DMSO)_5]^+ + Cl^- \rightleftharpoons [MCl_2(DMSO)_4] + DMSO \ (K_2)$$

$$[MCl_2(DMSO)_4] + Cl^- \rightleftharpoons [MCl_3(DMSO)]^- + 3DMSO \ (K_3)$$

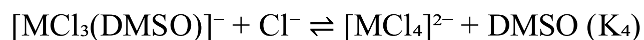

$$[MCl_3(DMSO)]^- + Cl^- \rightleftharpoons [MCl_4]^{2-} + DMSO \ (K_4)$$

The relative stability of these complexes depends critically on the metal ion. For cobalt(II), determined that the trichloro complex $[CoCl_3(DMSO)]^-$ is exceptionally stable, with a formation constant of $\log K_3 = 11.0 \pm 1$. In contrast, the dichloro complex is negligible ($\log K_2 = -2.0 \pm 0.5$), while the monochloro complex shows moderate stability ($\log K_1 = 3.5 \pm 0.5$) [101, 104]. This means that in $CoCl_2$/DMSO solutions, the predominant species are likely to be $[Co(DMSO)_6]^{2+}$ and $[CoCl_3(DMSO)]^-$, existing as the ion pair $[Co(DMSO)_6]^{2+}\cdot 2[CoCl_3(DMSO)]^-$. For nickel(II), the coordination chemistry differs significantly. While $NiCl_2$ also forms octahedral complexes in DMSO, the tendency toward tetrahedral $[NiCl_4]^{2-}$ formation is much lower. Instead, the predominant species in $NiCl_2$/DMSO solutions is $[NiCl(DMSO)_5]^+.[NiCl_3(DMSO)]^-$ (105, 106). These structural differences are visually summarized in the accompanying Figure IV.2.1, which compares the dominant coordination geometries of Ni^{2+} and Co^{2+} in DMSO-based environments. Both metals form octahedral complexes, but with differing ligand arrangements: Ni^{2+} coordinates with five DMSO molecules and one Cl^-, whereas Co^{2+} coordinates with six DMSO molecules exclusively. Additionally, the tetrahedral species depicted show that Ni^{2+} tends to form three-coordinate chloro complexes with weak outer-sphere interactions, while Co^{2+} exhibits tighter Cl^- coordination consistent with its higher complex stability. Moreover, the figure highlights a crucial kinetic difference in ligand exchange behavior. Cobalt (II) complexes undergo rapid ligand exchange, with an estimated exchange rate constant $k_{ex} \sim 10^6\ s^{-1}$ whereas nickel (II) complexes exhibit significantly slower ligand dynamics, with $k_{ex} \sim 10^4\ s^{-1}$. These kinetic disparities further contribute to the distinct electrochemical characteristics observed for Co and Ni systems in DMSO [107, 108].

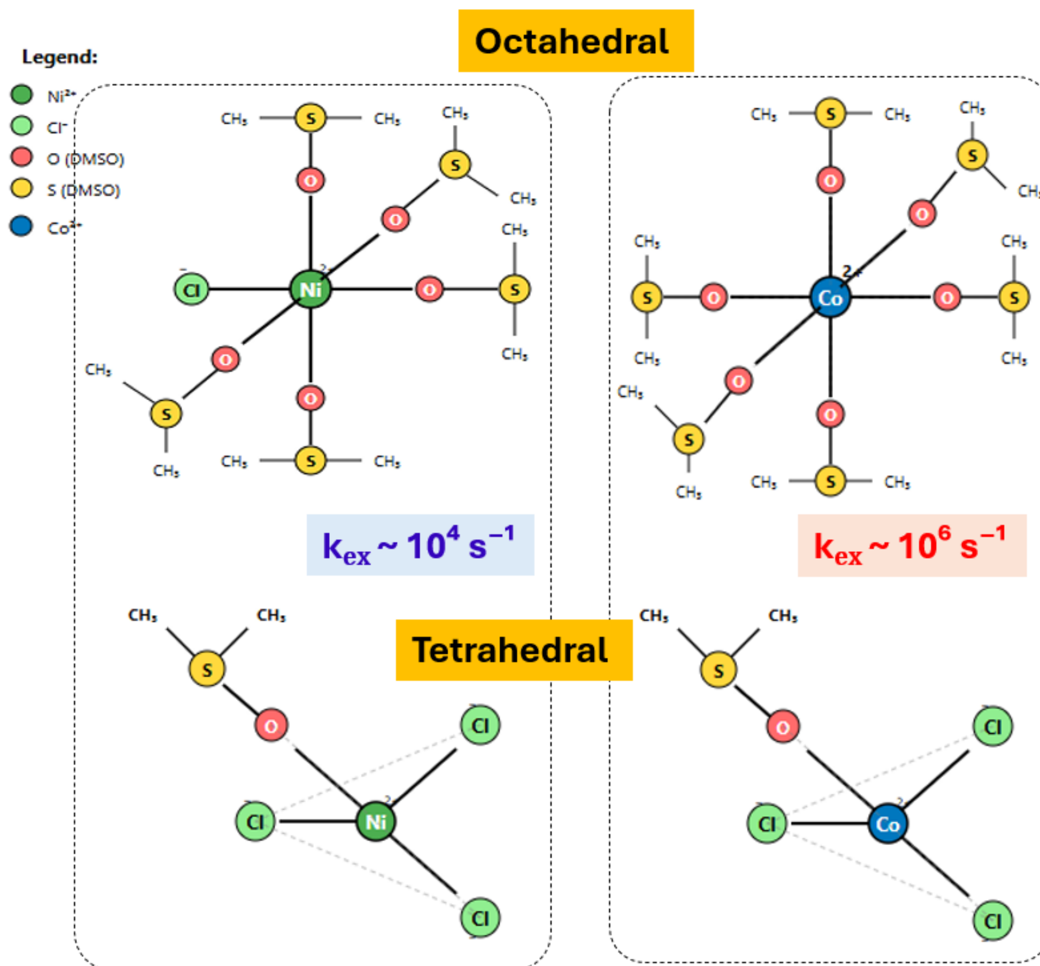

Figure IV.2.1: Different configuration of Stable Nickel and Cobalt Complexes in DMSO

The linear sweep voltammetry (LSV) of $CoCl_2$ in DMSO without supporting electrolyte reveals distinctly different behavior at low (0.05 M) and high (1 M) concentrations, providing crucial insights into the coordination chemistry and electron transfer mechanisms. LSVs in 0.05 M $CoCl_2$ in DMSO solvent, show a gradual onset of reduction beginning at approximately -1.5 V vs. Ag/AgCl, with the current increasing smoothly to reach an ion diffusion limitation (Figure IV.2.2), which is consistent with the reduction of the predominant $[CoCl_3(DMSO)]^-$ complex at around -1.95 V:

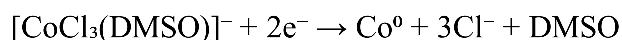

$$[CoCl_3(DMSO)]^- + 2e^- \rightarrow Co^0 + 3Cl^- + DMSO$$

The gradual onset and smooth current rise indicate that nucleation is not a significant barrier to the reduction process. This can be attributed to the labile nature of the cobalt complexes and the

relatively low overpotential required for cobalt deposition. Cui et. al [98] reported similar behavior for $CoCl_2$ in DMF (a similar polar aprotic organic solvent), finding that the reduction proceeds via a single two-electron step with a Tafel slope of 68 mV/decade, exchange current density of 4.94×10^{-7} A/cm², and transfer coefficient of 0.44; these values suggest a relatively facile electron transfer process, consistent with our observations in DMSO.

At 1 M $CoCl_2$ (Figure IV.2.2), the LSV shows a gradual current onset beginning at approximately -0.8 V, with a smooth, ohmic current rise characteristic of a system under enhanced reduction as well as ion transfer. The absence of a sharp nucleation overpotential indicates that Co^{2+} reduction proceeds readily on the glassy carbon substrate. This facile reduction can be attributed to the predominant $[Co(DMSO)_6]^{2+}$ complex in solution. Furthermore, the $[Co(DMSO)_6]^{2+}$ primary form of complex, being positively charged, is easily drawn to cathode and brings the other intermediate to electrode along with it. Therefore, the initial activated control I-V response is expected to be preferentially from the $[Co(DMSO)_6]^{2+}$ complex which tends to align more closely to cathode. Moreover, a clear diffusion-limited plateau is reached, even though the high concentration of Co-DMSO complexes would indicate sufficient material flux to the electrode surface. This is because of the shift of the equilibrium towards more stable complex $[CoCl_3(DMSO)]^-$ after significant Co^{2+} consumption from $[Co(DMSO)_6]^{2+}$. This $[CoCl_3(DMSO)]^-$ complex is anionic and experience repulsive forces from the negatively charged electrode; thereby experiencing slower ionic transport. Also, owing to higher stability constants these require more overpotential to free the Co^{2+} ions from the solvation cloud and deposit as metal; thus, the increase in response after this limitation is due to the Co^{2+} reduction from $[CoCl_3(DMSO)]^-$. Additionally, during the reduction of Co^{2+} from $[CoCl_3(DMSO)]^-$, the freed Cl^- ions are accumulated above the electric double layer (3 moles per mole of Co deposited), creating a high local chloride concentration that maintains the tetrahedral complex as the dominant species near the electrode throughout the remainder of process.

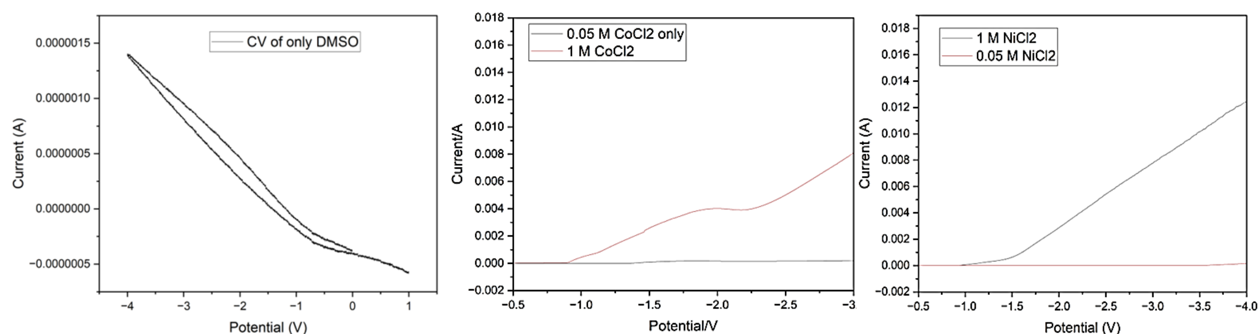

Figure IV.2.2: CV of DMSO reduction, LSV of concentrated Ni and Co non-aqueous electrolytes

In stark contrast to cobalt, $NiCl_2$ in DMSO exhibits complex electrochemical behavior indicative of coupled nucleation/growth and electron transfer kinetics. The LSV in 0.05 M $NiCl_2$ in DMSO shows negligible current until -3.6 V vs. Ag/AgCl, where a sharp current onset occurs (Figure IV.2.2). This behavior is characteristic of an electrodeposition process requiring significant nucleation overpotential. Based on the equilibrium analysis [105, 106, 107], $[NiCl(DMSO)_5]^+$ is likely electroactive & stable.

The electrochemical behavior of $NiCl_2$ in DMSO stands in stark contrast to that of $CoCl_2$, reflecting fundamental differences in coordination chemistry and electron transfer mechanisms. At 1 M $NiCl_2$ (Figure IV.2.3), the LSV exhibits negligible current until approximately –1.0 V vs. Ag/AgCl, beyond which a sharp increase in current is observed. This abrupt onset is indicative of a high activation barrier, suggestive of a kinetically hindered reduction process, possibly involving a nucleation step. At higher concentrations, the population of electroactive Ni^{2+} complexes such as $[NiCl(DMSO)_5]^+$ increases, facilitating more frequent electrode–electrolyte interactions and enabling electron transfer at less negative potentials. Furthermore, the increased ionic strength reduces the electrostatic barrier for charge transfer and improves the conductivity of the electrolyte, both of which contribute to the earlier onset of reduction current. In dilute solutions, the scarcity of Ni^{2+} species near the electrode and the stabilization of more strongly solvated complexes (with higher reorganization energies) delay the onset of reduction.

In contrast to the gradual current rise seen with $CoCl_2$, this sharp transition implies that a significant overpotential is required to initiate nickel deposition, likely due to the strong ligand stabilization of Ni^{2+} in DMSO and a larger reorganization energy associated with its octahedral complex structure. In $NiCl_2$/DMSO or DMF solutions, the predominant species is $[NiCl(DMSO)_5]^+$ rather than a tetrahedral complex [105]. The octahedral coordination complex of

Ni^{2+} in DMSO presents several intrinsic barriers to electrochemical reduction. First, the transition from the octahedral solvated complex to metallic nickel involves a high reorganization energy, as it necessitates the cleavage of six coordinate bonds and substantial geometric rearrangement at the electrode–electrolyte interface. This structural transformation imposes an energetic penalty that slows down the reduction kinetics. Moreover, the Ni–O bonds formed with DMSO are stronger than the corresponding Co–O bonds in cobalt complexes, implying that additional energy is required to break these bonds prior to the reduction step. These combined factors contribute to the sluggish reduction dynamics observed for Ni^{2+} compared to Co^{2+} under identical solvent and concentration conditions. The reduction mechanism involves:

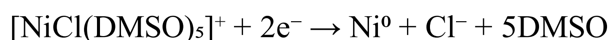

$$[NiCl(DMSO)_5]^+ + 2e^- \rightarrow Ni^0 + Cl^- + 5DMSO$$

At high concentration of 1 M, the current continues to increase steeply beyond the onset potential without reaching a plateau (as in $CoCl_2$) because the solvated ion/complex is cationic in nature and is readily attracted to cathode. The sharp current rise suggests that once nucleation begins, the process is autocatalytic – freshly deposited nickel provides low-energy sites for further deposition. This positive feedback leads to rapidly increasing current until mass transport limitations eventually intervene after -5 V. Another plausible factor concerns the nature of the deposited metal films: cobalt tends to crystallize in a hexagonal close-packed (HCP) structure, typically with a dominant (002) orientation, whereas nickel preferentially forms a face-centered cubic (FCC) phase with a (111) texture. As the HCP cobalt layer thickens, registry loss with the underlying substrate may occur, leading to non-planar or tip-like growths, particularly under high overpotentials. Such morphological evolution can disrupt uniform access of cations to the electrode surface, effectively throttling mass transport despite high bulk concentrations and resulting in the appearance of the diffusion-limited plateau observed in the $CoCl_2$ case.

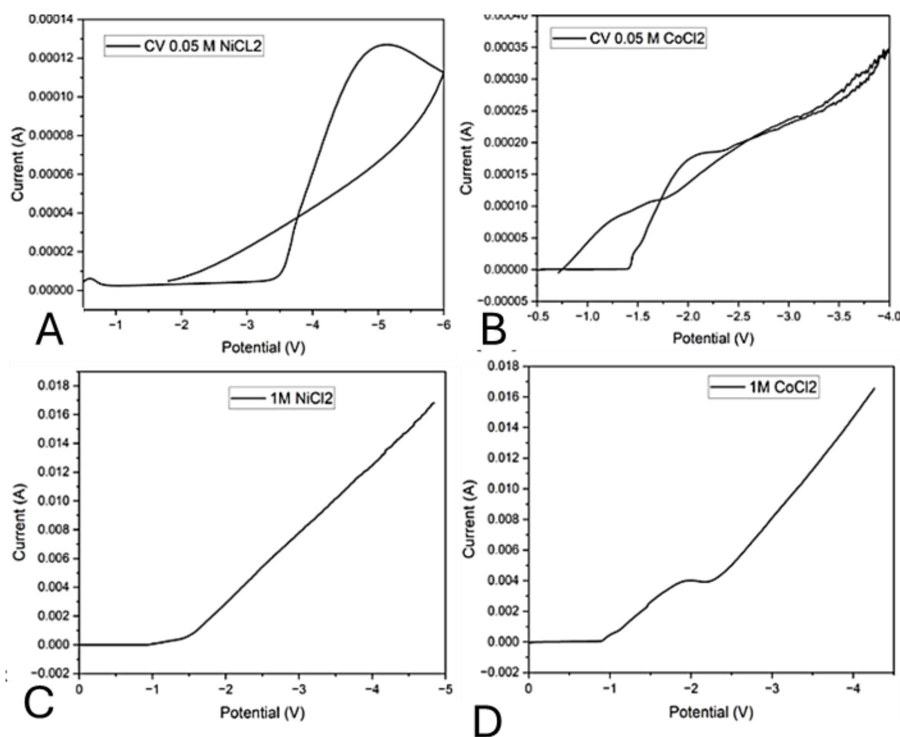

Figure IV.2.3: Comparison of Voltammograms between dilute and concentrated control experiments of Ni & Co electrodeposition in non-aqueous medium

Additional insights are obtained by subjecting the systems to hydrodynamic conditions using a rotating disk electrode (RDE), where enhanced mass transport is expected due to thinning of the diffuse boundary layer. Cobalt deposition, as anticipated, shows improved current responses with increasing rotation speeds, consistent with the classical mass transport enhancement under forced convection. At low $CoCl_2$ concentrations (0.05 M), the RDE experiments reveal classic Levich behavior (Figure IV.2.4). The current reaches a well-defined plateau or depression that increases linearly with $\omega^{-1/2}$, confirming diffusion control. The diffusion coefficient calculated from the Levich slope is approximately 8×10^{-6} cm^2/s, consistent with the relatively smaller $[CoCl_3(DMSO)]^-$ complex. The transition from charge transfer to diffusion control occurs at low overpotentials ($\eta < 100$ mV), indicating exceptional electron transfer kinetics. This is consistent with the labile nature of Co^{2+} complexes, which undergo rapid ligand exchange (k-ex ~ 10^6 s^{-1}). High exchange rates like these indicate that ligands are rapidly entering and leaving the coordination sphere. The metal-ligand bonds are relatively weak and easily broken/reformed.

In contrast, the electrochemical response of 0.05 M $NiCl_2$ (right panel) exhibits anomalous and non-monotonic behavior as a function of rotation speed. At lower rotation rates (up to ~250 RPM),

the current increases with ω and the reduction peak shifts to less negative potentials, consistent with improved mass transport to the electrode and enhanced reduction kinetics. However, beyond 250 RPM, an unexpected reversal in trend is observed—both the magnitude of the reduction current and the sharpness of the peak begin to decline. At the highest rotation speed of 2000 RPM, the voltammogram becomes significantly flattened, with diminished current response and loss of distinct peak features (Figure IV.2.4). This deviation from Levich behavior suggests that additional kinetic or interfacial phenomena begin to dominate at higher rotation rates. One possible explanation lies in the speciation equilibria of Ni^{2+} in DMSO:

$$[Ni(DMSO)_6]^{2+} \rightleftharpoons [NiCl(DMSO)_5]^{+} \rightleftharpoons [NiCl_3(DMSO)]^{-}$$

At moderate rotation rates, the initial reduction of $[NiCl(DMSO)_5]^+$ likely generates Cl^- ions near the electrode surface. These locally accumulated chloride ions shift the above equilibrium toward the formation of $[NiCl_3(DMSO)]^-$, a more readily reducible species with smaller solvation shell, and lower ligand field stabilization. This results in enhanced current at intermediate rotation speeds. However, at very high rotation speeds (e.g., 1000–2000 RPM), the hydrodynamic shear becomes strong enough to rapidly sweep away the generated Cl^- ions from the diffusion layer before they can sufficiently alter the local equilibrium. As a result, the concentration of $[NiCl_3(DMSO)]^-$ near the electrode remains too low to sustain high current densities, and reduction is forced to proceed primarily through the less favorable $[NiCl(DMSO)_5]^+$ pathway. Since this species is more kinetically hindered and involves a larger reorganization energy, the overall rate of reduction decreases, leading to suppressed current despite increased convection. Furthermore, since this equilibrium shift toward $[NiCl_3(DMSO)]^-$ occurs only in the near-electrode region and not in the bulk electrolyte, high rotation rates prevent both the formation and accumulation of this transient, favorable complex. This explains the observed decrease in peak current beyond 250 RPM and the broad flattening of the voltammetric wave at 2000 RPM. These results indicate that the electrochemical behavior of Ni^{2+} in DMSO is governed not only by mass transport but also by complex coordination dynamics and local speciation effects, which are disrupted by high hydrodynamic forces. In summary, the contrasting behaviors of Co^{2+} and Ni^{2+} under identical conditions underscore the critical influence of solvation structure, ligand field effects, and near-surface speciation on metal electrodeposition in non-aqueous solvents. While Co^{2+} reduction

adheres closely to classical diffusion-controlled transport, Ni^{2+} reduction is modulated by complex, shear-sensitive equilibria and interfacial phenomena.

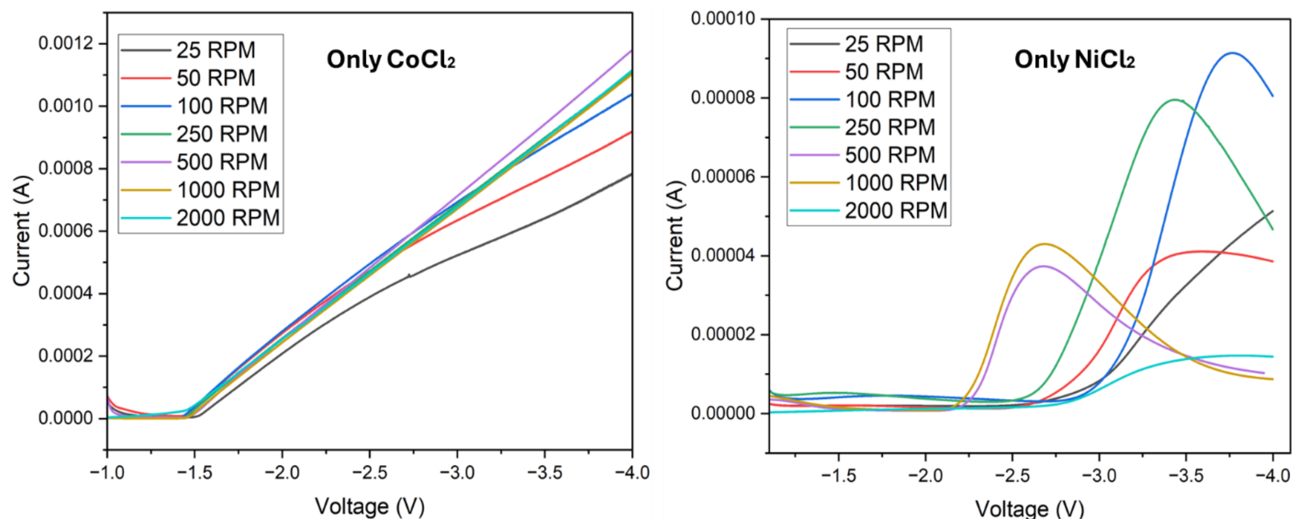

Figure IV.2.4: LSVs of $CoCl_2$ and $NiCl_2$ electrolytes under influence of forced convection (25 rpm to 2000 rpm)

The LSV of the bulk electrolyte containing only 0.05 M $CoCl_2$ exhibits an early onset of cathodic current at approximately –1.3 V vs Ag/AgCl, indicative of the facile reduction of Co^{2+} from the DMSO solvation cloud. When $NiCl_2$ is introduced into the system, even in small proportions, the overall current–voltage profiles of the binary Ni–Co electrolytes maintain a similar qualitative shape to the $CoCl_2$ control, but with notable shifts in both the onset and redox peak potentials toward more negative values. This cathodic shift arises from the introduction of Ni^{2+}, which imposes additional kinetic and transport limitations, primarily due to the slower reduction kinetics and bulky solvation shell of the octahedral $[NiCl(DMSO)_5]^+$ complex. These complexes not only hinder ionic mobility in the diffusion layer but also compete for adsorption and reduction at the electrode surface, thereby delaying the reduction of Co^{2+}. Across all binary compositions studied – 1:4 to 4:1 Ni:Co (total salt concentration being 0.05 M, as in the aqueous case), the cathodic current consistently onsets near –1.8 V, with variations in peak height and total current magnitude reflecting the evolving Ni:Co ratio in the bulk. The onset of the overlimiting regime remains largely consistent around –2.5 V for all compositions except 1:4 Ni:Co. Notably, in the most Ni-rich system, a further cathodic shift of the redox peak is observed, even though the initial current onset overlaps with other cases (Figure IV.2.5). This behavior underscores the significant role of Ni^{2+} speciation and its coordination environment in modulating both the kinetics and interfacial

dynamics of Co^{2+} reduction, highlighting the complex interplay between metal–ligand chemistry and electrochemical response in Ni–Co co-deposition in DMSO.

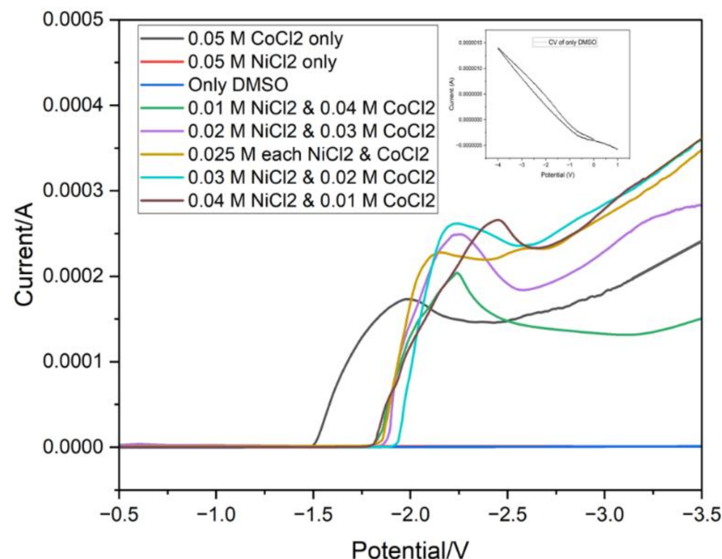

Figure IV.2.5: Linear sweep voltammograms of Ni–Co binary electrolytes with varying Ni:Co cation ratios at a fixed total anion concentration, including control experiments for comparison.

In the 1:4 Ni:Co case, a distinct redox peak appears at –2.2 V. Beyond this, a prolonged diffusion-limited regime is observed, with the current resuming an increase only beyond –3.1 V. The extended plateau reflects transport limitations imposed by the slow-diffusing, bulky Ni^{2+} species. Co^{2+}, although dominant in concentration and readily dissociable from its DMSO solvation cloud, requires a greater overpotential to reduce due to the interference of Ni^{2+} in the EDL. However, once a monolayer of Co is formed, it facilitates co-deposition of Ni that produces an alloy composition closely replicating the bulk – Ni:Co ≈ 0.23–0.25 (Figure IV.2.6 (A)). SEM reveals isolated nucleation clusters at low potentials, which evolve into moderately textured, grainy surfaces by –2.75 V, and increasingly unstable, rough features beyond –3 V (Figure IV.2.6 (B)). While, EDS analysis shows limited S/O accumulation, suggesting minimal surface passivation and a higher likelihood of hydrodynamic instability at deep overpotentials.

In the 2:3 system, the redox peak position remains nearly the same (–2.15 V), but the current magnitude increases due to greater Ni^{2+} involvement. The diffusion plateau shortens compared to 1:4 Ni:Co case, suggesting improved ionic transport. At –2.25 to –2.75 V, SEM reveals a uniform surface with fine grains and minimal porosity, which remains structurally intact even at –3.5 V (Figure IV.2.6 (B)). EDS shows the Ni:Co ratio rising from 0.60 to 1.3, confirming

enhanced Ni^{2+} reduction at high potentials. The increase in sulfur and oxygen content, especially in the overlimiting regime (S ≈ 6.5%, O ≈ 8.4%), suggests the gradual building up of a surface passivation layer with an increase in $NiCl_2$ in the bulk, that helps suppress morphological instabilities (Figure IV.2.6 (A)).

When the concentration of $NiCl_2$ and $CoCl_2$ in the bulk is equimolar, the system represents a balance point, with LSV exhibiting a broad, flattened redox peak and a high overall current magnitude. The diffusion-limited region is further shortened in comparison to the previous compositions, and the overlimiting regime onsets earlier than in 2:3, indicating more synchronized Ni–Co co-reduction. EDS confirms that the deposited alloy is Ni-rich (Ni:Co ≈ 2.13 at overlimiting potentials), even though the bulk is equimolar—reflecting Ni's increasingly favorable kinetics (Figure IV.2.6 (A)). SEM images across all potentials show smooth, dense morphologies without dendritic features. Notably, the overlimiting regime yields compact planar films, corroborating the effect of surface passivation (Figure IV.2.6 (B)). High S (up to 8.1%) and O (up to 9.5%) content supports the hypothesis of a protective organic layer forming due to Ni-driven DMSO adsorption, stabilizing growth even under aggressive field conditions.

Upon further increasing the $NiCl_2$ in bulk to 0.03 M while $CoCl_2$ being 0.02 M, the redox peak remains near –1.8 V, but the current magnitude increases further compared to the 1:1 case. The modestly lower Co^{2+} content still facilitates early nucleation due to its weakly bound solvation shell. The resulting mixed-metal interface promotes synergistic growth, yielding uniform, compact alloy deposits. The diffusion plateau is more prominent than in 1:1 but less prolonged than in 1:4, indicating balanced mass transport. At potentials beyond –2.75 V, the current continues rising steadily. The earlier onset of the overlimiting regime suggests that Ni^{2+} has accumulated sufficiently near the EDL to overcome solvation barriers. SEM reveals highly uniform deposits with minimized porosity (Figure IV.2.6 (B)), and EDS confirms a strong Ni enrichment trend (Ni:Co ~3.2 in the overlimiting regime). S and O levels also rise significantly, suggesting that the passivation layer contributes to the stability of the deposit (Figure IV.2.6 (A)).

At the highest Ni concentration, the system becomes predominantly Ni-controlled. The LSV displays a broad redox region with a continuous current rise beginning near –1.8 V and the earliest onset of the overlimiting regime among all cases. The absence of a sharp peak suggests Ni^{2+} governs the reduction process with minimal Co^{2+} contribution. SEM imaging shows densely packed grains at moderate voltages and near-featureless surfaces at high voltages

(–3.0 to –3.5 V), reflecting the formation of Ni-rich, compact deposits (Figure IV.2.6 (B)). EDS confirms Ni:Co ratios increase from 4.16 to 4.79 as deposition potential increases. S and O levels are highest in this system (S ≈ 16.2%, O ≈ 18.1%), strongly indicating the formation of a thick, passivating oxysulfide layer (Figure IV.2.6 (A)). This layer likely stabilizes the surface, explains the extremely smooth morphology at high overpotentials, and suggests the suppression of tip-enhanced convection and growth instabilities.

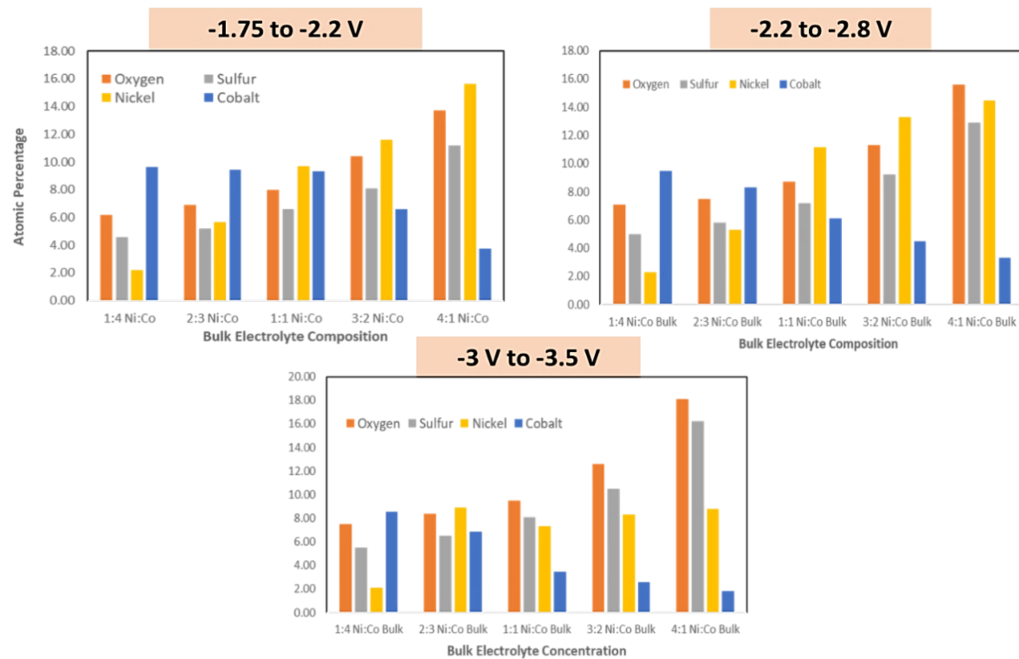

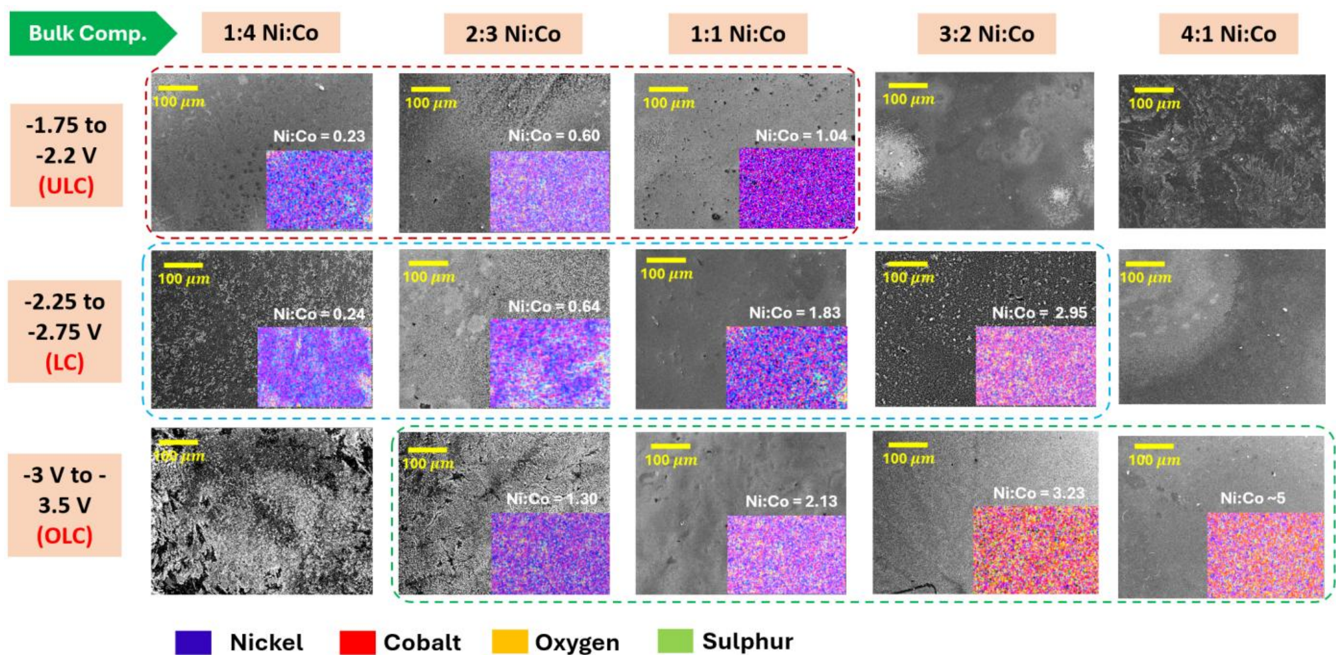

Figure IV.2.6: (A) EDS (electrodeposit composition) results and (B) SEM images of the electrodeposits in different applied voltage windows for each bulk composition studied. Note: The dashed boxes indicate the solid solution alloys.

IV.3. Optimal Window for Stable Ni–Co Solid Solution Alloy Formation

The electrodeposition of nickel-cobalt alloys from DMSO solutions exhibits a pronounced catalytic effect wherein the presence of cobalt dramatically facilitates nickel reduction. This phenomenon manifests as a positive shift in nickel reduction potential, decrease in nucleation overpotential, and enhanced deposition kinetics in mixed metal systems compared to pure nickel solutions. Understanding this catalytic mechanism is crucial for controlling alloy composition and morphology in non-aqueous electrodeposition systems.

1. Active Center Formation and Surface Modification

The fundamental basis of cobalt's catalytic effect lies in its ability to create energetically favorable nucleation sites for nickel deposition. When cobalt deposits first, it forms a metallic surface with distinct electronic properties compared to the substrate. The d-band electronic structure of metallic cobalt (d^7 in Co^0) provides optimal orbital overlap with incoming $[NiCl(DMSO)_5]^+$ complexes, facilitating electron transfer. The work function of cobalt (5.0 eV) is lower than that of typical substrates like glassy carbon (~5.5 eV) or even nickel itself (5.15 eV). This lower work function reduces the energy barrier for electron tunneling to nickel complexes, effectively lowering the activation energy for nickel reduction (109). Additionally, freshly deposited cobalt atoms possess high surface energy and numerous defect sites owing to HCP crystallinity (steps, kinks, and adatoms) that serve as preferential nucleation centers [110]. These high-energy sites can stabilize the transition state during nickel complex reduction, following the relationship [111]: $\Delta G^*_{nucleation} = (16\pi\gamma^3\Omega^2)/(3(\Delta G_v + \varepsilon)^2)$; where the presence of cobalt modifies the surface energy landscape, though the exact mechanism of how cobalt affects the interfacial energy γ and adhesion energy ε requires further investigation.

2. Complexation Equilibria and Ligand Exchange Dynamics

The catalytic effect is profoundly influenced by the different complexation behaviors of cobalt and nickel in DMSO. Cobalt's preference for tetrahedral $[CoCl_3(DMSO)]^-$ complexes versus nickel's octahedral $[NiCl(DMSO)_5]^+$ complexes creates a unique interfacial environment during co-deposition. When $[CoCl_3(DMSO)]^-$ reduces at the electrode surface:

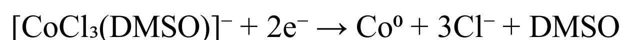

$$[CoCl_3(DMSO)]^- + 2e^- \rightarrow Co^0 + 3Cl^- + DMSO$$

The reaction releases three chloride ions per cobalt atom deposited, creating a high local chloride concentration at the interface. This chloride accumulation drives the equilibrium of nickel complexes toward more easily reduced species:

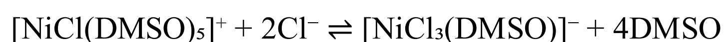

$$[NiCl(DMSO)_5]^+ + 2Cl^- \rightleftharpoons [NiCl_3(DMSO)]^- + 4DMSO$$

The anionic $[NiCl_3(DMSO)]^-$ complex has a less negative reduction potential than the cationic $[NiCl(DMSO)_5]^+$ due to decreased coordination number and stability (relatively easy dissociation). This chloride-induced speciation supposedly accounted for a ~200-250 mV positive shift in nickel reduction potential in LSV. Furthermore, the rapid ligand exchange kinetics of cobalt complexes ($k\text{-}ex \sim 10^6\ s^{-1}$) creates a dynamic interfacial region where DMSO and chloride ligands are constantly redistributing. This dynamic environment can facilitate the transformation of slowly exchanging nickel complexes ($k\text{-}ex \sim 10^4\ s^{-1}$) through a ligand-assisted mechanism:

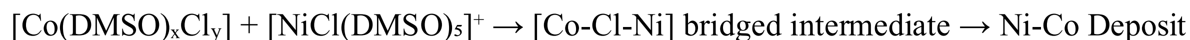

$$[Co(DMSO)_xCl_y] + [NiCl(DMSO)_5]^+ \rightarrow [Co\text{-}Cl\text{-}Ni] \text{ bridged intermediate} \rightarrow \text{Ni-Co Deposit}$$

4. Electronic Effects and D-Band Interactions

The electronic structure of the cobalt-modified surface plays a crucial role in catalyzing nickel reduction. Density functional theory calculations on Ni-Co surfaces (112) show that cobalt atoms increase the d-band density of states near the Fermi level, enhancing the surface's ability to donate electrons to approaching nickel complexes. The d-band center (εd) of cobalt-rich surfaces is closer to the Fermi level than pure nickel surfaces, following the relationship (113): Activation Energy $\propto |\varepsilon d - \varepsilon F|$. This electronic modification reduces the activation energy for breaking Ni-O bonds in

$[NiCl(DMSO)_5]^+$ complexes, facilitating the rate-determining step of DMSO ligand displacement during reduction.

Initial cobalt deposition forms catalytically active sites that promote subsequent nickel reduction, potentially skewing alloy composition unless controlled—particularly under kinetically dominated conditions. Operating in a mass transport-limited regime helps stabilize the target stoichiometry. Cobalt also lowers the nucleation barrier for nickel, encouraging layer-by-layer growth and yielding smoother, denser deposits—consistent with the transition from nodular Ni to compact Ni–Co morphologies. Additionally, cobalt enhances efficiency by enabling Ni reduction at less negative potentials, suppressing side reactions such as DMSO decomposition (even though less likely in that window). Its presence narrows the potential gap between Ni and Co reduction, supporting true co-deposition over sequential plating. Across the full range of Ni:Co electrolyte compositions, the electrochemical response, deposit morphology, alloy composition, and key electrochemical descriptors evolve systematically, revealing a progressively widening and stabilizing regime for solid solution formation as the bulk composition shifts from Co-rich to Ni-rich domains.

In Co-rich systems such as 1:4 Ni:Co, the electrochemical response is governed by the facile reduction of Co^{2+}, resulting in early onset potentials and distinct redox features. However, the limiting current remains low, and the diffusion-limited window is narrow, reflecting strong mass transport limitations. SEM imaging reveals porous and rough morphologies at higher voltages, with minimal sulfur and oxygen detected by EDS, implying insufficient surface passivation in Co-rich environment (due to less stability of Co-DMSO complexes). XRD patterns in this case predominantly exhibit HCP phases, with peaks near $2\theta \approx 41.7°$ and $44.4°$ corresponding to the (100) and (101) planes (Figure IV.3.1 (A)). Transitioning into more balanced compositions such as 2:3, 1:1 and 3:2 Ni:Co, the system exhibits significant improvements in co-deposition behavior. The onset potentials shift slightly cathodically (–1.80 to –1.85 V), yet the total current and exchange current values increase markedly (e.g., $I_0 = 0.27$ A for 3:2), indicating enhanced charge transfer kinetics. These systems also display higher limiting currents (up to 0.23 A) and wider limiting plateaus ($\Delta V \approx 0.400$–0.750 V), which suggest significant ion-transport limitation and better surface accommodation. SEM images revealed smooth, uniform morphologies with reduced porosity even under deep overpotentials. The evolving XRD profiles further corroborate

alloy homogeneity: overlapping with mild HCP reflections, FCC peaks become prominent, including (111) at 44.5°, (200) at 51.8°, and (220) at 76.4°, confirming the emergence of a stable, Ni-rich Ni–Co alloy FCC solid solution (Figure IV.3.1 (A)). As the system becomes Ni-dominant, the electrochemical response reflects accelerated kinetics driven by $[NiCl(DMSO)_5]^+$ reduction, as evident from the increased exchange current magnitude. The onset potential shift positively, and the I-V curve displays a smooth, continuous rise without distinct peaks—indicating a kinetically dominated process. Exchange current density remains high ($I_0 \approx 0.20$ A). XRD analysis reveals clean FCC phase dominance, with sharp (111), (200), and (220) peaks, signifying pure Ni-rich solid solution formation (Figure IV.3.1 (A)).

The development of passivation layers—comprising of DMSO adsorbed preferentially with Ni-rich systems—not only mitigates tip-enhanced convection but also contributes to the homogenization of the interfacial electric field, thereby stabilizing growth during electrodeposition. These effects manifest distinctly across evolving electrochemical-morphological regimes, which shift predictably with increasing Ni content in the bulk electrolyte. In the voltage range spanning –1.75 to –2.2 V, the system is Co-dominated, yielding HCP phases, minimal passivation and highly porous/irregular morphologies due to limited surface stabilization. As the voltage shifts closer to the diffusion-limited regime (–2.25 to –2.75 V), a balanced co-reduction of Ni^{2+} and Co^{2+} emerges with uniform morphology and optimal passivation. Finally, in the overlimiting current regime beyond –3 V, deposition becomes Ni-dominated, resulting in dense FCC phase formation, the accumulation of a robust passivation layer, and extremely stable, smooth film morphologies (Figure IV.3.1 (B)). This voltage-dependent regime progression underscores how both alloy composition and electrochemical stability can be modulated by tuning the applied potential and Ni:Co ratio, allowing for precise control over solid solution formation in DMSO-based systems.

(A)

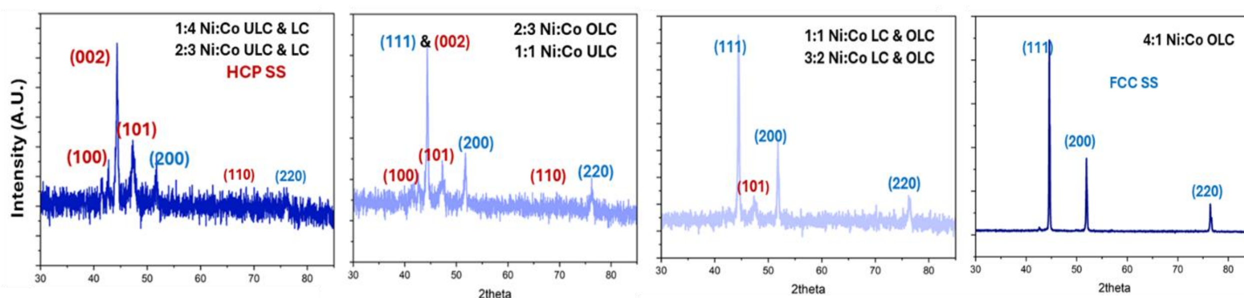

(B)

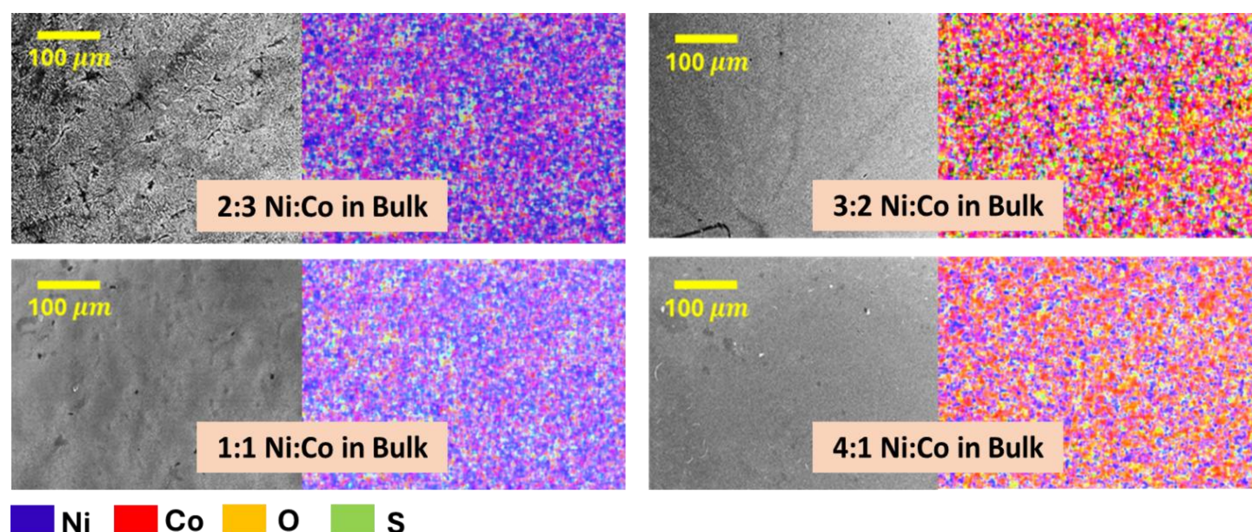

Figure IV.3.1: (A) XRD of the solid solution alloys of Ni-Co obtained in different regimes in different bulk composition. (B) SEM and EDS mappings of the deposits obtained at high over-limiting voltages in the Ni-rich electrolytes showing the passivation effect on suppression of instabilities.

An essential feature of alloy formation in non-aqueous DMSO media is the exceptional agreement between the bulk Ni:Co ratio and the resulting alloy composition particularly at the onset of limiting-current window (–2.2 V to –2.5 V), where stable solid solution formation is most favorable. Quantitative EDS analysis reveals that the Ni:Co atomic ratio in the electrodeposit closely replicates the electrolyte composition during this intermediate regime, with a near-perfect linear fit ($R^2 = 0.9952$, slope ≈ 1.05), as shown in Figure IV.3.2. This stands in stark contrast to aqueous systems, where significant deviation from the bulk is observed due to competitive adsorption effects.

For 2:3 to 3:2 Ni:Co bulk compositions, in the aforementioned window, the alloying process is synergistically governed by the simultaneous reduction of both Ni^{2+} and Co^{2+}. These factors, coupled with the formation of a moderate yet stabilizing sulfur- and oxygen-rich passivation layer, enable uniform co-deposition with minimal compositional drift. In this regime, XRD patterns show overlapping/coincident HCP and strong FCC peaks—evidence of solid solution behavior with slightly shifted peaks but without phase segregation or intermetallic formation. In the ULC regime (–1.75 to –2.2 V), where Co reduction dominates, alloy composition

mirrors the bulk only at low Ni fractions (e.g., 1:4 and 2:3), but overall predictability is limited due to sluggish Ni^{2+} incorporation and asymmetric growth rates. Conversely, in the OLC regime (> –3 V), although the alloy becomes increasingly Ni-rich and deposition remains smooth, the ratio begins to diverge from bulk values as Co^{2+} becomes kinetically suppressed. While still forming FCC solid solutions, this regime is less ideal for precise compositional tuning.

Thus, close to limiting current window not only delivers structural and morphological uniformity but also offers compositional fidelity, making it optimal for tailored alloy synthesis. This tight correlation between bulk composition and resulting alloy underscores the predictive power of DMSO as a solvent and highlights the potential for rational design of multi-metallic systems based on electrochemical descriptors such as exchange current, limiting current, and voltage window width.

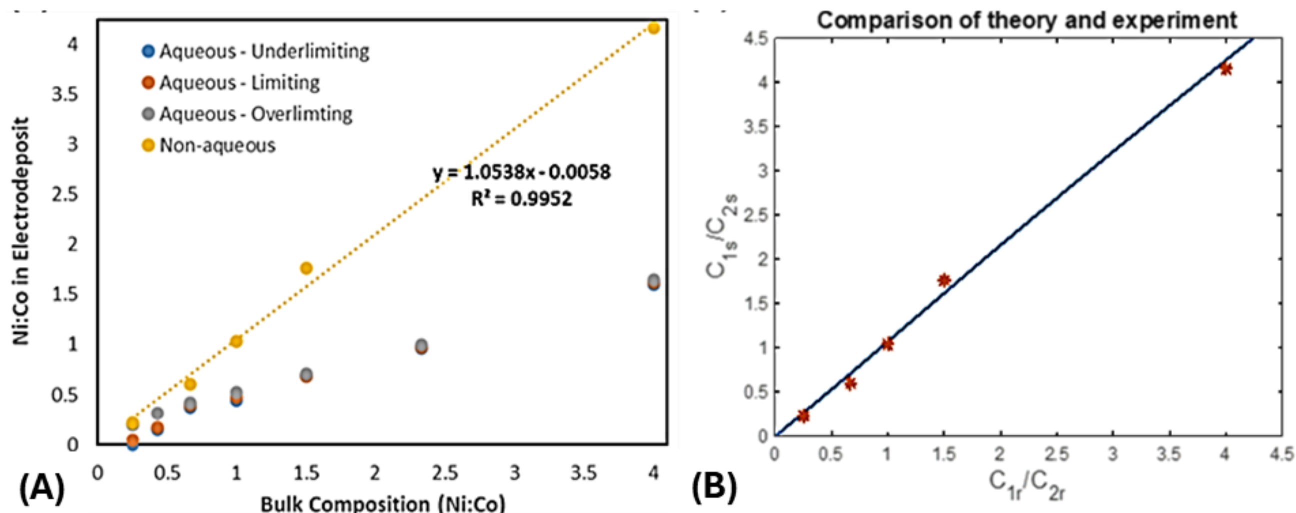

Figure IV.3.2: (A) Correlation between the Alloy and Bulk electrolyte composition in the non-aqueous medium and its comparison with the aqueous medium results. (B) Comparison of experimental alloy composition with the theoretical results (for non-aqueous environment).

Conclusion & Future Perspective

This thesis establishes an experimental framework for interface-controlled electrodeposition, demonstrating that crystallographic orientation, electrochemical driving force, and interfacial chemistry can be synergistically tuned to engineer uniform, compact, and highly reversible metal coatings. The work integrated systematic studies on single-metal (Zn) deposition and binary alloy systems (Zn–Cu and Ni–Co), offering mechanistic insights that extend well beyond empirical optimization and move toward predictive electrochemical interface design.

We began by addressing a fundamental limitation in conventional battery electrode architectures: the lack of crystallographic control of the substrate, which contributes to irregular nucleation, poor adhesion, dendrite formation, and irreversible growth behavior. Recognizing that electrochemical cells inherently possess uniaxial symmetry along the electrode normal (Pec), we investigated a scalable strategy to exploit this symmetry by fabricating Cu(111)-textured current collectors using cold compaction and thermal annealing. These textured Cu substrates act as crystallographic templates that induce strong epitaxial alignment of Zn(002) during electrodeposition. Extensive structural and electrochemical characterization confirms that Zn deposited on Cu(111) grows in a compact, planar and highly oriented manner, with significantly reduced nucleation overpotentials and outstanding Coulombic efficiencies exceeding 99% over thousands of cycles. SEM and XRD studies demonstrated that Zn(002) growth on Cu(111) follows a lattice-matched epitaxial pathway, preserving long-range orientation over hundreds of microns in thickness. Even at high current densities (up to 40 mA/cm^2, limiting current density being ~ 20 mA/cm^2), this epitaxial registry suppresses dendrite formation, ensures smooth interface evolution, and minimizes voltage hysteresis.

A critical insight of this work lies in identifying the role of underpotential deposition (UPD) as a chemically and structurally mediated process that enables sub-Nernstian Zn deposition on Cu. At intermediate overpotentials (–0.5 V vs Ag/AgCl), Zn atoms preferentially deposit onto Cu(111), forming a thermodynamically stable α-brass (Cu–Zn) solid solution. As the potential becomes more negative, the system transitions to bulk Zn-rich intermetallic growth. XRD peak shifts, SEM morphology, and EDS composition mapping confirm this alloying behavior, highlighting UPD as a critical route for phase-selective deposition. Moreover, in Zn–Cu binary systems, the study uncovers a voltage- and concentration-dependent mechanistic transition from UPD-induced surface alloying to 3D nucleation and cluster evolution. Specifically, in the potential

window between –1.0 V and –1.6 V, 3D Cu–Zn alloy clusters spontaneously form, acting as high-surface-area, conductive scaffolds that support fast Zn^{2+} desolvation and lateral growth. These clusters serve as auto-catalytic templates, simultaneously suppressing dendrite nucleation and accelerating reaction kinetics. The electrochemical response—marked by increased exchange current density, reduced nucleation overpotentials, and pseudo-capacitive behavior—reinforces this self-sustaining mechanism.

This thesis also extends its mechanistic insights to the Ni–Co binary alloy system, chosen due to the proximity of their standard reduction potentials. Here, the focus was on anomalous codeposition—wherein the more noble metal (Ni) deposits preferentially despite its thermodynamic disadvantage. The findings confirm that this behavior arises from asymmetric charge transfer kinetics and surface adsorption effects. By varying Ni^{2+}/Co^{2+} ratios and current densities, the electrodeposited alloy composition and texture could be tuned. The results establish that even in systems without large redox gaps (unlike Zn–Cu), interfacial control and substrate effects still play dominant roles in determining deposition morphology and performance. Together, the findings across Zn, Zn–Cu, and Ni–Co systems highlight the critical, underutilized role of crystallography–electrochemistry coupling in practical battery electrode design. The uniaxial nature of electrochemical fields favors out-of-plane texturing, particularly along close-packed, low-energy crystallographic planes such as Cu(111) and Zn(002). This work shows that such texture can be achieved not by costly single crystals, but through scalable powder metallurgy and thermomechanical processing. More broadly, this research underscores that rational manipulation of electrochemical interfaces—through substrate engineering, UPD exploitation, and electrochemical regime selection—can unlock new regimes of reversible, uniform, and phase-selective metal deposition.

The principles established in this work transcend the specific case of zinc and copper, offering a broader framework applicable to a wide range of metal and alloy systems used in rechargeable batteries, corrosion-resistant coatings, and electronic materials. The findings provide a blueprint for designing advanced electrode architectures that are not only structurally and kinetically tailored but also compatible with scalable manufacturing. Through this investigation, the intricate relationship between crystallography and electrochemical behavior at the metal–electrolyte interface has been systematically unraveled, culminating in a generalized strategy for

engineering dendrite-free, durable metal anodes that support sustainable electrochemical energy storage technologies.

Looking ahead, although prior studies have emphasized the importance of voltage profiles in optimizing high-entropy alloy (HEA) coatings, they have largely overlooked the mechanistic basis of these effects—particularly the role of electrolyte additives in modifying interfacial dynamics to achieve levels of coating quality comparable to that of monometallic systems. To address this gap, the next phase of this research should integrate experimental tools and numerical simulations to derive actionable design principles for fabricating uniform, compositionally controlled alloy coatings composed of two to five metals. Special attention will be given to tuning accessible parameters—such as electrolyte composition, voltage waveform, and interfacial additives—to guide crystal structure development, suppress morphological instabilities, and refine mechanical and electrochemical properties. Initial efforts will focus on predicting the onset of hydrodynamic instabilities, mapping stress distributions, and understanding morphology evolution in binary systems. These insights will then inform strategies to leverage interphase engineering—via polymer adsorption or externally applied flow fields—to delay or suppress instability, enabling high-fidelity morphological control in the deposition of complex alloy and HEA coatings.

REFERENCES

1. Volta, XVII. (1800) On the electricity excited by the mere contact of conducting substances of different kinds. In a letter from Mr. Alexander Volta, FRS Professor of Natural Philosophy in the University of Pavia, to the Rt. Hon. Sir Joseph Banks, Bart. KBPR S. Philosophical transactions of the Royal Society of London, 403-431, doi:10.1098/rspl.1800.0016.

2. Paunovic, M. and Schlesinger, M. (2006) Fundamentals of electrochemical deposition (Second Edition), Wiley Interscience, Hoboken, New Jersey

3. Dini, J.W. (1993) Electrodeposition – The Materials Science of Coating and Substrates. Noyes Publications, New Jersey.

4. Zheng, J. and Archer, L.A. (2022) Crystallographically textured electrodes for rechargeable batteries: symmetry, fabrication, and characterization. Chem. Rev. 122, 14440.

5. Hull, C.M. and Switzer, J.A. (2018) Electrodeposited Epitaxial Cu (100) on Si (100) and Lift-Off of Single Crystal-like Cu (100) Foils. ACS applied materials interfaces 10, 38596.

6. Hwang, S., Oh, I. and Kwak, J. (2001) Electrodeposition of epitaxial Cu (111) thin films on Au (111) using defect-mediated growth. Journal of the American Chemical Society 123, 7176

7. Diggle, J.W., Despic, A.R. and Bockris, J. O'M. (1969) The mechanism of dendritic electrocrystallization of zinc. J Electrochem Soc, 116, 1503.

8. Mullins, W.W. and Sekerka, R.F. (1964) Stability of a planar interface during solidification of a dilute binary alloy. Journal of Applied Physics 35, 444.

9. Rubinstein, I., Zaltzman, B. and Lerman, I. (2005) Electroconvective instability in concentration polarization and nonequilibrium electro-osmotic slip. Physical Review E 72, 011505.

10. Mani, A. and Wang, K.M. (2020) Electroconvection near electrochemical interfaces: Experiments, modeling, and computation. Annual Review of Fluid Mechanics 52, 509-529.

11. Huth, J. M., Swinney, H. L., McCormick, W. D., Kuhn, A. and Argoul, F. (1995) Role of convection in thin-layer electrodeposition. Physical Review E 51, 3444.

12. Fleury, V., Chazalviel, J. N. and Rosso, M. (1993) Coupling of drift, diffusion, and electroconvection, in the vicinity of growing electrodeposits. Physical Review E 48, 1279.

13. Barton, J.L. and Bockris, J. O'M. (1962) The electrolytic growth of dendrites from ionic solutions. Proc R Soc London, Ser A 268, 485.

14. W. J. Lorenz, H. D. Herrmann, N. Wüthrich and F. Hilbert, J. Electrochem. Sot. 121, 1167 (1974).

15. M. Alvarez, K. Jüttner, Simulation of UPD-electrocatalysis on single crystal surfaces, Electrochimica Acta, Volume 33, Issue 1, 1988.

16. D. M. Kolb. Advances in Electrochemistry and Electrochemical Engineering (Edited by H. Gerischkr and C. W. Tobias) Vol. 11, p. 125. John Wiley, New York (1978).

17. Bosco, E., & Rangarajan, S. K. (1981). Electrochemical phase formation (ECPF) nucleation growth vis-a-vis adsorption models. *Journal of Electroanalytical Chemistry*, *129*(1-2), 25–51.

18. McIntyre, J. D. E., & Peck, W. F., Jr. (1976). In situ ellipsometric studies of oxide film growth on metals. *Journal of the Electrochemical Society*, *123*(12), 1800–1813.

19. Kolb, D. M., Przasnyski, M., & Gerischer, H. (1974). Underpotential deposition of metals and work function differences. *Journal of Electroanalytical Chemistry*, *54*(1), 25–38.

20. Swathirajan & Bruckenstein, Thermodynamics Underpotential & Kinetics of Deposition of Metal Monolayers on Polycrystalline Substrates, Electrochemica Acta, Vol 28, No. 7, pp. 865-877, 1983

21. Jingxu Zheng and Lynden A. Archer, *Chemical Reviews* 2022 *122* (18), 14440-14470. DOI: 10.1021/acs.chemrev.2c00022

22. Dudney, N. J. Thin film micro-batteries. Electrochemical Society Interface 2008, 17 (3), 44.

23. Zheng, J.; Garcia-Mendez, R.; Archer, L. A. Engineering Multiscale Coupled Electron/Ion Transport in Battery Electrodes. ACS Nano 2021, 15, 19014.

24. Zhu, C.; Usiskin, R. E.; Yu, Y.; Maier, J. The nanoscale circuitry of battery electrodes. Science 2017, 358 (6369), No. eaao2808.

25. Usiskin, R. E.; Maier, J. Guidelines for optimizing the architecture of battery insertion electrodes based on the concept of wiring lengths. Phys. Chem. Chem. Phys. 2018, 20 (24), 16449.

26. Jungblut, B.; Hoinkis, E. Diffusion of lithium in highly oriented pyrolytic graphite at low concentrations and high temperatures. Phys. Rev. B 1989, 40 (16), 10810.

27. Mandeltort, L.; Yates, J. T., Jr Rapid atomic Li surface diffusion and intercalation on graphite: a surface science study. J. Phys. Chem. C 2012, 116 (47), 24962.

28. Zhang, X.; Ju, Z.; Zhu, Y.; Takeuchi, K. J.; Takeuchi, E. S.; Marschilok, A. C.; Yu, G. Multiscale Understanding and Architecture Design of High Energy/Power Lithium-Ion Battery Electrodes. Adv. Energy Mater. 2021, 11 (2), 2000808.

29. Callister, W. D., Jr., & Rethwisch, D. G. (2018). *Materials science and engineering: An introduction* (10th Australia and New Zealand ed.). Wiley.

30. Zheng, J. X.; Zhao, Q.; Tang, T.; Yin, J. F.; Quilty, C. D.; Renderos, G. D.; Liu, X. T.; Deng, Y.; Wang, L.; Bock, D. C.; et al. Reversible epitaxial electrodeposition of metals in battery anodes. Science 2019, 366 (6465), 645−648.

31. Xie, C. L.; Ji, H. M.; Zhang, Q.; Yang, Z. F.; Hu, C.; Ji, X. B.; Tang, Y. G.; Wang, H. Y. High-index zinc facet exposure induced by preferentially orientated substrate for dendrite-free zinc anode. Adv. Energy Mater. 2023, 13 (3), 2203203.

32. Liu, Z. P.; Guo, Z. K.; Fan, L. S.; Zhao, C. Y.; Chen, A. S.; Wang, M.; Li, M.; Lu, X. Y.; Zhang, J. C.; Zhang, Y.; et al. Construct robust epitaxial growth of (101) textured zinc metal anode for long life and high capacity in mild aqueous zinc-ion batteries. Adv. Mater. 2024, 36, 2305988.

33. Wang, M.; Wang, W.; Meng, Y.; Xu, Y.; Sun, J.; Yuan, Y.; Chuai, M.; Chen, N.; Zheng, X.; Luo, R.; Xu, K.; Chen, W. Crystal facet correlated Zn growth on Cu for aqueous Zn metal batteries. Energy Stor. Mater. 2023, 56, 424–431.

34. Hao, Z.; Zhang, Y.; Hao, Z.; Li, G.; Lu, Y.; Jin, S.; Yang, G.; Zhang, S.; Yan, Z.; Zhao, Q.; Chen, J. Metal anodes with ultrahigh reversibility enabled by the closest packing crystallography for sustainable batteries. Adv. Mater. 2023, 35 (9), 2209985.

35. Zhang, Y., Hu, Z., Bi, Y., Sun, L., Tian, S., Sun, H., Li, K., Liu, W., Liu, W., Huang, G., & Yang, C. (2025). Epitaxial Zn (002) growth directed by Cu (111): A dual-layer strategy toward stable and reversible Zn metal anodes. *Energy Storage Materials*, *79*, 104366. https://doi.org/10.1016/j.ensm.2025.104366

36. Yaroshevsky, A. A. Abundances of chemical elements in the Earth's crust. Geochem. Int. 2006, 44 (1), 48−55.

37. Hull, C.M. and Switzer, J.A. (2018) Electrodeposited Epitaxial Cu (100) on Si (100) and Lift-Off of Single Crystal-like Cu (100) Foils. ACS applied materials interfaces 10, 38596.

38. Mani, A. and Wang, K.M. (2020) Electroconvection near electrochemical interfaces: Experiments, modeling, and computation. Annual Review of Fluid Mechanics 52, 509-529

39. Nielsen, C.P. and Bruus, H. (2015) Morphological instability during steady electrodeposition at overlimiting currents. Physical Review E 92, 052310.

40. Huth, J. M., Swinney, H. L., McCormick, W. D., Kuhn, A. and Argoul, F. (1995) Role of convection in thin-layer electrodeposition. Physical Review E 51, 3444.

41. Fleury, V., Chazalviel, J. N. and Rosso, M. (1993) Coupling of drift, diffusion, and electroconvection, in the vicinity of growing electrodeposits. Physical Review E 48, 1279.

42. Barton, J.L. and Bockris, J. O'M. (1962) The electrolytic growth of dendrites from ionic solutions. Proc R Soc London, Ser A 268, 485.

43. Jesser, W. A., & Kuhlmann-Wilsdorf, D. (1981). Glide and climb stresses on secondary slip systems in F.C.C. crystals due to isolated primary edge and screw dislocations. *Materials Science and Engineering*, *51*, 31–37. https://doi.org/10.1016/0025-5416(81)90103-8

44. Hong S, Fang M, Baffour S, Gao Z, Jin S, Xu H, Yang R, Archer LA. Highly textured metal anodes for stable aqueous batteries: Fabrication and characterization. Sci Adv. 2025 Jul 11;11(28):eadx0289. doi: 10.1126/sciadv.adx0289. Epub 2025 Jul 9. PMID: 40632868; PMCID: PMC12239945.

45. Carlos, A., Siqueira, J.L.P., Finazzi, G.A. and de Almeida, M.R.H. (2003) Voltammetric study of lead electrodeposition in the presence of sorbitol and morphological characterization. J Power Sources, 117, 179.

46. Kan, J.Q., Xue, H.G. and Mu, S.L. (1998) Effect of Inhibitors on Zn-dendrite Formation for Zinc polyaniline Secondary Battery. J. Power Sources 74, 113.

47. Wei, S., Cheng, Z., Nath, P., Tikekar, M.D., Li, G. and Archer, L.A. (2018) Stabilizing electrochemical interfaces in viscoelastic liquid electrolytes. Science Advances 4, 6243.

48. Tikekar, M. D., Li, G., Archer, L.A. and Koch, D.L. (2018) Electroconvection and morphological instabilities in potentiostatic electrodeposition across liquid electrolytes with polymer additives. J. Electrochemical Society 165, A3697-A3713.

49. Zhao, Q., Zachman, M.J., AlSadat, W.I., Zheng, J., Kourkoutis, L.F. and Archer, L.A. (2018) Solid electrolyte interphases for high-energy aqueous aluminum electrochemical cells. Science Advances 4, eaau8131.

50. Wei, S. Choudhury, S., Tu, Z., Zhang, K. and Archer, L.A. (2018) Electrochemical Interphases for High-Energy Storage Using Reactive Metal Anodes, Accounts of Chemical Research 51, 80-88.

51. Zhao, Q., Tu, Z., Wei, S., Zhang, K., Choudhury, S., Liu, X. and Archer, L.A. (2018) Building organic inorganic hybrid interphases for fast interfacial transport in rechargeable metal batteries. Angewandte Chemie, Intl. Ed. 57, 992-996

52. Zhao, Q., Zheng, J. and Archer, L.A. (2018) Interphases in lithium-sulfur batteries: towards deployable devices with competitive energy density and stability. ACS Energy Lett. 3, 2104-2113

53. Li, G., Archer, L.A. and Koch, D.L. (2019) Electroconvection in a viscoelastic electrolyte. Phys. Rev. Lett. 122, 124501.

54. F.A. Moller, O.M. Magnussen, R.J. Behm, In situ STM studies of Cu underpotential deposition on Au(100) in the presence of sulfate and chloride anions, Phys. Rev. B Condens. Matter 51 (1995) 2484.

55. I. Park, H. Baltruschat, Atomic-scale friction study by EC-AFM: underpotential deposition (UPD) of Ag on I-modified Au(111) and its tip penetration, J. Electrochem. Soc. 169 (2022), 122501.

56. S.H. Zhu, Y.H. Dai, J.H. Li, C.M. Ye, W.H. Zhou, R.H. Yu, X.B. Liao, J.T. Li, W. Zhang, W. Zong, R.W. Chen, G.G. He, D.L. Chao, Q.Y. An, Cathodic Zn underpotential deposition: an evitable degradation mechanism in aqueous zinc-ion batteries, Sci. Bull. Beijing 08 (2022) 023.

57. Y. Dai, C. Zhang, W. Zhang, L. Cui, C. Ye, X. Hong, J. Li, R. Chen, W. Zong, X. Gao, J. Zhu, P. Jiang, Q. An, D.J.L. Brett, I.P. Parkin, G. He, L. Mai, Reversible Zn metal anodes enabled by trace amounts of underpotential deposition initiators, Angew. Chem. Int. Ed. Eng. 62 (2023), e202301192.

58. M. Nakamura, A. Aramata, A. Yamagi, M. Taniguchi, Underpotential deposition of zinc ions on Au(111) in phosphate solution (pH 4.6): kinetic and STM studies, J. Electroanal. Chem. 446 (1998) 227–231.

59. J.R. Davis, Nickel, Cobalt, and their Alloys, ASM International, 2000.

60. Akira Takeuchi & Akihisa Inoue, Calculations of Mixing Enthalpy & Mismatch Entropy for Ternary Amorphous Alloys, *Materials Transactions, JIM, Vol. 41, No. 11 (2000) pp. 1372-78.*

61. Hong, H., Wang, Q., Dong, C. *et al.* Understanding the Cu-Zn brass alloys using a short-range-order cluster model: significance of specific compositions of industrial alloys. *Sci Rep* **4**, 7065 (2014). https://doi.org/10.1038/srep07065

62. L Tian, L., Xu, J., & Qiang, C. (2011). The electrodeposition behaviors and magnetic properties of Ni–Co films. *Applied Surface Science, 257*, 4689–4694.

63. Farzaneh, M. A., Zamanzad-Ghavidel, M. R., Raeissi, K., Golozar, M. A., Saatchi, A., & Kabi, S. (2011). Effects of Co and W alloying elements on the electrodeposition aspects and properties of nanocrystalline Ni alloy coatings. *Applied Surface Science, 257*, 5919–5926.

64. El-Feky, H., Negem, M., Roy, S., Helal, N., & Baraka, A. (2013). Electrodeposited Ni and Ni–Co alloys using cysteine and conventional ultrasound waves. *Science China Chemistry, 56*, 1446–1454.

65. C. Gu, J. Lian, Z. Jiang, High Strength Nanocrystalline Ni-Co Alloy with Enhanced Tensile Ductility. *Advanced Eng. Mater. 8* (2006) 252–256.

66. J. Vazquez-Arenas, L. Altamirano-Garcia, T. Treeratanaphitak, M. Pritzker, R. Luna-Sánchez, R. Cabrera-Sierra, Electrochim. Acta 65 (2012) 234–243.

67. A. Brenner, Electrodeposition of Alloys: Principles and Practice, Elsevier, 2013.

68. Eliaz, N., Venkatakrishna, K., & Hegde, A. C. (2010). Electroplating and characterization of Zn–Ni, Zn–Co, and Zn–Ni–Co alloys. *Surface and Coatings Technology, 205*, 1969–1978.

69. Golodnitsky, D., Gudin, N. V., & Volyanuk, G. A. (2000). Study of nickel-cobalt alloy electrodeposition from a sulfamate electrolyte with different anion additives. *Journal of The Electrochemical Society, 147*(11), 4156–4163.

70. Vagramyan, A. T., & Fatueva, T. A. (1963). On the Theory of Simultaneous Discharge of Metal Ions in Real Conjugated Systems. *Journal of The Electrochemical Society, 110*(10), 1030–1035.

71. A. Ives, J. Edington, G. Rothwell, A transmission-electron-microscopy study of nickel films electrodeposited on (100) copper films. Electrochim. Acta 15 (1970) 1797–1801.

72. Gangasingh, D., & Talbot, J. B. (1991). Electrodeposition of nickel–iron alloys: rotating cylinder Hull cell study of anomalous codeposition. *Journal of The Electrochemical Society, 138*(11), 3605–3611.

73. Grande, W. C., & Talbot, J. B. (1993). Nickel–iron codeposition under pulse plating conditions. *Journal of The Electrochemical Society, 140*(3), 675–681.

74. Hessami, S., & Tobias, C. W. (1989). A Mathematical Model for Anomalous Codeposition of Nickel-Iron on a Rotating Disk Electrode. *Journal of the Electrochemical Society*, *136*(12), 3611–3616.

75. Sasaki, K. Y., & Talbot, J. B. (2000). Electrodeposition of iron-group metals and binary alloys from sulfate baths. III. Experimental studies and mathematical modeling of nickel-cobalt alloys. *Journal of the Electrochemical Society*, *147*(1), 189–197.

76. Sasaki, K. Y., & Talbot, J. B. (1998). Electrodeposition of iron-group metals and binary alloys from sulfate baths. II. Modeling. *Journal of the Electrochemical Society*, *145*(3), 981–990.

77. Sasaki, K. Y., & Talbot, J. B. (1995). Electrodeposition of iron-group metals and binary alloys from sulfate baths. I. Experimental study. *Journal of the Electrochemical Society*, *142*(3), 775–782.

78. Matlosz, M. (1993). Competitive adsorption effects in the electrodeposition of iron-nickel alloys. *Journal of the Electrochemical Society*, *140*(8), 2272–2279.

79. Baker, B. C., & West, A. C. (1997). Electrodeposition of nickel-iron alloys from sulfate electrolytes. II. Modeling. *Journal of the Electrochemical Society*, *144*(1), 169–175.

80. Baker, B. C., & West, A. C. (1997). Electrodeposition of nickel-iron alloys from sulfate electrolytes. I. Experimental results. *Journal of the Electrochemical Society*, *144*(1), 164–169.

81. Vazquez-Arenas, J., & Pritzker, M. (2012). Theoretical analysis of multiple steady states in electrodeposition of Ni-Fe alloys. *Electrochimica Acta*, *66*, 139–150.

82. Podlaha, E., & Landolt, D. (1996). Induced codeposition. I. An experimental investigation of Ni-Mo alloys. *Journal of the Electrochemical Society*, *143*(3), 885–892.

83. Podlaha, E., & Landolt, D. (1997). Induced codeposition. II. A mathematical model describing the electrodeposition of Ni-Mo alloys. *Journal of the Electrochemical Society*, *144*(5), 1672–1680.

84. Zech, N., Podlaha, E., & Landolt, D. (1999). Anomalous codeposition of iron group metals. I. Experimental results. *Journal of the Electrochemical Society*, *146*(8), 2886–2891.

85. Zech, N., Podlaha, E., & Landolt, D. (1999). Anomalous codeposition of iron group metals. II. Mathematical model. *Journal of the Electrochemical Society*, *146*(8), 2892–2900.

86. Zech, N., Podlaha, E., & Landolt, D. (1998). Rotating disk electrode study of the anomalous codeposition of iron group metals with molybdenum and tungsten. *Journal of Applied Electrochemistry*, *28*(11), 1251–1260.

87. Chung, C.-K., & Chang, W. (2009). Effect of pulse frequency and current density on anomalous composition and nanomechanical property of electrodeposited Ni-Co films. *Thin Solid Films*, *517*(15), 4800–4804.

88. Vazquez-Arenas, J., Altamirano-Garcia, L., Pritzker, M., Luna-Sánchez, R., & Cabrera-Sierra, R. (2011). Experimental study of Ni-Co alloy electrodeposition with different agitation conditions. *Journal of the Electrochemical Society*, *158*(1), D33–D41.

89. Vazquez-Arenas, J., & Pritzker, M. (2011). Theoretical analysis of current and potential oscillations during nickel-iron electrodeposition. *Electrochimica Acta*, *56*(24), 8023–8033.

90. Vazquez-Arenas, J., & Pritzker, M. (2010). Analysis of copper-nickel alloy electrodeposition accounting for complexation. *Electrochimica Acta*, *55*(26), 8376–8387.

91. Goldbach, S., De Kermadec, R., & Lapicque, F. (2000). Electrodeposition of nickel-iron alloys from a chloride bath containing NH4Cl. *Journal of Applied Electrochemistry*, *30*(3), 277–284.

92. El-Halim, A. A. (1984). Electrodeposition and corrosion behaviour of nickel-iron alloys. *Surface Technology*, *23*(3), 207–213.

93. Grande, W. C., & Talbot, J. B. (1993). Electrodeposition of thin films of nickel-iron. I. Experimental. *Journal of the Electrochemical Society*, *140*(3), 669–674.

94. Vazquez-Arenas, J., Ramos-Sanchez, G., Lara, R. H., Romero-Ibarra, I., Almazan, M., & Lartundo-Rojas, L. (2017). Understanding the electrodeposition process of Ni-Co alloys by means of the apparent molar Gibbs free energy of activation for viscous flow concept. *ChemistrySelect*, *2*(6), 1826–1834.

95. Hu, H., Tan, M., & Liu, L. (2017). Electrodeposition and characterization of Ni-Co-TiO2 composite coatings. *Journal of Alloys and Compounds*, *715*, 384–389.

96. Benisek, A., Dachs, E., Salihović, M., Paunovic, A., & Maier, M. E. (2014). The vibrational and configurational entropy of α-brass. *Journal of Chemical Thermodynamics, 71*, 126–132. https://doi.org/10.1016/j.jct.2013.11.012

97. Sillen, L. G., & Martell, A. E. (1964). *Stability Constants of Metal-Ion Complexes, Part A: Inorganic Ligands*. IUPAC; Chemical Society (London).

98. C. Q. Cui et al 1991. Mechanism of the Electrodeposition of Cobalt(II) Chloride in N,N-Dimethylformamide (DMF) Solution. J. Electrochem. Soc. 138 94

99. V. Gutmann, "Coordination Chemistry in Non- Aqueous Solutions," Springer-Verlag, New York (1968).

100. Marcus, Y. (1997). *The Properties of Solvents*. Wiley

101. Meek, D. W., Straub, D. K., & Drago, R. S. (1960). Transition metal ion complexes of dimethyl sulfoxide. *Journal of the American Chemical Society, 82*(23), 6013–6016.

102. C. Q. Cui, S. P. Jiang, and A. C. C. Tseung, Journal of the Electrochemical Society, 137(11), 3418 (1990)

103. Straub, D. K., & Drago, R. S. (1965). The stretching frequency of the S=O bond in dimethyl sulfoxide complexes. *Journal of the American Chemical Society, 87*(15), 3581–3585.

104. Sandell, E. B., Lorimer, J. W., & Lewis, J. (1969). Vibrational spectra and structure of nickel(II) and copper(II) complexes of dimethyl sulfoxide. *Inorganica Chimica Acta, 3*(6), 625–629.

105. Grzybkowski, W., & Pilarczyk, M. (1986). Ionization equilibria of cobalt(II) chloride in N,N-dimethylformamide. *Journal of the Chemical Society, Faraday Transactions 1*, *82*, 1703–1712

106. Grzybkowski, W., & Pilarczyk, M. (1986). Stability of monochloride complexes of some divalent transition-metal cations in N,N-dimethylformamide. *Journal of the Chemical Society, Faraday Transactions 1*, *82*, 1745–1753

107. Pilarczyk, M., Grzybkowski, W., & Klinszporn, L. (1987). *Journal of the Chemical Society, Faraday Transactions 1*, *83*, 2261

108. Basolo, F., & Pearson, R. G. (1967). *Mechanisms of inorganic reactions: A study of metal complexes in solution* (2nd ed.). John Wiley & Sons.

109. Chung, C. K., & Chang, W. T. (2009). Effect of pulse frequency and current density on anomalous composition and nanomechanical property of electrodeposited Ni–Co films. *Thin Solid Films, 517*(16), 4800–4804.

110. Gamburg, Y. D., & Zangari, G. (2011). *Theory and practice of metal electrodeposition*. Springer. https://doi.org/10.1007/978-1-4419-9669-5

111. Ohring, M. (2001). *Materials Science of Thin Films* (2nd ed.). Academic Press.

112. Hu, J., Al-Salihy, A., Zhang, B., Li, S., & Xu, P. (2022). Mastering the D-band center of iron-series metal-based electrocatalysts for enhanced electrocatalytic water splitting. *International Journal of Molecular Sciences, 23*(23), Article 15405.

113. Bhattacharjee, S., Waghmare, U. V., & Lee, S.-C. (2016). An improved d-band model of the catalytic activity of magnetic transition metal surfaces. *Scientific Reports, 6*, Article 35916.